

# ATOMIC AND MOLECULAR OPACITIES FOR BROWN DWARF AND GIANT PLANET ATMOSPHERES

C.M. SHARP<sup>1</sup>, A. BURROWS<sup>1</sup>

*Accepted to Ap.J. Suppl.*

## ABSTRACT

We present a comprehensive description of the theory and practice of opacity calculations from the infrared to the ultraviolet needed to generate models of the atmospheres of brown dwarfs and extrasolar giant planets. Methods for using existing line lists and spectroscopic databases in disparate formats are presented and plots of the resulting absorptive opacities versus wavelength for the most important molecules and atoms at representative temperature/pressure points are provided. Electronic, ro-vibrational, bound-free, bound-bound, free-free, and collision-induced transitions and monochromatic opacities are derived, discussed, and analyzed. The species addressed include the alkali metals, iron, heavy metal oxides, metal hydrides,  $H_2$ ,  $H_2O$ ,  $CH_4$ ,  $CO$ ,  $NH_3$ ,  $H_2S$ ,  $PH_3$ , and representative grains. Once monochromatic absorption cross sections for all constituents have been derived, chemical abundances have to be obtained before the resulting product can be summed to obtain total opacities. Hence, we include a review of the thermochemistry, techniques, and databases needed to derive equilibrium abundances and provide some sample results.

*Subject headings:* infrared: stars — stars: fundamental parameters — stars: low mass, brown dwarfs, spectroscopy, atmospheres, spectral synthesis

## 1. INTRODUCTION

The discoveries of extrasolar giant planets and brown dwarfs in 1995 have opened up exciting new fields in astrophysics. These enable model atmospheres to be directly tested against observations for atmospheric temperatures and pressures at which a large number of molecules that had not been considered before in stellar astrophysics reside. Moreover, many of the extrasolar planets, including the first to be discovered, are much closer to their parent star than Mercury is to the Sun so the atmospheric conditions of these planets are totally unlike any previously investigated. In such situations, many of these molecules are subjected to a large ultraviolet flux from the parent star.

The absorption of radiation by molecules is generally much more complicated than by atoms. Since many of the molecules in the atmospheres of brown dwarfs and extrasolar giant planets had not been studied in detail in an astrophysical context before 1995, their properties are still poorly known. Even those that had been investigated, had not been for the temperatures (100 - 3000 K) and pressures ( $10^{-6}$  - 100 atmospheres) found in the atmospheres of such objects. Moreover, an additional factor of considerable importance is the formation of grains. In this paper, we address the spectroscopy and opacities of the molecules and atoms central to an understanding of substellar objects. Such opacities are required for models of their spectra and evolution.

Another consequence of the emergence of this young field is the extension of the spectral classification system beyond late-type M-dwarf stars to include two new spectroscopic classes at lower temperatures, L and T dwarfs. The criteria for these new classes depend upon the strengths of atomic and molecular spectral lines, which in turn are governed by absorption cross sections and the abundances of various species.

In this paper, we discuss the methods used to calculate opacities from extant line lists or by directly calculating the energy levels. The absorption due to spectral lines is the most important source of opacity, as well as the most difficult to calculate, and this is considered in §2. After dealing with the background theory for calculating line strengths and broadening, and how to handle a frequency grid that samples the lines, we review the chemical species used for calculating substellar atmospheres. These are grouped together when they share important similarities, such as being metal hydrides or absorbing in the same general part of the spectrum. Table 1 lists the species considered in this work and gives the sections where the species are discussed in detail, including several condensates addressed with the Mie theory.

In §2.1, we discuss the species with data obtained from the HITRAN (Rothman et al. 2003, 2005) and GEISA (Jacquinet-Husson et al. 1999, 2003, 2005) databases, together with other sources. The spectral range covered is the visible and infrared. The molecules considered in detail are  $H_2O$  (Partridge & Schwenke 1997; Barber et al. 2006),  $CH_4$  (Strong et al. 1993; Karkoscka 1994; Borysow et al. (2003); Brown et al. 1997),  $NH_3$  (Brown et al. 2000),  $CO$  (Goorvitch, 1994). Of these,  $CH_4$  and  $NH_3$  are important at the lower temperatures of interest,  $CO$  is important at the upper temperatures of interest, and  $H_2O$  is very important over the whole temperature range.

In §2.2, we discuss the two heavy metal oxides,  $TiO$  (Allard, Hauschildt & Schwenke 2000) and  $VO$  (Plez 1998). Of the heavy metal oxides, these are the most important sources of opacity at the higher end of the temperatures of interest. Both have very similar properties. This is followed by §2.3, where we discuss the metal hydrides  $TiH$

<sup>1</sup> Department of Astronomy and Steward Observatory, The University of Arizona, Tucson, AZ 85721; csharp@as.arizona.edu, burrows@zenith.as.arizona.edu

(Burrows et al. 2005), *CrH* (Burrows et al. 2002), *FeH* (Dulick et al. 2003), *MgH* (Skory et al. 2003; Weck et al. 2003a), and *CaH* (Leininger & Jeung 1995), which all have similar properties.

As much as possible, the most extensive and up-to-date spectroscopic data available are considered. In the case of *H<sub>2</sub>S* and *PH<sub>3</sub>*, tables of precomputed opacities can be used, so calculations are restricted to interpolating in the ranges of temperature and pressure in the tables, but since these species have low abundances, they are relatively unimportant.

Ultraviolet opacities are important when a planet is irradiated by the star it orbits, and in §2.5 we discuss these opacities for atomic hydrogen (Menzel 1969; Bethe & Salpeter 1957; Carson 1988a), atomic iron (Kurucz 1995), and the molecules *H<sub>2</sub>*, *CO*, *SiO*, *H<sub>2</sub>O* (Kurucz 1993), and *H<sub>2</sub>S* (Lee, Wang & Suto 1987). The available data vary considerably, and this dictates the methods used to calculate the opacities.

The absorption of the alkali elements in monatomic form: *Li*, *Na*, *K*, *Rb*, and *Cs* using the Vienna Atomic Line Data, (VALD - Piskunov 1994) is considered in §2.6. The line strengths and widths are all calculated in a uniform way, except for the wings of the resonance lines of *Na* and *K* (Burrows & Volobuyev 2003; Allard et al. 2003; Zhu, Babb, & Dalgarno 2006), for which a separate treatment should be applied.

In addition to lines, the absorption due to the underlying continuum is calculated, as discussed in §3. Rosseland and other harmonic mean opacities are divergent if the absorption drops to zero at any point in the frequency region considered, and a realistic truncation of the wings of spectra lines is required. The four processes discussed are free-free, bound-free, collision-induced absorption in the gas phase, and grain absorption by condensed phases.

For the temperatures and pressures of interest, free-free opacity sources are the least important, so are only briefly covered in §3.1, since they can make at most a minor contribution at the upper end of the temperature range of interest. We discuss a number of free-free opacity sources, but in practice the only ones of even minor importance are *H<sub>ff</sub>* (Carson 1988a), *H<sub>ff</sub><sup>-</sup>* (Wishart 1979), *He<sub>ff</sub><sup>-</sup>* (Bell, Berrington & Croskery 1982), and *H<sub>2ff</sub><sup>-</sup>* (Bell 1980). We adopt the convention of including the free electron in the net charge of the whole system undergoing photon absorption, so here *H<sub>ff</sub>* refers to an electron moving in the field of a proton, and *H<sub>ff</sub><sup>-</sup>* refers to an electron moving in the field of a neutral hydrogen atom, and likewise for the other species.

Of considerably greater importance is bound-free absorption, as discussed in §3.2. We calculate the contribution due to *H* with Gaunt factors from Carson (1988a), its negative ion *H<sup>-</sup>* (Wishart 1979; Bell & Berrington 1987), and the atomic species *Na* (Cunto & Mendoza 1992; Cunto et al. 1993), *K* (Verner & Yakovlev 1995), and *Fe* (Kurucz 1995). The ion *H<sup>-</sup>* is important only when there is a supply of free electrons, and this is the case only when the species with the lowest ionization potentials, namely the alkali elements, become ionized.

At high pressures, collision-induced absorption, as discussed in §3.3, can be very important in the infrared. In an astrophysical mixture for the temperatures of interest to us here, the two most important contributions are due to *H<sub>2</sub> – H<sub>2</sub>* (Borysow et al. 1985; Zheng & Borysow 1995a; Zheng & Borysow 1995b; Borysow & Frommhold 1990; Lenzuni, Chernoff, & Salpeter 1991; Guillot et al. 1992), and *H<sub>2</sub> – He* collisions (Borysow, Frommhold, & Birnbaum 1988; Borysow, Frommhold, & Moraldi 1989; Borysow & Frommhold 1989). Although the contribution to the opacity due to *H<sub>2</sub> – CH<sub>4</sub>* collisions is much weaker, *CH<sub>4</sub>* is an important molecule and the data are available.

The detailed discussion of opacity calculations is completed in §3.4 by calculating Mie scattering due to grains formed by the condensation of species out of the gas phase (Van de Hulst 1957; Sudarsky 2002). Both the real and imaginary components of the refractive indices are needed and used.

Once all the individual opacity sources have been calculated, they must be weighted by abundances and combined into monochromatic opacities or suitable mean opacities, as discussed in §3.5. For the abundances calculated in §4, suitable thermodynamic data are required, and methods of handling them are discussed. Once the abundances are used to derive the total monochromatic opacity, Rosseland and Planck mean opacities can be calculated, if desired.

## 2. LINE OPACITIES

The sources of opacities of greatest interest are bound-bound transitions of atoms and molecules, and are the main focus of this paper. These involve the greatest computational efforts, and often influence most strongly the computation of model atmospheres of brown dwarfs and giant planets. Such transitions involve the absorption of a photon by an atom or molecule in the ground state, or a discrete initial excited state, to a more excited state, giving rise to a set of spectral lines, whose frequencies, strengths, and widths have to be calculated.

For some atoms, notably the alkali elements, there are only a few strong lines and a relatively modest number of weak lines that need to be considered. For other elements, such as iron, there are a large number of lines. For molecules the number of lines that need to be considered can be very large indeed, often numbered in the millions, hundreds of millions, or billions, which require a significant amount of computing in order to calculate the opacity. All the gaseous species down to *CaH* in Table 1 contribute line absorption, with the exception of the *H<sup>-</sup>* ion, which has no lines, and *He* which has no lines of importance in the spectral regions of interest.

The calculation of the line strengths for each line of each species depends on the data available for the species being considered, so different methods have to be used, as discussed in §2.1, §2.2, §2.3, §2.5, and §2.6. In order to reduce the chances of errors with input data in different forms, it is recommended to convert, if necessary, all the line strengths into the same uniform system, with the best being integrated line strengths in  $\text{cm}^2\text{s}^{-1}\text{species}^{-1}$ . These depend only on the temperature. The lines should then be broadened to a suitable profile which is dependent on the pressure, then the monochromatic absorption in  $\text{cm}^2\text{species}^{-1}$  across the profile should be computed, with the contributions from any overlapping profiles being summed. The monochromatic absorption for each species so obtained depends on the temperature and pressure. The total monochromatic opacity of the gas is obtained by summing up the individual

contributions weighted by the abundances as number densities in  $\text{cm}^{-3}$  for each of the species, yielding the total monochromatic volume opacity in  $\text{cm}^2\text{cm}^{-3}$ , i.e.  $\text{cm}^{-1}$ ; however, the total monochromatic mass opacity in  $\text{cm}^2\text{g}^{-1}$  is usually the required result, and is obtained by dividing the volume opacity by the gas mass density. This is discussed later in §3.5.

In its most general LTE (Local Thermodynamic Equilibrium) form, the integrated strength  $S$  of a spectral line in  $\text{cm}^2 \text{s}^{-1} \text{species}^{-1}$  is obtained from

$$S = \frac{\pi e^2 g_i f_{ij} e^{-hcF_i/kT}}{m_e c Q(T)} \left[ 1 - e^{-hc(F_j - F_i)/kT} \right], \quad (1)$$

where  $g_i$  and  $f_{ij}$  are, respectively, the statistical weight of the  $i^{\text{th}}$  energy level and the oscillator strength for a transition from that level to a higher level  $j$ ,  $F_i$ , and  $F_j$  are, respectively, the term values (excitation energies) in  $\text{cm}^{-1}$  of the  $i^{\text{th}}$  and  $j^{\text{th}}$  levels participating in the transition, and  $Q(T)$  is the partition function of the species at some temperature  $T$ . The other symbols have their usual meanings. Note that the first term in eq. (1) gives the line strength in  $\text{cm}^2 \text{s}^{-1} \text{absorber}^{-1}$ , the next term with the Boltzmann factor and the partition function converts this to the required line strength, and the last term is the stimulated emission correction factor, where  $F_j - F_i$  is the transition frequency in wavenumbers, i.e.  $\bar{\nu}$  in  $\text{cm}^{-1}$ . Although monochromatic opacities are displayed later as functions of wavelength, it is recommended that all opacity calculations be performed internally in wavenumbers, even if some of the input data are given in wavelengths, as most molecular spectroscopic constants and energy levels are expressed in  $\text{cm}^{-1}$ , and adopting a uniform system of units reduces the chances of error.

However, much of the data available are not expressed in the form of oscillator strengths and statistical weights, collectively given as  $gf$ -values, but in other forms that must be converted to the required lines strengths (see §2.1).

The general expression for calculating the partition function is given by

$$Q(T) = \sum_{i=1}^n g_i e^{-hcF_i/kT}, \quad (2)$$

where the summation is performed over the first  $n$  levels, whose contributions are required at the highest temperatures of interest. The term value of the lowest level  $F_1$ , i.e. the ground state, is zero by construction.

For atoms, eq. (2) can be evaluated directly with the data from Moore (1949) up to term values of about 20,000  $\text{cm}^{-1}$ , above which the contribution to the partition function is less than 1% at all relevant temperatures. Formally the partition function is divergent, but for the pressures of interest, the higher levels that can cause this problem are not populated. However, because molecules contain a large number of energy levels, directly summing the levels is usually impractical and other methods should be used, depending on the data. For diatomic molecules, a good approximation is to assume that the rotational, vibrational, and electronic contributions to the partition function can be separately evaluated for each electronic state, then combined by summing their products weighted by the Boltzmann factor of each electronic state. This gives

$$Q(T) = \frac{1}{\sigma} \sum_{i=1}^n Q_{e_i} Q_{v_i} Q_{r_i} e^{-hcT_i/kT}, \quad (3)$$

where  $\sigma$  is the symmetry number, equal to 1 or 2 for heteronuclear and homonuclear molecules, respectively,  $Q_{e_i}$ ,  $Q_{v_i}$ , and  $Q_{r_i}$  are the electronic, vibrational, and rotational contributions, respectively, to the partition function of the  $i^{\text{th}}$  electronic state, and  $T_i$  is the term value in  $\text{cm}^{-1}$  of the  $i^{\text{th}}$  state, with, as before, the ground state energy zero energy by definition. As with the atoms, levels above about 20,000  $\text{cm}^{-1}$  contribute less than 1% to the partition function and, therefore, can be neglected.

When present, multiplet spin splitting of an electronic state is small compared to  $kT/hc$ , and the electronic partition function can be considered a statistical weight without any temperature dependence and is given by (on dropping the  $i$  subscript for clarity)

$$Q_e = (2S + 1)(2 - \delta_{\Lambda,0}), \quad (4)$$

where  $S$  is the electron spin quantum number,  $2S + 1$  is the multiplicity,  $\Lambda$  is the electronic orbital quantum number: 0, 1, 2, 3... for  $\Sigma$ ,  $\Pi$ ,  $\Delta$ ,  $\Phi$ ... electronic states, respectively, and  $\delta$  is the Kronecker delta. All states other than  $\Sigma$  states contribute an additional factor of two. If the spin splitting is large compared to  $kT/hc$ , then the individual multiplet states can be treated as separate substates, and weighted by the Boltzmann factor of that substate. The vibrational and rotational contributions to the partition function for each electronic state in eq. (3) can be calculated using asymptotic formulae derived from Kassel (1933a, 1933b).

In some cases where partition functions of diatomic molecules are already available in the literature as tables, as is the case with  $TiO$ , it may be more convenient to use polynomial approximations, rather than evaluating eq. (3) using the methods outlined above. Expressions for calculating the partition functions of polyatomic molecules are in general very much more complicated, but with the available data in §2.1, only the partition functions of  $CH_4$ ,  $H_2O$ , and  $NH_3$  are required. Of these, that of  $CH_4$  is easily calculated by evaluating a formula, as given in §2.1. Unlike

the other molecules considered,  $CH_4$  is a spherical top molecule with three equal principle moments of inertia. The partition functions of the other molecules can be obtained from polynomial fits.

In the case of diatomic molecules, each electronic state is split up into vibrational and rotational levels, and transitions between two electronic states, or even within the same (usually the ground state), make up a band system. Transitions between two given vibrational levels make up a band, which in turn is resolved into individual rotational lines that have to be calculated separately. If the  $gf$  values of these rotational lines are available, then eq. (1) can be used as above, but if they are not, the line strengths can still be calculated, provided an oscillator strength is available for either the band system, or the particular band being calculated. In the latter case, eq. (1) can be replaced by

$$S = \frac{\pi e^2}{m_e c} f_{v'v''} \frac{\bar{\nu}}{\bar{\nu}_{v'v''}} S_{J',J''}^{\Lambda',\Lambda''} \frac{e^{-hcF_i/kT}}{Q(T)} \left[ 1 - e^{-hc(F_j - F_i)/kT} \right], \quad (5)$$

where  $f_{v'v''}$  is the band oscillator strength for the  $v' \leftarrow v''$  transition (by convention, in molecular spectroscopic notation the lower state is double-primed, and is given after the upper state),  $\bar{\nu}$  is the transition frequency of the band origin (the hypothetical transition with  $J' = J'' = 0$ ), and  $S_{J',J''}^{\Lambda',\Lambda''}$  is the Hönl-London factor (Herzberg 1950; Kovács 1969) for the rotational transition  $J' \leftarrow J''$  between the electronic states with the corresponding values  $\Lambda'$  and  $\Lambda''$ . Note that the Hönl-London factors express the contributions to the total line strengths of the rotational wavefunctions of the participating levels, and should be normalized such that they satisfy eq. (4), which accounts for the statistical weight.

In cases where individual band oscillator strengths are not given, the line strengths can be calculated from the electronic strength of the band system, from which the band oscillator strengths can be calculated using

$$f_{v'v''} = q_{v'v''} f_{el}(\bar{\nu}_{v'v''}), \quad (6)$$

where  $q_{v'v''}$  is the Franck-Condon factor and  $f_{el}(\bar{\nu}_{v'v''})$  is the electronic oscillator strength of the system. Note that the Franck-Condon factors are defined only for transitions between different electronic states, express the relative contributions to the band strengths due to the vibrational wavefunctions of the participating levels, and are normalized such that they sum to unity from a given  $v''$  to all possible values of  $v'$ , (likewise, for the reverse transitions, assuming that the electronic oscillator strength is a constant over the system). In general, this will be a function of the frequencies of the band origins, and can be accounted for by using r-centroids, as first introduced by Fraser (1954), and subsequently used, by, for example, Nicholls & Jarman (1956), Nicholls (1965), and Sharp (1984). When such data are not readily available, and the variation of the electronic component of the oscillator strength over the band system is unknown, it could only be obtained by experiment or detailed quantum mechanical calculations. Both of these are beyond the scope of our work, and the simplest assumption is to assume it is constant. This is justified by Schadee (1967), who provides a number of figures and expressions that show the variation of the electronic component of the band oscillator strength as a function of wavelength for one or more band systems of each of the molecules  $C_2$ ,  $CN$ ,  $N_2$ ,  $N_2^+$ ,  $CO^+$ ,  $NO$ , and  $O_2$ . With the exception of the red system of  $CN$  ( $A^2\Pi_i - X^2\Sigma^+$ ) and possibly the Schumann-Runge system of  $O_2$  ( $B^3\Sigma_u^- - X^3\Sigma_g^-$ ), these associated oscillator strengths vary by not much more than a factor of three at worst across the bands; even the exceptions still vary by less than an order of magnitude. For polyatomic molecules a similar, though considerably more complicated, theory is in general involved, but data in forms suitable for direct opacity calculations are often available, as discussed in §2.1.

Many elements have several isotopes which can have a significant abundance. For example, the dominant isotope of titanium,  $^{48}Ti$ , makes up about 74% of all isotopes of titanium, with four other isotopes making up the balance. The isotopic shifts of atomic lines are negligible, but are significant for molecules, and have to be considered for calculating line positions, though not for calculating partition functions (see below). Many datasets included line strengths and positions of isotopically substituted molecules, so no additional provisions have to be made. However, for those diatomic molecules which involve elements with significant fractions of minor isotopic species, and for which only data on the most abundant isotopic form are available, the isotopically shifted lines can be calculated. This can only be performed if the data for each transition include the vibrational and rotational quantum numbers of the participating states.

If  $\mu$  and  $\mu^i$  are, respectively, the reduced masses of the main isotopic version and an isotopically substituted version of the molecule, then given from Herzberg (1950)

$$\rho = \sqrt{\frac{\mu}{\mu^i}}, \quad (7)$$

the isotopic shifts of the harmonic, anharmonic and second-order anharmonic vibrational constants are, respectively,  $\omega_e^i = \rho\omega_e$ ,  $\omega_e^i x_e^i = \rho^2\omega_e x_e$  and  $\omega_e^i y_e^i = \rho^3\omega_e y_e$ , the rigid and non-rigid rotational constants are, respectively,  $B_e^i = \rho^2 B_e$  and  $D_e^i = \rho^4 D_e$ , and the first- and second-order vibration-rotation coupling constants are, respectively,  $\alpha_e^i = \rho^3 \alpha_e$  and  $\beta_e^i = \rho^5 \beta_e$ . The shifts of higher order constants, even when available, are neglected. This is because they make only a small correction to the energy levels. For multiplet states, various spin-orbit and spin-spin coupling constants, again if they are available, are also neglected, and it is assumed that the levels are shifted by only the effects already mentioned. This is a higher order effect beyond the scope of this work, and is expected to have a small influence. With the isotopically shifted constants, together with the vibrational and rotational quantum number, the positions of the shifted energy levels can be calculated, and, thus, also the positions of the lines in the spectrum. The line strength

are obtained by just multiplying the strength from eq.(5) by the fractional abundance of the isotope of the element. This is applied also to the main isotopic version of the molecule, if more than one are considered.

In nearly all cases the main isotopic form of a molecule is more than an order of magnitude more abundant than the next most abundant isotopic form, so abundance effect dominates in the line strengths over other isotopic effects. The effects due to isotopically-shifted partition functions are generally only a few percent, and so are neglected. The line strengths will also be influenced by the changed wavefunctions due to the shifted energy levels of the participating states, but this is also expected to be small, as the isotopic shifts of energy levels are small compared to the depth of a typical internuclear potential well, whose shape is to a high order independent of the nuclear masses. Even if the necessary data are available, calculating such wavefunctions is beyond the scope of this work and would provide at best a very marginal improvement in accuracy. In the case of homonuclear diatomic molecules, the line strengths also depend on the nuclear spins, and alternate between levels with even and odd parities (Herzberg 1950). For nuclei with zero spin, alternate levels are missing. When one of the atoms is replaced by an isotope, the molecule becomes heteronuclear and this symmetry is lost. If both atoms are replaced by another isotope causing the molecule to be homonuclear again, the line strengths alternate with parity depending on the nuclear spins. Thus, in the case of homonuclear molecules these effects have to be accounted for. The only homonuclear molecule considered in the opacity calculations in this work is  $H_2$ , but deuterium is not discussed due to its low abundance. In the case of polyatomic molecules, the shifts are considerably more complicated to calculate, and most of the data on these molecules already include the isotopes. In situations where no isotopic data are given, no data on the levels involved in the transitions are given either.

Once the integrated line strength for a particular transition being considered has been obtained, including any isotopic versions of a molecule, its contribution to the monochromatic absorption has to be calculated. This requires the line to be broadened into a suitable profile, and the calculation of the absorption across each profile is the most intensive part of any calculation.

With the exception of the resonance lines of sodium and potassium, a Lorentzian profile should be used for all the broadening calculations. Because of the generally high pressures and low temperatures, Lorentzian broadening dominates over Gaussian Doppler broadening, so not employing general Voigt profiles is justified, particularly when there are large uncertainties with broadening. Accordingly, the monochromatic absorption in  $\text{cm}^2\text{species}^{-1}$  can be calculated using

$$\sigma(\bar{\nu}) = \left(\frac{Sb}{c}\right) \frac{\Delta\bar{\nu}/2\pi}{(\Delta\bar{\nu}/2)^2 + (\bar{\nu} - \bar{\nu}_o)^2}, \quad (8)$$

where as before  $S$  is the integrated line strength,  $b$  is the normalization correction factor,  $c$  is the velocity of light,  $\Delta\bar{\nu}$  is the Lorentzian full-width at half-maximum in  $\text{cm}^{-1}$ , and  $\bar{\nu}_o$  is the frequency of the line center in  $\text{cm}^{-1}$ . If the profile is calculated out to large distances in the wings from the line center, then the normalization correction factor is unity. However, a major problem in calculating profiles is to know how to treat the far wings. If the wings are simply extrapolated out to large values of  $|\bar{\nu} - \bar{\nu}_o|$ , the absorption is unrealistically large, and an excessive amount of computing time is used. As the absorption generally drops off in the far wings at a rate larger than a simple Lorentzian profile, a suitable treatment in the absence of a detailed theory would be to cut off the profile at some distance  $d$  from the line center, given by a simple prescription of the form  $d = \min(25P, 100) \text{ cm}^{-1}$ , where  $P$  is the total gas pressure in atmospheres. The  $\min()$  function ensures that the lines do not become unrealistically broad.

Because the profile is truncated at a distance  $d$  from  $\bar{\nu}_o$ , in order to ensure that the total strength of the profile is conserved, the normalization correction factor  $b$  in eq. (8) is greater than unity, and is given by

$$b = \left(\frac{2}{\pi}\right) \arctan\left(\frac{2d}{\Delta\bar{\nu}}\right). \quad (9)$$

However, another problem occurs when the profiles are much narrower than the grid intervals, i.e. when  $\Delta\bar{\nu} \ll w$ , where  $w$  is the grid interval in  $\text{cm}^{-1}$ , which is likely to happen at low pressures when the lines are very narrow. On average, most profiles will fall between grid points and only the far wings will be sampled, or even missed completely because of the truncation discussed above, so such profiles will be undersampled or not sampled at all. In these cases, the line centers should be moved to the nearest grid point, but this will overcompensate and cause the lines to be overestimated in strength. This is because the profile is effectively replaced by a triangle whose apex is the profile's peak, which has a larger area than the original profile. In this case, the integrated strength causes the profile to appear to be too strong, so the normalization factor must reduce the total strength. After taking account of the small absorption in the two grid points immediately adjacent to the grid point at the center of the profile, the normalization factor used in eq. (8) is given by

$$b = \left(\frac{\pi}{4}\right) \left(\frac{\Delta\bar{\nu}}{w}\right) \left[\frac{4 + (\Delta\bar{\nu}/w)^2}{2 + (\Delta\bar{\nu}/w)^2}\right], \quad (10)$$

where in this case  $b$  is less than unity and the criterion that  $\Delta\bar{\nu} < w^2/2$  is satisfied. In these cases, truncating the wings is done simply to avoid unnecessary computation, and the truncation is performed sufficiently far out in the wings so as not to affect eq. (10), and if necessary may exceed the distance  $d$  using the criterion based on the total gas

pressure mentioned above. In the limit of very small widths, the contributions made by the two grid points adjacent to the profile’s center become negligible, and the right hand side of eq. (10) reduces to  $\pi\Delta\bar{\nu}/2w$ .

The isotopic shifts of the energy levels of atoms are negligibly small (typically, one part in ten thousand), and can be ignored. For the molecules, the isotopic shifts can be significant, and can affect both the partition function and the spectral lines. However, the effect on the partition function is relatively small for the molecules of interest, as previously mentioned, and most molecules are dominated by one major isotope, so calculations can be simplified considerably by using only the partition function of the most abundant isotope for all isotopic forms. In the case of spectral lines the isotope effects need to be considered, and separate sets of shifted lines should be calculated for each isotopic version. Many sources of line data already incorporate the isotopically shifted lines with their fractional abundances included with the line strengths, but when such data are not available, the isotopic shifts have to be specifically calculated (see eq. 7).

In calculating models of brown dwarfs and extrasolar giant planets, the monochromatic opacities produced by the species known to be important sources of absorption are required at the temperature and pressure at each level in the model. For an object relatively remote from its parent star where stellar irradiation is unimportant, the majority of the radiation is in the infrared, where molecules such as  $CH_4$  and  $H_2O$  have strong vibration-rotation (and in the case of the latter also pure rotation) absorption, but are relatively transparent in the visible and the near ultraviolet parts of the spectrum. This is because these molecules have stable closed electron shells, and only highly excited electronic states exist above the ground state. At the temperatures of interest the population of these levels is negligibly small, and transitions from the ground state to these excited states lie further in the ultraviolet, where the flux is negligibly small, so ultraviolet opacities are unimportant. In the case of a substellar object orbiting close to its parent star, it can be irradiated at short wavelengths, which can affect its modeling, so ultraviolet opacities are required.

For those opacity sources that do not require much processing time, they can be calculated “on the fly” as required. This includes all calculations of processes that produce continuous absorption, such as bound-free processes, those where the data can be obtained in the form of a smoothed absorption of a band system, and where a relatively small number of spectral lines have to be individually computed.

For those atomic and molecular species for which data are available containing millions of spectral lines that have to be individually computed, the processing time per thermodynamic point can be too long, of the order of 30 minutes on a modern computer with a processor speed of about 2 GHz, for them to be calculated on the fly. In these cases a good option is to generate a large number of files containing pre-computed monochromatic opacities for each species for a range of temperatures and pressures. Then, interpolation can be performed at the time the opacities are required. A good choice would be to consider 50 logarithmic steps in temperature from 50 K to 3000 K, and 50 logarithmic steps in pressure from  $1.00 \times 10^{-7}$  to  $3.16 \times 10^2$  atmospheres. Each table would consist of monochromatic opacities in  $\text{cm}^2 \text{species}^{-1}$  over a range of wavenumbers. For those opacities important in the infrared, a suitable tabulation could be from  $100 \text{ cm}^{-1}$  to  $30,000 \text{ cm}^{-1}$  in steps of  $1 \text{ cm}^{-1}$  ( $100 \mu\text{m}$  to  $0.33 \mu\text{m}$ , respectively), which would include the visible part of the spectrum when data are available. For those that are important sources in the visible and ultraviolet parts of the spectrum, but not the infrared, the tabulation would cover a suitable range appropriate for the species (see the discussion in section §2.5), but starting from at least  $10,000 \text{ cm}^{-1}$  ( $1 \mu\text{m}$ ) in steps of  $2 \text{ cm}^{-1}$ . The suggested tabulation intervals in temperature, pressure, and wavenumber represent realistic compromises to render the data as accurately as possible with a manageable amount of processing time and memory, and interpolations in temperature and pressure should be accurate to one part in  $10^3$  or better.

Because opacities are usually confined to specific spectral regions, often with large sections of zero absorption on either side in the spectral range of interest, in many cases considerable disk space and processing time can be saved by noting the blank regions and not storing the zero data in these regions. This is particularly the case between the last non-zero grid point and  $30,000 \text{ cm}^{-1}$  for the relevant infrared opacities. Further savings can be made by not calculating and storing opacities of refractory species, such as  $TiO$ , below 1000 K, as their abundances would be too small to be of any relevance. In such cases very short dummy files can be generated, and when the opacities are obtained by interpolation, zero values are handled very quickly without having to read in any data.

### 2.1. HITRAN or GEISA-like Data

Several of the molecules that are important sources of opacity in brown dwarf and extrasolar giant planet atmospheres in the infrared have their data expressed in HITRAN (Rothman et al. 2003, 2005) or GEISA-like (Jacquinet-Husson et al. 1999, 2003, 2005) format. For the molecules of interest here, more extensive data are available from sources other than HITRAN or GEISA.

All HITRAN and GEISA-like line strengths are expressed in units of  $\text{cm species}^{-1}$ , which can be converted to the required strengths in  $\text{cm}^2 \text{s}^{-1} \text{species}^{-1}$  by multiplying by the velocity of light and various factors containing the Boltzmann factor and the partition function. Specifically, this can be written as

$$S = cS_h \frac{Q(T_o)}{Q(T)} e^{F(hc/kT_o - hc/kT)} \frac{(1 - e^{-hc\bar{\nu}/kT})}{(1 - e^{-hc\bar{\nu}/kT_o})}, \quad (11)$$

where  $S_h$  is the tabulated line strength in  $\text{cm species}^{-1}$  in HITRAN or GEISA format, and  $T_o$  is the HITRAN or GEISA reference temperature of 296 K. Thus,  $Q(T_o)$  is the partition function at that temperature. The term after the partition functions is the Boltzmann factor, after taking account of the Boltzmann factor at 296 K, and the last term is the stimulated emission correction factor, which has to allow for the correction factor at 296 K. Isotopes, when

relevant, are accounted for by their fractional abundances already being included in  $S_h$ , so no separate treatment is required. Some of the datasets give the transition moment or the Einstein A coefficient in addition to  $S_h$ , but this is unnecessary, except as a check on the data.

The line widths are calculated from broadening parameters using

$$\Delta\nu = \alpha \left( \frac{T_o}{T} \right)^\beta \frac{kT}{A_o} N_t, \quad (12)$$

where  $\Delta\nu$  is the full-width at half-maximum in  $\text{cm}^{-1}$ , as given in eq.(8),  $\alpha$  and  $\beta$  are two widths parameters, as given in the HITRAN or GEISA databases,  $A_o$  is the standard atmosphere in  $\text{dyne cm}^{-2}$ , and  $N_t$  is the total number density of particles in  $\text{cm}^{-3}$ . In practice for most of the temperatures and pressures of interest, most of the gas is in the form of  $H_2$  and  $He$ . So, it is convenient to assume that the broadening is the weighted average of these two gases. In the case of  $CO$ , the individual contributions due to  $H_2$  and  $He$  can be calculated, and the combined width is found from the weighted fractional abundances by number of these two gases. The individual values of  $\alpha$  are given, and  $\beta$  can be assumed to be 0.6 and 0.4, respectively, for  $H_2$  and  $He$ . With the widths calculated, the monochromatic absorption in  $\text{cm}^{-2} \text{ species}^{-1}$  across the spectrum can be calculated, as discussed in §2.

All the data in HITRAN or GEISA format cover the infrared part of the spectrum up to  $10,000 \text{ cm}^{-1}$ , and in some cases to up larger wavenumbers, subject to the available data, with the following molecules being discussed here:  $H_2O$ ,  $CH_4$ ,  $NH_3$ , and  $CO$ . Due to the availability of the data and some specific restrictions, several molecules require special treatment as discussed here.

$H_2O$  - Together with  $CH_4$ , this molecule is one of the most important sources of opacity in the infrared. Partridge and Schwenke (1997) and Barber et al. (2006) have very extensive databases, in addition to those in the latest versions of HITRAN (Rothman et al. 2005) and GEISA (Jacquinot-Husson et al. 2005), but it is likely that there are too many weak lines for calculations to be completed in a realistic period of time with typical computing resources available. In that case the lines can be binned in decades of line strength  $S_h$ , and only those lines stronger than a threshold value need be used in opacity calculations. A good compromise between realistic opacity calculations and processing time is with  $S_h \geq 1 \times 10^{-40} \text{ cm molecule}^{-1}$ . This results in a considerably reduced database, but still contains over forty million lines.

The partition function can be obtained from a 6<sup>th</sup>-order polynomial of the form

$$\ln(Q) = a + bx + cx^2 + dx^3 + ex^4 + fx^5 + gx^6, \quad (13)$$

where  $x = \ln(T)$ , and  $a$  to  $g$  are two sets of fitted coefficients for the ranges  $T \leq 500$  and  $T > 500$  K.

Figure 1 shows a plot of the monochromatic absorption of  $H_2O$  in the near infrared, together with  $CH_4$  and  $NH_3$ , as discussed later in this section, for a temperature of 1600 K and a total gas pressure of 10 atmospheres. It is seen that  $H_2O$  has strong absorption over this region, with a strong peak centered at about  $2.7 \mu\text{m}$ , and another broader peak centered at about  $6.4 \mu\text{m}$ . The double peak structure of some of the bands with a trough between them, is due to the gap between the  $P$ - and  $R$ -branches. Over most of the wavelength range plotted,  $H_2O$  is the strongest intrinsic absorber, and moreover, after  $H_2$ , which has no permanent dipole-allowed infrared absorption,  $H_2O$  is either the second or third most abundant molecular species over most of the temperatures and pressures of interest. Abundances are discussed in greater detail in §4. Figure 2 is a repeat of Fig. 1, but plotted on a larger wavelength scale and a slightly larger opacity scale, for the short wavelength side of Fig. 1.

$CH_4$  - This is the other significant source of opacity in the infrared, along with  $H_2O$ , for much of the temperatures and pressures of interest. As no single source of data covers the spectral region of interest, which extends into the visible part of the spectrum, the best approach is to merge data from three separate sources having four data files, taking account of overlapping frequency ranges in order to avoid duplicate lines, and incompatibilities with the data.

The main dataset covering lower frequencies up to  $6825 \text{ cm}^{-1}$  is available from Borysow et al. (2003), as used in our earlier work on  $CH_4$  (Burrows, Marley, & Sharp 2000), and contains over 17 millions lines. Brown et al. (1997) contains two files for the frequency coverage 4800 to 7698 and 8002 to 9199  $\text{cm}^{-1}$ . This is in addition to those in the latest versions of HITRAN (Rothman et al. 2005) and GEISA (Jacquinot-Husson et al. 2005). Laboratory studies of  $CH_4$  are reported in Robert et al. (2000) and Brown, Dulick & Devi (2001). In superimposing a plot of the lower range of the data from Brown et al. (1997) with that from Borysow et al. (2003), it is seen that the coverage of the lower range overlaps with the data from Borysow et al. (2003), but includes a large gap in coverage centered at about  $5850 \text{ cm}^{-1}$ , corresponding to a peak in the opacity in the data from Borysow et al. (2003). It can also be seen that as the the opacity from the Borysow et al. (2003) data tails off, it is overlapped by increasing opacity from the Brown et al. (1997) data, and corresponds to a band system that was not covered by the Borysow et al. (2003) data. This can be confirmed by looking at the opacity from Strong et al. (1993), which we used in our earlier work (Burrows, Marley, & Sharp 2000) to extend the opacity to higher frequencies. By a careful examination of the data, it can be seen that there is a small additional gap in coverage from Brown et al. (1997) below  $6356 \text{ cm}^{-1}$ . Where the data from Brown et al. (1997) has coverage below this point, it appears to duplicate the data from Borysow et al. (2003). However, the overlapping coverage at and above  $6356 \text{ cm}^{-1}$  appears to cover a different band system, so the data from Brown et al. (1997) below  $6356 \text{ cm}^{-1}$  should be discarded. A certain amount of judgment is required in deciding which lines to include from overlapping databases, and which to discard. This is decided by looking at plots of absorption at high resolution in overlapping regions.

The second file from Brown et al. (1997) with the higher frequency coverage presents no problem with duplication of any other files, and extends the opacity coverage of  $CH_4$  up to  $9199\text{ cm}^{-1}$ . In superimposing data from Strong et al. (1993), the peaks in absorption covered by the two sets of the data from Brown et al. (1997) are seen to match well, and the gap in coverage between the two files presents no problem, as it corresponds to a minimum in the opacity as seen in the Strong et al. data. As all three files are in the same format, and match each other together with the data from Strong et al., where there is overlap, the same code could be used for the whole range up to  $9199\text{ cm}^{-1}$  without any special treatment, with the data from Borysow et al. (2003) and Brown et al. (1997) joined together. A good place to join is at  $6356\text{ cm}^{-1}$ .

However, the upper frequency limit of  $9199\text{ cm}^{-1}$  is still too low because  $CH_4$  opacities are also important at shorter wavelengths. In our earlier work, when we did not have available data from Brown et al. (1997), the  $CH_4$  opacities could be extended continuously up to  $9495\text{ cm}^{-1}$  using data from Strong et al. (1993). This was followed by an unavoidable gap in coverage, until data from Karkoschka (1994) starting at  $10,000\text{ cm}^{-1}$  could be used. The data from Strong et al. and Karkoschka give only monochromatic opacities as a function of wavenumber or wavelength. The data from Strong et al. give a simple formula for calculating the temperature dependence of the opacity, but no pressure dependence, and the data from Karkoschka give no dependences at all. Consequently, various means of scaling could be devised to match these opacities with the data from Borysow et al. (2003).

However, the small range covered by Strong et al. (1993) beyond the upper limit from Brown et al. (1997) is probably not worth the extra work in including the former for a marginal gain. Additionally, without other information, there is little to be gained by attempting to fill in the gap in opacities using interpolation.

The data from Karkoschka (1994) cover the range from  $1\text{ }\mu\text{m}$  to  $0.3\text{ }\mu\text{m}$ , i.e. from about  $10,000\text{ cm}^{-1}$  to about  $33,300\text{ cm}^{-1}$ . However, shortward of  $0.4\text{ }\mu\text{m}$  (i.e.  $25,000\text{ cm}^{-1}$ ), the opacity includes gaps and in our judgement does not seem very reliable. Since its contribution to the opacity decreases with decreasing wavelength, whilst other processes become more important, the amount of processing and storage necessary to handle this section of data was not considered worthwhile.

As the data from Karkoschka (1994) have no pressure or temperature dependency, a simple method can be devised to match it to the rest of the data. As the monochromatic absorption over a number of wavelength points is given without any information on the lines producing this absorption, there is no way any pressure dependency can be determined. However, it is possible to adopt a simple scaling factor to adjust the absorption for different temperatures. The data provided by Karkoschka are applicable for  $160\text{ K}$ ; which is somewhat higher than the effective temperature of Jupiter. The strongest line in the upper of the two frequency ranges listed by Brown et al. (1997), as discussed above (in fact at  $8644.2322\text{ cm}^{-1}$ ), can have its strength calculated at  $160\text{ K}$ , then when opacities are calculated at some required temperature  $T$ , the ratio of the strengths at  $T$  and  $160\text{ K}$  can be used to scale the Karkoschka opacities. This very simple scaling will at least allow the Karkoschka data to follow the trend of the other data with changing temperatures.

Following Herzberg (1968), the partition function for  $CH_4$  can be calculated from

$$Q(T) = \frac{4}{3} \sqrt{\pi} e^{hcB/4kT} \left( \frac{kT}{hcB} \right)^{\frac{3}{2}} \left( 1 + \frac{15}{4} \frac{hc}{kT} \frac{D}{B^2} \right) \prod_{i=1}^4 \frac{1}{(1 - e^{-hc\omega_i/kT})^{d_i}}, \quad (14)$$

where  $B$  and  $D$  are the rigid rotational and the non-rigid correction constants in  $\text{cm}^{-1}$  for the spherical top model of  $CH_4$ ,  $\omega_i$  is the vibrational harmonic constant of the  $i^{\text{th}}$  vibrational mode, of which there are four, and  $d_i$  is the corresponding degeneracy of that mode, such that for the four modes the degeneracies are 1, 2, 3, and 3, respectively. This formula neglects higher-order effects, such as anharmonicity and vibration-rotation coupling, and only the partition function of  $^{12}CH_4$  is calculated, with the differences for  $^{13}CH_4$  being neglected due to the low abundance of  $^{13}C$  (approximately one part in a hundred).  $CH_4$  is the best known example of a spherical top molecule, where the three principle moments of inertia are the same, as are, hence the rigid rotational constants. The rotational and vibrational constants are well known, and can be obtained from many sources, such as Herzberg (1966) or the JANAF tables (Chase et al. 1985).

An example of joining together the data from different sources is the monochromatic absorption of  $CH_4$ , shown in Figs. 1 and 2; in several places, it fills in windows in the absorption of  $H_2O$ . The strongest band in the wavelength range shown is centered just above  $3.3\text{ }\mu\text{m}$ , where the central peak between the  $P$ - and  $R$ -branches is due to the  $Q$ -branch. As discussed in more detail in §4, Fig. 17 shows that  $CH_4$  is only slightly less abundant than  $H_2O$  at low temperatures, due to the lower abundance of carbon compared to oxygen.

$NH_3$  - This is the third most important molecule at low temperatures, after  $H_2O$  and  $CH_4$ . Data are available from Brown et al. (2000) listing over 34,000 lines from below  $1\text{ cm}^{-1}$  to over  $7000\text{ cm}^{-1}$ . Unlike the other two molecules, no special treatment is required, and a set of precomputed files for a suitable set of temperatures and pressures, as discussed above, can be generated relatively rapidly. Even though  $NH_3$  is important in giant planet atmospheres, suitable sources of data for a spectral coverage to shorter wavelengths do not appear to be readily available.

Like  $H_2O$ , the partition function can conveniently be calculated from a polynomial fit in the same form as eq. (13) for a 6-<sup>th</sup> order polynomial, using available numerical values in the range  $50 \leq T \leq 3000\text{ K}$  for the isotope  $^{14}NH_3$ . This covers the whole temperature range that is likely to be of interest. As before, other isotopic versions of nitrogen can be neglected, with the next most abundant isotope,  $^{15}N$ , comprising only  $\sim 0.4\%$  of total nitrogen.

As with  $H_2O$  and  $CH_4$ , the monochromatic absorption of  $NH_3$  is plotted on Figs. 1 and 2. For most of the wavelengths shown,  $NH_3$  is an intrinsically weaker opacity source than  $H_2O$  and  $CH_4$  over most wavelengths, and



additionally it is less abundant than the other two molecules because nitrogen is less abundant than carbon or oxygen. Nevertheless, it is still a relatively important opacity source in the infrared, and has a strong absorption peak at about  $10.5 \mu\text{m}$ , where its absorption exceeds  $H_2O$  and  $CH_4$  by a large amount. As with  $H_2O$  and  $CH_4$ , the abundance of  $NH_3$  is plotted on Fig. 17, which is discussed in more detail in §4.

*CO* - Although in principle *CO* is a non-refractory molecule like the three discussed above, below about 1200 K, depending on the pressure, it is superseded in abundance by  $CH_4$ ; its abundance becomes very small below about 800 K, if equilibrium is assumed. Nevertheless, a full set of opacities for temperatures down to 50 K should still be computed if non-equilibrium calculations are required. The data are available from HITRAN (Rothman et al. 2003, 2005) and GEISA (Jacquinet-Husson et al. 1999, 2003, 2005), which can be used to calculate the absorption from 3 to nearly  $8500 \text{ cm}^{-1}$  in the infrared for about 99,000 transitions covering the pure rotational, and the fundamental (first harmonic), second, third and fourth harmonic vibration-rotation bands. Unlike the polyatomic molecules mentioned above, there are relatively few lines of *CO* due to the fact that the ground electronic state is a  $^1\Sigma$  state, and each band consists of a single *P*- and *R*-branch. The other isotopic forms, the most important of which is  $^{13}C^{16}O$ , make relatively small contributions to the opacity when compared with the main isotopic form  $^{12}C^{16}O$ . There are large gaps between the bands with negligibly small opacities.

The partition function can be obtained from eq. (3) and asymptotic formulae for the vibrational and rotational contributions. Because only the ground electronic state contributes any significant fraction to the partition function, and because it is just a singlet  $\Sigma$  state, there is no summation in eq. (3), which reduces to just the product of the vibrational and rotational contributions of the ground state. The spectroscopic constants used to calculate the partition function can be obtained from Huber & Herzberg (1979).

The monochromatic absorption of *CO* at 1600 K and a total gas pressure of 10 atmospheres is shown in Fig. 3, together with  $PH_3$  and  $H_2S$ , which are briefly discussed in §2.4. *CO* is the only diatomic molecule shown here and in the previous figures, and has a particularly simple spectrum, with only simple *P*- and *R*-branches, which are easily seen in the strong absorption feature centered at about  $4.67 \mu\text{m}$ . This corresponds to the fundamental vibration-rotation band and the associated “hot” bands, and is the strongest feature in its infrared absorption spectrum. The weaker bands at shorter wavelengths correspond to the second, third, and fourth harmonics with progressively decreasing wavelengths. Although *CO* has some strong absorption, particularly around the  $\sim 4.5\text{--}5.5\text{-}\mu\text{m}$  region where it exceeds the intrinsic absorption of the molecules discussed so far, the absorption is confined to relatively narrow spectral regions, with very low absorption in other places; it is not a particularly important opacity source in the infrared. Figure 17 shows that it replaces  $CH_4$  at higher temperatures, as discussed in more detail in §4.

## 2.2. Heavy Metal Oxides

The oxides of transition metals, where “metals” are used here in a chemical, rather than an astrophysical, sense, form a well defined group with many similar physical, chemical, and spectroscopic properties. Of these, *TiO* and *VO* are by far the most important sources of opacity over the upper regions of the temperatures of interest.

*TiO* - Because compounds involving titanium are refractory, gas-phase species of titanium do not exist at low temperatures. Thus, both processing time and memory can be saved by not calculating opacities below 1000 K. Unlike many volatile gaseous species like  $H_2O$ , where vibration-rotation transitions are the main source of absorption in the infrared, the opacity of *TiO* in the infrared, as well as in the visible, is due to transitions between different electronic states. Two important sets of data of *TiO* can be found in Allard, Hauschildt, & Schwenke (2000) and Plez (1998), with the data for the former being in a HITRAN or GEISA-like format, similar to the data for the molecules discussed in §2.1.

The dataset from Allard, Hauschildt, & Schwenke (2000) lists about 12 million lines in one large file from 3 to nearly  $30,000 \text{ cm}^{-1}$ , covering the whole infrared and visible parts of the spectrum for the transitions of the most abundant isotope  $^{48}TiO$ , together with  $^{46}TiO$ ,  $^{47}TiO$ ,  $^{49}TiO$ , and  $^{50}TiO$ , for the seven different electronic band systems  $\alpha(C^3\Delta-X^3\Delta)$ ,  $\beta(C^1\Phi-a^1\Delta)$ ,  $\gamma(A^3\Phi-X^3\Delta)$ ,  $\gamma'(B^3\Pi-X^3\Delta)$ ,  $\delta(b^1\Pi-a^1\Delta)$ ,  $\epsilon(E^3\Pi-X^3\Delta)$ , and  $\phi(b^1\Pi-d^1\Sigma)$ . Because all the data are contained in one file, no provision is required to handle the isotopes or the electronic transitions separately. Also, because the data are given in a HITRAN or GEISA-like format, the line strengths and widths are calculated with the same methods discussed in §2.1.

The data from Plez (1998) are contained in five files for each of the isotopes for nine electronic systems, i.e. those listed immediately above, plus two additional systems. The data for  $^{48}TiO$  has about 3 million lines covering the range from about  $2800 \text{ cm}^{-1}$  to about  $29,000 \text{ cm}^{-1}$ , and is more restricted for the other isotopes. The line strengths are expressed as *gf* values, and, given the excitation energy of the lower state and transition frequency, the line strength can be calculated directly from eq. (1). However, no information is available for line broadening, so a simple formula based on the rotational quantum number is used, namely

$$\Delta\nu = [w_0 - \min(J'', 30)w_1] kTN_t/A_o, \quad (15)$$

where  $w_0$  is the full-width at half-maximum of a transition at 1 atmosphere when the lower rotational quantum number,  $J''$ , is zero, and  $w_1$  is a coefficient that governs the dependancy of the line width on  $J''$ , with the broadening at  $J'' = 30$  being used for larger values of  $J''$ . Numerical values of 0.1 and 0.002 are adopted for  $w_0$  and  $w_1$ , respectively, and in the absence of a suitable theory, appear to give realistic broadening for a number of molecules whose line broadening parameters are not available. This somewhat *ad hoc* approach is in general agreement with experimental observations, where broadening increases with  $J''$  up to some limit (see, for example, Varanasi & Chudamani 1989).

If the opacities of *TiO* using the two sources of data are compared, a significant and consistent discrepancy between the two sources of data and methods employed is found, with the absorption from Allard, Hauschildt, & Schwenke (2000) being about two orders of magnitude higher than Plez (1998) for a number of test calculations at different temperatures and pressures. It was discovered that an additional factor of  $2J'' + 1$  had been included in the line strengths from the former, and when this factor in the tabulated values is divided out before calculating the absorption, the agreement between the two sources is good. (The fact that the highest tabulated values of  $J$  were about 100, means that the average value of  $2J'' + 1$  is also about 100, which explains this discrepancy.) Because Allard, Hauschildt, & Schwenke provide more extensive coverage, as well as information on line broadening, it is recommended that one use these data, after correcting for the  $2J'' + 1$  factor, even though the data cover seven rather than nine electronic systems.

The partition function of *TiO* can be obtained by interpolating the table given by Jørgensen (1997), which tabulates it for a range of temperatures between 200 and 8000 K based on 7 electronic states. The coefficients  $a$ ,  $b$ ,  $c$ ,  $d$ ,  $e$ , and  $f$  can be fitted to the expression

$$\log_{10} Q(T) = aT^{-1} + b + cT + dT^2 + eT^3 + fT \ln(T), \quad (16)$$

for each tabulated value in the range  $200 \leq T \leq 8000$  K, then any partition function for a temperature in this range can be obtained. Alternatively, Schwenke (1998) gives some very detailed spectroscopic data for a large number of electronic states which can be used to obtain the partition function.

Figures 4, 5, and 6 show the monochromatic absorption of *TiO* and *VO* at progressively larger scales at a temperature of 2200 K and a total pressure of 10 atmospheres. As discussed in more detail in §4, Fig. 17 shows the abundances of *TiO* and *VO* at a total pressure of 1 atmosphere. The sudden decrease with falling temperature is due to the formation of condensates (Burrows & Sharp 1999).

*VO* - Data on this molecules can be found in Plez (1998), where they are given in the same format as *TiO* in that reference.

As with the other molecules, a set of opacity files can be precomputed, but like *TiO* it is a refractory species, so temperatures below 1000 K need not be considered. Also like *TiO*, the opacity is produced by electronic transitions, and covers a large region of the infrared, as well as parts of the visible spectrum. The line data consist of over 3 million lines from nearly  $3800 \text{ cm}^{-1}$  to nearly  $26,000 \text{ cm}^{-1}$  with the  $gf$  values of the lines being given, together with the other necessary data, including the value of  $J''$  for each transition for the  $A^4\Pi - X^4\Sigma^-$ ,  $B^4\Pi_r - X^4\Sigma^-$ , and  $C^4\Sigma^- - X^4\Sigma^-$  band systems. The line strengths can be calculated using eq. (1). No information on line broadening is available, so, as with *TiO* when the Plez (1998) data are used, eq. (15) can be employed to calculate the broadening. The isotopic version  $^{51}\text{VO}$  is by far the most abundant, so other isotopes need not be considered. The partition function can be calculated using eq. (3), with the spectroscopic constants for the ground and first few excited electronic states taken from Huber & Herzberg (1979).

Because the behavior of *VO* is so similar to *TiO*, it is included on the same opacity plots in Figs. 4, 5, and 6 and abundance plots in Figs. 17 and 22. The opacity figures show that it has the same general trend as *TiO*, though the band positions are at different wavelengths.

### 2.3. Metal Hydrides

A major source of molecular opacity is the metal hydrides, where as in §2.2 “metals” are used in a chemical, rather than an astrophysical, sense. The role played by metal oxides such as *TiO* is well known, and although the absorption of metal hydrides is often less than the oxides for a solar composition, to zeroth order the abundances of the hydrides at a given temperature and pressure (thus gravity) are approximately linearly dependent on  $Z$ , the metallicity (in the astrophysical sense), whereas the abundance of the oxides can very approximately scale as the square of  $Z$ , because two elements other than hydrogen and helium are involved. The consequence of this is that for mixtures with a Population II value of  $Z$ , the hydrides are relatively more important.

The opacities of the hydrides *TiH*, *CrH*, *FeH*, *MgH*, and *CaH* can be calculated using various methods, depending on the available data. The characteristics of these molecules are broadly similar, and all involve electronic transitions in the visible and infrared parts of the spectrum. As with *TiO* and *VO*, because of the large number of lines involved, it is recommended, as before, to precompute sets of files for a grid of the same temperatures and pressures. For comparison, opacities of all five metal hydrides are plotted in Fig. 7 at 1800 K and a total gas pressure of 10 atmospheres. Because they have low moments of inertia, and thus large rotational constants, the rotational fine structure is visible in several of the bands at the scale used here. For comparison, the abundances of the molecules are plotted together on Fig. 18 for a total pressure of 1 atmosphere, as discussed in §4.

*TiH* - The line frequencies and strengths of the  $A^4\Phi - X^4\Phi$  and  $B^4\Gamma - X^4\Phi$  electronic systems of *TiH* are available from detailed quantum mechanical calculations, as described by Burrows et al. (2005), and include the spectroscopic data and the Hönl-London factors for the two quartet electronic transitions. The calculations there are based on the data on about 91,000 and 101,000 lines for the  $A^4\Phi - X^4\Phi$  and  $B^4\Gamma - X^4\Phi$  systems, respectively. The lines for the  $A - X$  system are based on 20 bands with  $v' = 0, 1, 2, 3, 4$  and  $v'' = 0, 1, 2, 3$ , and 24 bands for the  $B - X$  system with  $v' = 0, 1, 2, 3$  and  $v'' = 0, 1, 2, 3, 4, 5$ . Bands with the same value of  $\Delta v = v' - v''$  generally strongly overlap giving, the appearance of one band, unless the resolution is high enough to resolve the individual rotational components, so the general appearance of a spectrum is given by different sequences of  $\Delta v$ . In the case of the  $A - X$  system, 8 sequences are calculated with  $\Delta v$  taking on values in the range of -3 to 4, and for the  $B - X$  system 9 sequences are calculated

with  $\Delta v$  taking on values in the range of -5 to 3. For both systems in any transition, the value of  $\min(J', J'') \leq 50\frac{1}{2}$  is satisfied. The two systems overlap, giving continuous coverage from about  $5000 \text{ cm}^{-1}$  to  $24,000 \text{ cm}^{-1}$  (about  $2 \mu\text{m}$  to  $0.42 \mu\text{m}$ ). The line strengths are given in terms of the Einstein  $A$  coefficients, which can be converted to the required integrated line strength using

$$S = \frac{A}{8\pi\bar{\nu}^2} (2J' + 1) \frac{e^{-hcF''/kT}}{Q(T)} \left[ 1 - e^{-hc(F' - F'')/kT} \right], \quad (17)$$

where  $J'$  is the rotational angular momentum quantum number of the upper state. The Einstein  $A$  coefficient for each line in the input data is given by

$$A = A_{v',v''} S_{J',J''} / (2J' + 1), \quad (18)$$

where  $A_{v',v''}$  is the Einstein  $A$  coefficient for the whole  $v' - v''$  band, and  $S_{J',J''}$  is the Hönl-London for the  $J' - J''$  rotational transition, including the spin substates. A number of values of  $A_{v',v''}$  for both electronic transitions are listed in Table 2 of Burrows et al. (2005). Unlike  $TiO$ , where data on several isotopic versions are available, for  $TiH$ , only data on the main isotopic version  $^{48}TiH$  are available, so the isotopic shifts for the forms containing  $^{46}Ti$ ,  $^{47}Ti$ ,  $^{49}Ti$ , and  $^{50}Ti$ , have to be calculated, using eq. (7), and the methods briefly discussed in §2. The quantum numbers of the levels involved are known, together with the vibrational and rotational constants from Burrows et al. (2005) for the three electronic states, of which the pair  $X$  and  $A$  or  $X$  and  $B$  participate in a given transition. Although the shift of the lines of  $TiD$  is large, even when deuterium has not been destroyed by nuclear burning, at best, it has an abundance of about five orders of magnitude below normal hydrogen, so its isotopic shift, and equivalently, those of the other hydrides, is not required.

The terrestrial isotopic fraction of  $Ti$  in the form of  $^{48}Ti$  is 0.738, so this factor should be applied to eq. (17) for the main isotopic version. For the other isotopes,  $^{46}Ti$ ,  $^{47}Ti$ ,  $^{49}Ti$ , and  $^{50}Ti$ , the corresponding factors of 0.08, 0.073, 0.055, and 0.054, respectively, can be applied to eq. (17), together with the shifted values of  $\bar{\nu}$ ,  $F''$ , and  $F'$ . However, no account is taken of the slight changes in the Einstein  $A$  coefficient due to the shifts of the levels, as discussed in §2. Likewise, the isotopically shifted partition functions are not considered. The lines widths are calculated using eq. (15) with the same coefficients.

In addition to Fig. 7, the opacities of  $TiH$  are plotted on a larger scale in Fig. 8, together with  $FeH$  and  $CrH$ . The  $A - X$  system covers an extensive region in the near infrared longward of about  $0.65 \mu\text{m}$ , where it follows a trend very similar to  $FeH$  and  $CrH$ , which strongly overlaps it. There are several strong peaks, of which the strongest is at about  $10,500 \text{ cm}^{-1}$  or  $\sim 0.94 \mu\text{m}$ . This corresponds to the overlapping of many  $\Delta v=0$  bands, i.e. the 0-0, 1-1, 2-2 etc. transitions. The next strongest bands at a shorter wavelength correspond to the overlapping of many  $\Delta v=1$  bands, i.e. the 1-0, 2-1, 3-2 etc. transitions, and likewise the next strongest bands at a still longer wavelength are due to the overlapping of the  $\Delta v=-1$  bands, i.e. the 0-1, 1-2, 2-3 etc. transitions. Most of the band heads are on the  $R$ -branches because  $B' < B''$ , as can be seen by the absorption dropping off more rapidly shortward of the peak than at longer wavelengths; however, for the peak at the longest wavelength here corresponding to the  $\Delta v=-3$  sequence the band heads are on the  $P$ -branches. This band is particularly interesting. When  $TiH$  is present,  $H_2O$  is also present and “competes” with  $TiH$  absorption; most of the peaks of the bands in the  $A - X$  system coincide with maxima in the bands of  $H_2O$ . In the case of the  $\Delta v=-3$  sequence, this happens to coincide with a trough in  $H_2O$  absorption, and appears to be somewhat stronger than the general trend. This band system may be a good candidate for detection in brown dwarfs.

The  $B - X$  system covers a more restricted range at shorter wavelengths, but with a narrow and very strong peak at about  $19,000 \text{ cm}^{-1}$  or  $0.53 \mu\text{m}$  in the yellow part of the visible spectrum, as can be seen in Fig. 8, where  $TiH$  has its highest absorption for both the band systems. As with the  $A - X$  system, the various peaks are caused by the overlapping sequences for a given value of  $\Delta v$ . This is a general characteristic for most electronic band systems with  $|\Delta v|$  being zero or a small integer. Although as stated earlier the band systems overlap, there is a substantial minimum between the maxima of the two systems at about  $14,300 \text{ cm}^{-1}$  or  $0.7 \mu\text{m}$  in the red part of the visible spectrum.

The partition function can be calculated from eq. (3) using the spectroscopic data of the 15 electronic states listed in Tables 11 and 12 of Burrows et al. (2005), including the  $X$ ,  $A$ , and  $B$  states used to calculate the opacity. Since the energy levels of the four spin substates of the  $X$  electronic state are available, these can be treated as four separate states for calculating the partition function, so the sum can be performed over 18 states. The calculated values of the partition function at 200 K intervals from 1200 to 4800 K are listed in Table 13 of Burrows et al. (2005). As previously, only the partition function for the main isotopic version need be calculated. The variation of the abundance with temperature at a gas pressure of 1 atmosphere is show in Fig. 18, discussed in more detail in §4.

$CrH$  - As discussed in Burrows et al. (2002), this molecule plays an important role in L dwarfs and sunspots. The calculations investigated here are based on the  $X^6\Sigma^+ - A^6\Sigma^+$  system using 12 bands with  $v' = 0, 1, 2$ , and  $v'' = 0, 1, 2, 3$ , with  $\min(J', J'') \leq 30\frac{1}{2}$ , giving rise to 6  $\Delta v$  sequences in the range of -3 to 2. For each band, 6 strong main  $P$ - and  $R$ -branches are available, corresponding to each of the 6 spin substates, together with 18 weaker satellite bands. This yields a relatively modest number of about 13,800 lines between about  $6200 \text{ cm}^{-1}$  and  $14,500 \text{ cm}^{-1}$ . As both electronic states are  $\Sigma$  states, i.e. have an orbital angular momentum quantum number  $\Lambda=0$ , they are strictly Hund’s case (b) (Herzberg 1950) coupling, so a rotational quantum number apart from electron spin,  $N$ , can be defined. However, the net electron spin of  $5/2$  does interact, giving rise to 6 values of  $J$  for a given value of  $N$  from

$J = N + 5/2$ ,  $J = N + 3/2$ ,  $J = N + 1/2$ ,  $J = N - 1/2$ ,  $J = N - 3/2$ , and  $J = N - 5/2$ , which have slightly different energies. The effect of the splitting of these levels is to increase the contribution to the opacity.

The main isotope is  $^{52}\text{CrH}$  with an isotopic fraction of 0.83, with the other isotopic versions of any significance being  $^{50}\text{CrH}$ ,  $^{53}\text{CrH}$ , and  $^{54}\text{CrH}$ , and having fractions of 0.044, 0.10, and 0.02, respectively. As with  $\text{TiH}$ , eq. (17) can be used to calculate the line strengths in  $\text{cm}^2\text{molecule}^{-1}$  using the Einstein  $A$  coefficients given by eq. (18), with the line widths and isotopic shifts being calculated similarly.

Unfortunately, only the  $X$  and  $A$  electronic states used to calculate the opacity are readily available for calculating the partition function. The partition function for isotopically substituted  $\text{CrH}$  is the same as that derived under the assumption that chromium is pure  $^{52}\text{Cr}$  to within  $\sim 0.3\%$ . The monochromatic absorption of  $\text{CrH}$  is replotted on a larger scale in Fig. 8, together with  $\text{TiH}$  and  $\text{FeH}$  at 1800 K and a total pressure of 10 atmospheres, and its abundance as a function of temperature at a gas pressure of 1 atmosphere is shown in Fig. 18, together with the other metal hydrides.

$\text{FeH}$  - In Dulick et al. (2003), details were given for the calculation of  $\text{FeH}$  opacities produced by the  $F^4\Delta_i - X^4\Delta_i$  (Wing-Ford) system, which are briefly discussed here. A total of 25 bands with both  $v'$  and  $v''$  taking values of 0, 1, 2, 3, and 4, with 9 sequences of  $\Delta v$  in the range of -4 to 4, and with the rotational quantum numbers limited by  $\min(J', J'') \leq 50\frac{1}{2}$  for the four spin substates, were provided. This yields a total of about 116,000 transitions in the range from about  $2000\text{ cm}^{-1}$  in the infrared to  $16,000\text{ cm}^{-1}$  in the red part of the visible spectrum, i.e.  $5\text{ }\mu\text{m}$  to  $0.625\text{ }\mu\text{m}$ , respectively.

Major problems with the  $\text{FeH}$  Wing-Ford system are that  $\text{FeH}$  itself is not easily studied in the laboratory, and both the  $F^4\Delta_i$  and  $X^4\Delta_i$  electronic states are intermediate between Hund's (a) and (b) coupling cases (Herzberg 1950), with the coupling changing with  $J$ . Moreover, the rotational levels are perturbed by unknown electronic states. For Hund's case (b) coupling, the situation is like  $\text{CrH}$ , as discussed above, with  $N$  being a well-defined quantum number representing rotation before electron spin is added, except that the net electron spin is  $3/2$ , yielding four values of  $N$  for a given  $J$ , i.e.,  $J = N + 3/2$ ,  $J = N + 1/2$ ,  $J = N - 1/2$ , and  $J = N - 3/2$ ; the selection rules are  $\Delta N = 0, \pm 1$  and  $\Delta J = 0, \pm 1$ . Of the 28 branches corresponding to allowed combinations of  $\Delta J$  and  $\Delta N$ , there are four each of the main  $P$ -,  $Q$ -, and  $R$ -branches with  $\Delta J = \Delta N$ , which are the strongest branches, with the remainder being weaker satellite branches. Table 4 in Dulick et al. (2003) lists the Hönl-London factors of all 28 branches. It is worth noting that for the four  $P$ - and  $R$ -branches, the Hönl-London factors scale as  $O(J)$ , but for the others they scale as  $O(J^n)$ , where the integer  $n = -1$  or is greater than 0.

For Hund's (a) coupling, the quantum number  $\Omega = \Lambda + \Sigma$  is defined, and is the sum of orbital angular momentum quantum number ( $\Lambda$ ), where  $\Lambda = 2$  here for the  $\Delta$  states, and the projection of the net electron spin on the internuclear axis ( $\Sigma$ ), where  $\Sigma = -3/2, -1/2, 1/2$ , and  $3/2$  for quartet states. Hence,  $\Omega$  takes the values  $1/2, 3/2, 5/2$ , and  $7/2$ . The selection rules are such that  $\Delta\Lambda = 0$  and  $\Delta J = 0, \pm 1$ , so there are 12 branches, i.e., 4  $P$ -,  $Q$ -, and  $R$ -branches for the different spin substates, with the Hönl-London factors for these being given in Table 3 of Dulick et al. (2003). Note that the  $P$ - and  $R$ -branches are strong, and scale as  $O(J)$ , whereas the  $Q$ -branches are weak and scale as  $O(J^{-1})$ , as is the case with the case (b) coupling. The general intermediate coupling between Hund's cases (a) and (b) is very complicated for quartet states, and depends on spin-orbit and spin-spin interactions. Instead, intermediate coupling was determined by fitting to experimental results, as discussed in Dulick et al. (2003), for both the intensities and the term values for a number of selected vibrational levels. The latter are listed in Tables 8a to 8j in Dulick et al. (2003) for the  $X$  and  $F$  states, then used to calculate the opacity. The use of the Einstein  $A$  coefficients together with the treatment of broadening are exactly the same as  $\text{TiH}$  and  $\text{CrH}$  covered above. The main isotope is  $^{56}\text{FeH}$ , with a fractional abundance 0.917, the other isotopic forms are  $^{54}\text{FeH}$ ,  $^{57}\text{FeH}$ , and  $^{58}\text{FeH}$ , which have fractional abundances of 0.058, 0.022, and 0.028, respectively, and, as previously, the treatment is the same.

The partition function can be calculated for the main isotopic version with the data for the energies of the electronic states listed in Table 9a of Dulick et al. (2003), and the vibrational and rotational constants of these states can be obtained from Table 9b of the reference. A total of 10 states are listed in Dulick et al. (2003), including the  $X$  and  $F$  states, and the individual energies of several spin substates in Table 9a are given, yielding 29 states or substates included in the summation of eq. (3). Table 9c in that reference compares analytic values between 1000 and 3500 K from eq. (3) with direct summation of the levels. It is found that the values from direct summation are always less, ranging from 78% of the values at 1000 K, to only about 30% of the value at 3500 K, by which time  $\text{FeH}$  has for all practical purposes completely dissociated. As direct summations will always underestimate a partition function when levels are omitted, whereas analytic solutions allow for them, we have reason to believe that the analytic results are more accurate. As with  $\text{TiH}$  and  $\text{CrH}$ ,  $\text{FeH}$  is replotted on a larger scale in Fig. 8 at 1800 K and 10 atmospheres total gas pressure, and its abundances as a function of temperature at a gas pressure of 1 atmosphere are plotted on Fig. 18, along with the other metal hydrides. See §4 for more details.

$\text{MgH}$  - Data for the  $X^2\Sigma^+ - X^2\Sigma^+$  pure rotation and vibration-rotation transitions in the infrared, the  $B'^2\Sigma^+ - X^2\Sigma^+$  electronic transitions in the visible, and the near-ultraviolet spectrum are available from Skory et al. (2003), and the  $A^2\Pi - X^2\Sigma$  electronic transitions, also in the visible and near ultraviolet, are available from Weck et al. (2003a).

Before the  $X - X$  pure rotation and vibration-rotation bands can be calculated, a file containing the energy levels and the corresponding vibrational and rotational quantum numbers from Weck et al. (2003a) should be combined with the file containing the transitional energies, Einstein  $A$  coefficients, and the corresponding quantum numbers from Skory et al. (2003), by matching up the quantum numbers. The same procedure should be performed for the  $A - X$  and  $B' - X$  systems. However, an additional complication is that the resultant line lists are not in general

sorted in order of ascending rotational quantum numbers for a given pair of vibrational quantum numbers, which in turn are not in general ordered in ascending values. For the previous hydrides, this is the case, and can result in the saving of a considerable amount of processing time when calculating isotopic shifts; thus, the data should be resorted before proceeding.

The data for the  $X - X$  system contain a list of over 2500 lines from the far infrared up to just above  $10,000 \text{ cm}^{-1}$  or  $1 \mu\text{m}$ . The small number of lines below  $100 \text{ cm}^{-1}$  are completely swamped in the far IR by  $H_2O$  and  $CH_4$  (by more than three orders of magnitude) and can be ignored. The data for the  $A - X$  system contains over 10,000 lines from about  $9,000 \text{ cm}^{-1}$ , i.e.  $1.1 \mu\text{m}$ , thus overlapping with the upper end of the  $X - X$  system, up to about  $32,000 \text{ cm}^{-1}$  in the near ultraviolet. The dataset for the  $B' - X$  system has about the same number of lines, and covers almost exactly the same spectral region as the  $A - X$  system, except that it starts at a slightly shorter wavelength and is missing an overlap with the  $X - X$  system. Thus, there are no gaps in the spectral coverage between the three systems.

As with the other hydrides discussed, the same methods can be used to calculate the line strength with the Einstein  $A$  coefficients, together with the line broadening and the isotopic shifts. Because only data for the most abundant isotope  $^{24}\text{MgH}$  are readily available, the shifted lines for the minor isotopic forms  $^{25}\text{MgH}$  and  $^{26}\text{MgH}$  should be calculated, taking account of the isotopic abundances, when line strengths are calculated using the reordered data.

The partition functions can be calculated using the spectroscopic data for the  $X$ ,  $A$ , and  $B'$  electronic states. Since the  $A$  and  $B'$  states are, respectively, about  $19,200 \text{ cm}^{-1}$  and  $22,400 \text{ cm}^{-1}$  above the  $X$  state, their contributions, even at the highest temperatures of interest, are small (less than 1%), and higher states can be neglected. The monochromatic absorption of  $\text{MgH}$  is replotted on a larger scale in Fig. 9, together with that for  $\text{CaH}$ , at 1800 K and 10 atmospheres total gas pressure, and as discussed in more detail in §4, its abundance as a function of temperature at 1 atmosphere is plotted alongside the other metal hydrides in Fig. 18.

$\text{CaH}$  - Unlike the other metal hydrides where the opacities can be calculated by reading in data from line lists available from the referenced sources, in the case of  $\text{CaH}$  we demonstrate that individual lines can be calculated from band data. Leininger & Jeung (1995) and Weck et al. (2003b) provide the required data. In the case of the former, band oscillator strengths are provided in their Table V for transitions in the  $A^2\Pi - X^2\Sigma^+$ ,  $B^2\Sigma^+ - X^2\Sigma^+$ , and  $D^2\Sigma^+ - X^2\Sigma^+$  electronic systems for the most abundant  $^{40}\text{CaH}$  isotopic form, giving a total of 154 values of  $v''$  from 0 to 13 and of  $v'$  from 0 to 11, respectively, for each of the three band systems. This is a total of 462 bands strengths, of which somewhat more than a half have non-negligible values. Given a band oscillator strength in the form of  $f_{v',v''}$  for a particular electronic system, a set of rotational lines can be calculated for valid combinations of  $J''$  and  $J'$  that follow the selection rules in order to calculate the strengths from eq. (5) for each available combination of  $v''$  and  $v'$ . The appropriate Hönl-London factors for doublet transitions (Kovács 1969) should be used.

The vibrational component of the vibrational-rotational energy levels can be calculated from the standard anharmonic formulae given by Herzberg (1950), and the rotational components can be calculated from the formulae for doublet states, including spin-orbit splitting when available, from Kovács (1969). The electronic, vibrational and rotational spectroscopic constants, including vibrational and rotation coupling and spin-orbit coupling, can be obtained from Huber and Herzberg (1979). As no information on broadening appears to be available, eq. (15) can be used to calculate the line widths.

Only one other isotopic form of  $\text{CaH}$  is of any significance, namely  $^{44}\text{CaH}$ , with a fractional abundance of 0.02. Exactly the same method can be used to calculate its opacity using eq. (7) with isotopically shifted constants. The partition function of the main isotopic form can be calculated using the spectroscopic constants of the electronic states in eq. (2), and, as previously, since the abundance of the second-most abundant isotope of Ca,  $^{44}\text{Ca}$ , is  $\sim 2\%$ , the isotopic shift correction to the partition function can be neglected. As stated above for  $\text{MgH}$ , the monochromatic absorption of  $\text{CaH}$  is replotted on a large scale in Fig. 9 at 1800 K and 10 atmospheres gas pressure, and its abundance as a function of temperature is shown in Fig. 18, which is discussed in greater detail in §4.

#### 2.4. $H_2S$ and $PH_3$ Infrared Opacities

Though the molecules  $H_2S$  and  $PH_3$  are not very abundant in substellar atmospheres, they are the primary reservoirs of sulfur and phosphorus, respectively, and have distinctive spectral features that can be used to diagnose their chemistry. In this short section, we summarize their spectroscopy and the databases where one can obtain the relevant line lists, and provide a figure at a representative temperature/pressure point depicting their absorption cross sections versus wavelength.

$H_2S$  - The data on line broadening are available from Kissel et al (2002), and HITRAN (Rothman et al. 2003, 2005) and GEISA (Jacquinot-Husson et al. 1999, 2003, 2005) do provide some additional data. The monochromatic opacities are tabulated at  $1 \text{ cm}^{-1}$  intervals from  $200 \text{ cm}^{-1}$  to about  $19570 \text{ cm}^{-1}$ , so essentially all the infrared and a large fraction of the visible light is covered.

$PH_3$  - Like  $H_2S$ , data can now be obtained from HITRAN (Rothman et al. 2003, 2005) and GEISA (Jacquinot-Husson et al. 1999, 2003, 2005). The data used for the precomputed tables are derived from Levy & Lacombe (1993) for  $H$  and  $He$  broadening, and Levy, Lacombe & Tarrago (1994) for the temperature dependence of collision broadening. More recent data are available from Bouanich et al. (2004) for the  $H_2$ -broadening coefficients in the  $\nu_2$  and  $\nu_4$  bands.

The resulting monochromatic opacities are tabulated at  $1 \text{ cm}^{-1}$  intervals from  $200 \text{ cm}^{-1}$ , but unlike  $H_2S$ , reach only to about  $2500 \text{ cm}^{-1}$ , so only fractions of the mid- and far-infrared regions are covered.

The monochromatic absorptions due to  $H_2S$  and  $PH_3$ , along with  $CO$ , as previously discussed, are shown in Fig. 3, at 1600 K and 10 atmospheres, but as mentioned above, due to their low abundances, they are only minor opacity sources. Their abundances are shown in Fig. 17, for a total pressure of 1 atmosphere, together with the other molecules

discussed so far, except for the metal hydrides.

### 2.5. Ultraviolet Opacities

For a substellar object sufficiently close to its parent star where irradiation from that star becomes important, a non-negligible fraction of the incoming radiation will be at short wavelengths, depending on the spectral type of the star. Such radiation can play an important role in the structure of the atmosphere, and ultraviolet and short wavelength visible opacities need to be calculated. The species discussed here are important opacity sources at short wavelengths.

*Fe* - When iron is in the gas phase, an appreciable fraction can be in the monatomic form. Kurucz (1995) gives a database of nearly 800,000 lines from about 100 to 0.055  $\mu\text{m}$ , i.e. respectively, from 100 to nearly 2 million  $\text{cm}^{-1}$  from the far infrared to the far ultraviolet. This covers an unrealistically large range for many practical calculations, and opacities need only be calculated from 10,000  $\text{cm}^{-1}$  to 67,000  $\text{cm}^{-1}$ , i.e. 1  $\mu\text{m}$  to 0.15  $\mu\text{m}$ , respectively. Longer wavelengths in the infrared can be neglected because the opacity due to atomic iron is smaller than that of many of the other species, and shorter wavelength ultraviolet opacities can also be neglected as there is little flux from a parent star with a spectral type later than *F8*. Even with this restricted range, a wider grid spacing may be needed to save memory and processing time. As with the infrared opacities, because *Fe* is a refractory species, no opacities are required below 1000 K.

The data from Kurucz (1995) are in the form of  $\log_{10}$  of the *gf* value for each transition, from which the integrated line strength can be calculated using eq. (1). The Van der Waals, Stark, and natural broadening are also available, which enables the broadening of each line to be calculated using the Van der Waals theory:

$$\Delta\bar{\nu} = \frac{1}{2\pi c} \left[ \gamma_W (N_H + C_{H_2}N_{H_2} + C_{He}N_{He}) \left( \frac{T}{10,000} \right)^{0.3} + \gamma_N \right], \quad (19)$$

where  $\gamma_W$  and  $\gamma_N$  are the Van der Waals and natural broadening coefficients, respectively,<sup>2</sup>  $N_H$ ,  $N_{H_2}$ , and  $N_{He}$  are the number densities of the corresponding species, and  $C_{H_2}$  and  $C_{He}$  are coefficients for  $H_2$  and  $He$ , respectively, because their polarizabilities are different from  $H$ . The partition function can be calculated using eq. (2) by direct summation of the first 31 levels listed by Moore (1949).

Figure 10 shows the monochromatic absorption of *Fe* in the ultraviolet and visible parts of the spectrum due to the sum of the contributions from the lines discussed here and the continuous bound-free absorption discussed in §3.2, at 2200 K and a pressure of 100 atmospheres. A gas pressure of 100 atmospheres is high, and is only chosen so that the lines can be broadened sufficiently to see the general trend. At a realistically lower pressure the general trend may be obscured by the fine details with the opacity changing by many orders of magnitude in very small spectral intervals. The abundances of *Fe*, *Al*, *Ca*, *SiO*, and  $H^-$ , are plotted in Fig. 20 for a total gas pressure of 1 atmosphere, and are discussed in §4.

*CO* - An ultraviolet line list is available from Kurucz (1993), that is quite separate from the infrared data used in §2.1, and includes transitions due the  $A^1\Pi - X^1\Sigma^+$  (4<sup>th</sup> Positive) electronic system. Data on nearly 400,000 lines from 0.430  $\mu\text{m}$  to 0.112  $\mu\text{m}$ , i.e. from about 23,000  $\text{cm}^{-1}$  to about 89,000  $\text{cm}^{-1}$ , are provided. With the *gf* values and other data, the integrated lines strengths from eq. (1) can be calculated. The broadening can be calculated using eq. (19), except that the natural widths are not available from Kurucz (1993).

The monochromatic absorption of *CO* in the ultraviolet, together with those of *SiO*,  $H_2$ ,  $H_2O$ , and  $H_2S$ , is shown in Fig. 11 at 2200 K and total pressure of 10 atmospheres, and is repeated for *CO*, only in greater detail, in Fig. 12. As with *Fe*, the pressure is unrealistically high, but is chosen as a compromise to show the various contributions to the absorption clearly.

*SiO* - Although the most important molecular gas-phase species of silicon is *SiO*, over most of the temperatures of interest most of the silicon has condensed out into refractory silicates, which are the most abundant condensates. Nevertheless, at the upper temperature range of interest *SiO* will be present and can be a significant ultraviolet opacity source, so should be considered. As with the ultraviolet opacity of *CO*, data from Kurucz (1993) are available with 1.7 million lines from 0.43  $\mu\text{m}$  to 0.14  $\mu\text{m}$ , i.e. about 23,000  $\text{cm}^{-1}$  to 70,000  $\text{cm}^{-1}$ , respectively. The transitions are for the  $A^1\Pi - X^1\Sigma^+$  electronic system, which is exactly analogous to the 4<sup>th</sup> Positive system of *CO*.

The partition function can be calculated using eq. (3) with data from Huber & Herzberg (1979). Only the ground electronic state makes any significant contribution for the temperatures of interest. As with *CO*, no information is available to enable isotopic variations to be considered.

Figure 11 shows the absorption of *SiO* compared with several other species in the ultraviolet. Because its abundance is relatively low compared with *CO* or  $H_2$ , a more detailed plot like Fig. 12 for *CO* or Fig. 13 for  $H_2$  (discussed immediately below), is not included. Figure 20 shows the abundance of *SiO* along with some other species (§4).

$H_2$  - This is by far the most abundant molecule, but with no permanent dipole moment, its only contribution in the infrared is collision-induced absorption (as discussed in §3.3). Since the first excited electronic state is at a very high energy above the ground state, there is no absorption at shorter wavelengths until the ultraviolet is reached, where the first and most important bands are due to the  $B^1\Sigma_u^+ - X^1\Sigma_g^+$  (Lyman) and  $C^1\Pi_u - X^1\Sigma_g^+$  (Werner) electronic systems. About 28,500 transitions are available from Kurucz (1993), from which the line strengths can be calculated

<sup>2</sup> Because the abundance of electrons is negligible for most of the temperature range of interest, the Stark coefficient is not relevant for these calculations.

using eq. (1). Since the  $gf$  values given do not include the  $2J'' + 1$  factor, this must be added in the calculations. Also, no information on line broadening is readily available, so eq. (15) has to be used. A set of precomputed tables can be generated for later use.

The partition function can be calculated using eq. (3) and using data from Huber & Herzberg (1979), and as with  $CO$  and  $SiO$ , only the ground electronic state makes any significant contribution for the temperatures of interest. Figure 11 includes  $H_2$ , where it is seen that even per molecule, its strongest absorption exceeds that of the other species shown, and a more detailed opacity is replotted in Fig. 13.

$H_2O$  - In addition to its infrared absorption which is discussed in §2.1, separate data on its ultraviolet opacity can be obtained from Kurucz (1993), which corresponds to bands associated with transitions from the ground electronic state to an excited electronic state. The data contain only a listing of the monochromatic absorption at a set of tabulated points from  $0.188 \mu\text{m}$  to  $0.12 \mu\text{m}$ , corresponding to a range of  $53,000 \text{ cm}^{-1}$  to  $83,000 \text{ cm}^{-1}$ , respectively, with no information on the lines producing this absorption. Except for the stimulated emission factor, no temperature or pressure dependence can be calculated, and the opacity at required frequency points would simply be calculated by linear interpolation from the data provided. As explained in the caption to Fig. 11, no data for individual lines are available, and only a smooth opacity could be plotted in that figure.

$H_2S$  - We consider  $H_2S$  to be a significant ultraviolet opacity source, but the availability of data are even more limited than for  $H_2O$ . Monochromatic opacities can be obtained from Lee, Wang, & Suto (1987) for the range  $0.24 \mu\text{m}$  to  $0.059 \mu\text{m}$ , i.e.  $42,000 \text{ cm}^{-1}$  to  $204,000 \text{ cm}^{-1}$ , respectively, (extending well beyond the normal range of interest), in the form of a short table for wavelengths below  $0.16 \mu\text{m}$ , and a figure for the longer wavelength range.

As with the ultraviolet opacity of  $H_2O$ , it is not possible to consider temperature and pressure dependencies, other than stimulated emission, and the opacity at the required frequencies can only be calculated by linear interpolation when required. Like  $H_2O$ , only smooth data could be plotted in Fig. 11.

$H$  - At the upper temperatures of interest molecular hydrogen will become sufficiently dissociated that atomic hydrogen will be present, which absorbs strongly in the ultraviolet in the Lyman continuum and lines. There will be much weaker absorption in the Balmer, Paschen, Brackett, etc. continua and lines, depending on the temperature, which generally will have little importance. However, because these are easy and quick to calculate, the general line transitions of atomic hydrogen are discussed here, and continuous processes in §3.2.

Given the lower ( $n_i$ ) and upper ( $n_j$ ) principle quantum numbers, though all the line strengths are available in tabulated form (Weise, Smith, & Glennon 1966) for modern computations, the method of Carson (1988a) can be used to gain insight into the associated spectroscopy and for obtaining the line strengths analytically when  $n_i \leq 7$  and  $n_j > n_i$ . The intrinsic line strengths are obtained by solutions of hypergeometric functions listed in that paper for this range of quantum numbers in terms of the square of the Bohr radius for a general hydrogenic atom. Since some very large intermediate numbers are often involved in the calculations, care has to be taken to avoid machine overflow or underflow. The line strengths have to be converted to the required strengths in  $\text{cm}^2\text{atom}^{-1}$  with stimulated emission included using

$$S = \frac{8\pi^3}{3h} a_o^2 e^2 \bar{\nu} S_{ij} \frac{e^{-hcF_i/kT}}{Q(T)} \left[ 1 - e^{-hc\bar{\nu}/kT} \right], \quad (20)$$

where  $a_o$  is the Bohr radius,  $S_{ij}$  is the line strength in units of  $a_o^2$  and  $F_i$  is the term value in  $\text{cm}^{-1}$  of the lower state given by  $RZ^2(1 - \frac{1}{n_i^2})$ , where  $R$  is the Rydberg constant and  $Z$  is the nuclear charge, which is unity here. The term value for the upper state,  $F_j$ , is likewise given by  $RZ^2(1 - \frac{1}{n_j^2})$ , and the line frequency in  $\text{cm}^{-1}$  is just the difference.

Because the  $l$  dependence of the energy levels of hydrogen is so weak, it is sufficient to ignore the corresponding splittings, and the statistical weight of  $n_i$  is already included in  $S_{ij}$  in eq. (20). For the range of temperatures and pressures of interest, only the ground state contributes significantly to the partition function, so  $Q(T) = 2$  for all  $T$ .

For values of  $n_i > 7$  for which  $n_j - n_i \leq 6$ , an approximate method based on Menzel (1969) can be used, which is modified to obtain the strength in  $a_o^2$ , then eq. (20) is used to obtain the required line strength in  $\text{cm}^2\text{atom}^{-1}$ . This is given by

$$S_{ij} \simeq \frac{n_i^5 n_j^2}{n_j^2 - n_i^2} A_{\Delta n} \left[ 1 + \frac{3\Delta n}{2n_i} - \frac{B_{\Delta n}}{n_i^2} \right], \quad (21)$$

where  $\Delta n = n_j - n_i$ , and  $A_{\Delta n}$  and  $B_{\Delta n}$  are two sets of six coefficients as given by Menzel.

Finally, for the most general case outside the restrictions above, the method of Bethe & Salpeter (1957) can be applied using

$$S_{ij} \simeq \frac{64}{3^{1/2}\pi} \frac{n_i^5 n_j^5}{[\Delta n(n_i + n_j)]^4}, \quad (22)$$

to obtain the strength in units of  $a_o^2$ .

Once the line positions and strengths have been calculated, the lines have to be broadened. Because the lines of hydrogen are so well known, and they are only a minor opacity source for the temperatures and pressures of interest, they have not been included in any figures here.

### 2.6. Calculation of Alkali Atomic Opacities with Data from VALD

All the lines of the alkali elements *Li*, *Na*, *K*, *Rb*, and *Cs* can be calculated using the data from the Vienna Atomic Line Database (VALD - Piskunov 1994). Because of the relatively small number of lines, the opacities can be calculated when required, rather than precomputed and stored in tables. The abundances as a function of temperature at a total pressure of 1 atmosphere are plotted in Fig. 19 (§4).

Lithium is an important indicator of youth for objects above about  $65 M_J$  where  $M_J$ , is the mass of Jupiter, which is about  $10^{-3} M_\odot$ . Above this mass it is quickly destroyed by nuclear burning. Sodium and potassium are the most and second most abundant alkali elements, respectively, and because of their low ionization potentials, are responsible for most of the free electrons at low temperatures, and thus, ultimately for the negative hydrogen ion bound-free and free-free absorption. In their own rights, their resonance lines are extremely broad and blanket a large region of the visible and near infrared parts of the spectrum (Burrows, Marly, & Sharp 2000). Because they tend to remain in the atmosphere when more refractory species have rained out, and because their resonance lines are in a part of the spectrum which is otherwise relatively transparent, their absorption can play a surprisingly important role, even though their abundances are relatively low. Although rubidium and cesium have low abundances, like sodium and potassium, their resonance lines are in a part of the spectrum that is relatively transparent, are observed in spectra, and so are included as minor species here.

The line strengths can be calculated from eq. (1) using the tabulated *gf* values, excitation energies, and transition energies, together with a factor of  $2J'' + 1$  for the initial state. The energy levels up to about  $20,000 \text{ cm}^{-1}$  and statistical weights can be used to calculate the partition functions.

With the exception of the resonance lines of sodium and potassium, simple Lorentzian profiles can be calculated based on Van der Waals broadening. For a number of transitions, the Van der Waals broadening coefficients are available together with the natural broadening and Stark broadening (for highly ionized and dense atmospheres). Given the Van der Waals broadening coefficient  $\gamma_W$ , the full-width at half-maximum in  $\text{cm}^{-1}$  can be calculated by scaling the broadening due to collisions of a perturbing species relative to collisions with atomic hydrogen using

$$\Delta\bar{\nu} = \frac{\gamma_W}{2\pi c} \left[ \frac{m_H(m + m_p)}{m_p(m + m_H)} \frac{T}{10000} \right]^{\frac{3}{10}} \left[ \frac{\alpha_p}{\alpha_H} \right]^{\frac{2}{5}} N_p, \quad (23)$$

where  $m$  is the mass of the atom undergoing the transition,  $m_H$  is the mass of the hydrogen atom,  $m_p$  is the mass of the perturbing species,  $\alpha_H$  and  $\alpha_p$  are the polarizabilities of hydrogen and the perturbing species, respectively, and  $N_p$  is the number density of the perturbing species *H*, *H*<sub>2</sub>, or *He*. The combined line width is obtained by evaluating eq. (23) for each of the perturbing species, then taking the square root of the sums of the squares of the line widths, weighted by the abundances of the perturbing species.

When the Van der Waals broadening coefficient is not available, it can still be calculated using the angular momentum quantum numbers of the participating states, from the symbols given in VALD, and the theory in Lang (1999) and Dimitrijević & Peach (1990), in order to calculate the  $C_6$  interaction coefficient. From this the line width can be calculated using

$$\Delta\bar{\nu} = 1.664461 \left[ \frac{kT}{N_A} \left( \frac{1}{m} + \frac{1}{m_p} \right) \right]^{\frac{3}{10}} C_6^{2/5} N_p / c, \quad (24)$$

where  $N_A$  is Avogadro's number.

The resonance lines of sodium and potassium are very strong, and at high pressures, absorption continues out into the far wings across much of the visible and near IR parts of the spectrum. Either truncating the lines, as discussed in §2, or extrapolating a Lorentzian profile into the far wings, is unrealistic, so a more appropriate treatment should be used, such as the more detailed theories by Burrows & Volobuyev (2003), Allard et al. (2003), or Zhu, Babb, & Dalgarno (2006). A normal Lorentzian profile with an appropriate truncation is generally used for the other lines of sodium and potassium, which are much weaker, and for which no suitable theory exists. This applies also to all the lines of the other alkali elements, since their abundances are much lower (Lodders 1999).

### 3. CONTINUOUS OPACITIES

Although the major contribution to the total opacity in brown dwarf and giant planet atmospheres is the large number of lines produced by several molecular species, and in some cases also by monatomic species, continuous sources of opacity must also be considered, because otherwise Rosseland mean opacities would be divergent. Because the various continuous opacity sources can be calculated much more rapidly than some of the line sources, the opacities can be calculated on the fly when required, for the particular temperature and pressure, rather than being stored in precomputed tables.

The various continuous processes that can take place are as follows:

1. Thomson scattering by free electrons, which is not considered here due to the fact that the temperature is too low for a significant number of free electrons to be present to make an important contribution. It is trivial to include if required.

2. Rayleigh scattering, which is also not discussed here, because at the temperatures and pressures of interest, the opacity is totally dominated by gas absorption or scattering due to grains. Again, it would be simple to include, and the polarizabilities for the most abundant species would be required.



3. Free-free opacity, i.e. inverse bremsstrahlung, which is due to a free electron moving in the field of a neutral atom or molecule, or a positively charged atomic or molecular ion, and produces absorption across the whole spectrum. By convention, we count the free electron as part of the system, so the charge of the species, neutral or ionized, includes that electron. Therefore,  $H_{ff}^-$  (negative hydrogen ion free-free) refers to an electron moving in the field of a neutral hydrogen atom. At the temperatures of interest there will be few free electrons, and nearly all the free electrons will be produced from the ionization of the alkali elements, so free-free processes are relatively unimportant, except at the highest temperatures of interest. Consequently this is discussed only briefly.

All free-free absorption coefficients are expressed in  $\text{cm}^5 \text{ particle}^{-1} \text{ electron}^{-1}$ , where a particle is an atom, ion, or molecule, and the absorption per unit volume in  $\text{cm}^{-1}$  is obtained by multiplying this by the abundances of both the particle in question and the electrons. The mass absorption coefficient in  $\text{cm}^2 \text{ g}^{-1}$  is obtained by dividing by the mass density.

4. Bound-free opacity, namely the photoionization of an electron from a neutral or positively charged atomic or molecular species, or photodetachment of an electron from a negative ion. Unlike free-free opacities, this absorption is confined to specific regions of the spectrum, and is relatively strong. The processes we consider are  $H_{bf}^-$  (the photodetachment of an electron from a bound  $H^-$  ion), and photoionization of neutral species. Bound-free opacity also includes photodissociation of molecules.

5. Collision-induced opacity due to induced dipole-dipole absorption by collisions between  $H_2$  with itself, and with other species. This can be a large opacity source in the infrared.

6. Mie scattering by grains, which is briefly discussed.

Table 1 lists the gas-phase species which are important sources of absorption, together with the last 8 entries which give the species included in Mie scattering calculations.

### 3.1. Free-Free Absorption

$H_{ff}$  - This absorption is produced by a free electron moving in the field of a proton. The convention used here is to count the net charge of the whole system. A suitable theory is one based on Carson (1988a) in the form of a table giving the monochromatic cross section in units of  $\text{cm}^5 \text{ proton}^{-1} \text{ electron}^{-1}$  as functions of temperature and photon energy.

For the low temperatures of interest here there will be very few free protons, so this source of absorption is of little importance. However, if a hydrogenic approximation is made for ions of other atoms with low ionization potentials, such as the alkali elements, this source of absorption could play a minor role near the upper temperatures of interest.

$H_{ff}^-$  - This absorption is produced by a free electron moving in the field of a neutral hydrogen atom, and is rather more important than the previous process. Nevertheless, it will make only a minor contribution to the total opacity. The absorption can be calculated from fitted coefficients from Wishart (1979).

$He_{ff}^-$  - In the case of free electrons moving in the field of a neutral helium atom, Table 2 of Bell, Berrington, & Croskery (1982) can be used. Pre-scaling the tabulated values of the cross sections by the square of the photon energy and the square root of the temperature reduces the changes in the values in the resultant new table, and increase the accuracy of the interpolation.

$H_{2ff}$  - Because  $H_2$  is the most abundant species, a free electron moving in the field of a neutral  $H_2$  molecule is likely to be the most important negative ion free-free opacity source. The data are available from Table 1 of Bell (1980), and can be treated in the same way as  $He^-$ , with the same pre-scaling used before bicubic spline interpolation is used.

Other Species - If required, the opacity of the following species can be included:  $C_{ff}^-$  (Bell, Hibbert, & Berrington 1988),  $N_{ff}^-$  (Ramsbottom, Bell, & Berrington 1992),  $Cl_{ff}^-$  (John & Morgan 1975),  $Ne_{ff}^-$ ,  $Ar_{ff}^-$ ,  $Kr_{ff}^-$ ,  $Xe_{ff}^-$ ,  $Li_{ff}^-$ ,  $Na_{ff}^-$ ,  $Cs_{ff}^-$ ,  $O_{ff}^-$ ,  $Hg_{ff}^-$ ,  $N_{2ff}^-$ ,  $O_{2ff}^-$ ,  $CO_{ff}^-$ ,  $CO_{2ff}^-$ , and  $H_2O_{ff}^-$  (John 1975). However, because of their low abundances in substellar atmospheres, they are unimportant for this particular work.

### 3.2. Bound-Free Absorption

$H$  - At the upper temperature range of interest, free atomic hydrogen will be present, which will contribute bound-free absorption to the total opacity. If  $\sigma_n(\bar{\nu})$  is the partial cross section as a function of wavenumber for the atom in an initial state with the principle quantum number  $n$ , with  $n=1, 2, 3, \dots$ , then for a general hydrogenic atom

$$\sigma_n(\bar{\nu}) = \frac{64\pi^2}{3^{3/2}} \left( \frac{e^2}{hc} \right)^3 \frac{RZ^4 e^{-RZ^2 \frac{hc}{kT}(1-1/n^2)}}{\bar{\nu} n^3 Q} G(n, Z, \bar{\omega}) \left( 1 - e^{-hc\bar{\nu}/kT} \right), \quad (25)$$

in  $\text{cm}^2 \text{ atom}^{-1}$  for a given  $n$ , where  $Z$  is the nuclear charge, which is 1 for hydrogen,  $R$  is the Rydberg constant,  $Q$  is the partition function,  $\bar{\omega}$  is the wavenumber offset from an absorption threshold,  $G(n, Z, \bar{\omega})$  is the Gaunt factor, and the other quantities have their usual meanings. Equation (25) includes all factors, including the population of the initial level with the quantum number  $n$  and the stimulated emission factor. At a given wavenumber, eq. (25) is evaluated for all values of  $n$  for which

$$\bar{\omega} = \bar{\nu} - \frac{RZ^2}{n^2} \geq 0, \quad (26)$$

is valid, i.e., at and above the absorption threshold for a given value of  $n$ . Below the threshold, no contribution need be calculated. We neglect here the slight effects due to level dissolution and related pseudo-continuum opacities (Hummer & Mihalas 1988). The total cross section at a given value of  $\bar{\nu}$  is obtained by summing the partial cross sections  $\sigma_n(\bar{\nu})$  over  $n$  for each frequency grid point  $\bar{\nu}$ . A value of 20 is a more than suitable value for the upper limit of  $n$ , and should account for all the excited levels present for the temperatures and pressures of interest.

The Gaunt factor  $G(n, Z, \bar{\omega})$  is a correction to the cross section, and is obtained from an algorithm by Carson (1988b). It is exact for the range  $1 \leq n \leq 7$ , and approximations are used for larger values of  $n$ . The strongest absorption is the Lyman continuum arising from the ground electronic state in the ultraviolet, which is always present. Absorption at longer wavelengths is due to excited electronic states, which are only important when these states are sufficiently populated at high enough temperatures.

Although the partition function should be calculated by summing the levels, in practice for the temperatures and pressures of interest in cool atmospheres, only the ground state contributes significantly, and so it has the value of 2.

The monochromatic bound-free absorption per atom (or ion in the case of  $H^-$ ) is shown in Fig. 14 for  $H$ ,  $H^-$ ,  $Na$ ,  $K$ , and  $Fe$  for a temperature of 2500 K. Because of the relatively low temperature, the absorption due to the Balmer continuum is too weak to show, and is an unimportant opacity source for most of the temperatures of interest; however, the Lyman continuum is very important if there is a considerable amount of irradiation at short ultraviolet wavelengths due to the parent star.

$H^-$  - At high enough temperatures for some of the  $H_2$  to be dissociated, some of the alkali elements will be ionized, and a portion of the freed electrons can be attached to the free hydrogen atoms, resulting in the  $H^-$  ion. For photons with wavenumbers above  $6083 \text{ cm}^{-1}$  (wavelengths shorter than  $1.64 \mu\text{m}$ ) in the infrared this extra electron can be photodetached.

Data from from Bell & Berrington (1987), Mathisen (1984), and Wishart (1979) are available. The data are in the form of a table of 85 cross sections with corresponding wavenumbers from the absorption threshold to about  $556,000 \text{ cm}^{-1}$  ( $0.018 \mu\text{m}$ ) in the ultraviolet, from which the absorption at the required wavenumbers can be obtained by linear interpolation. As the data extend well beyond the short wavelengths of interest in the ultraviolet, no extrapolation is required. After a rapid rise above the absorption threshold in the near infrared, there is very broad absorption extending from the near infrared, across the entire visible, and into the ultraviolet, gradually falling at shorter wavelengths, except for a strong and very sharp peak in the ultraviolet. This peak corresponds to a resonance with the  $^2P$  state, and is in fact where  $H^-$  has its maximum absorption.

As can be seen in Fig. 14,  $H^-$  is the strongest opacity source per species here, except for wavelengths shorter than  $0.16 \mu\text{m}$  where  $Fe$  exceeds it most of the time. As can also be seen from Fig. 20, the abundance of  $H^-$  smoothly decreases with decreasing temperature.

$Na$  - Data are available from the Strasbourg TOPBASE database (Cunto & Mendoza 1992; Cunto et al. 1993) for many ions and neutral atoms of astrophysical interest up to calcium in the periodic table and for iron. In the case of neutral sodium, the excitation energies and statistical weights of the ground state and 31 excited states are listed in the reference, together with partial cross sections as a function of photon energy in the form of a table for each state. The total cross section  $\sigma(\bar{\nu})$  as a function of wavenumber can be obtained from the summation, with stimulated emission included:

$$\sigma(\bar{\nu}) = \sum_{i=1} g_i \sigma_i(\bar{\nu}) \frac{e^{-E_i hc/kT}}{Q(T)} \left(1 - e^{-hc\bar{\nu}/kT}\right), \quad (27)$$

in  $\text{cm}^2 \text{atom}^{-1}$ , where  $i$  is now just a running index rather than a quantum number, as in eq. (25), with the ground state being indexed by  $i=1$ ,  $g_i$ ,  $E_i$ , and  $\sigma_i(\bar{\nu})$  are, respectively, the statistical weight, excitation energy in  $\text{cm}^{-1}$  above the ground state, and the partial cross section as a function of wavenumber for the  $i^{\text{th}}$  state.

Simple linear interpolation can be used to obtain  $\sigma_i(\bar{\nu})$  at the required value of  $\bar{\nu}$ . Summation is skipped over those indices for which the photon energy is below the absorption threshold, and for a photon energy above the upper range of the tabulated values the cross section of the last tabulated cross section can be used. This very simple extrapolation avoids an artificially discontinuous drop in opacity.

The partition function can be obtained by summing the ground state and the first two excited states which have energies less than  $20,000 \text{ cm}^{-1}$  above the ground state, using data from Moore (1949). The Boltzmann factors for states with energies at and above  $20,000 \text{ cm}^{-1}$  over the ground state make a negligibly small contribution to the partition function, much less than 1 percent, even at the temperatures well above the highest of interest. Consequently, such states are not considered, as previously stated. Because of its low ionization and excitation energies,  $Na$  has important bound-free absorption at relatively long wavelengths, even at a temperature of 2500 K, as plotted in Fig. 14. The sodium abundances, along with those of the other alkali elements, are plotted in Fig. 19 (see also Lodders 1999).

$K$  - Unfortunately, potassium is one of the elements not available in the TOPBASE database, but an alternative though considerably less extensive database given by Verner & Yakovlev (1995) can be used that does include it. They cover, with fitted coefficients, all the neutral atoms from hydrogen to zinc ( $Z = 30$ ), together with most of their positive ions that contain at least one bound electron.

However, the only data of relevance for potassium are the fit coefficients for absorption from the outermost electron in the  $[Ar].4s^1$  ground state configuration. Unlike sodium, no data are available for excited states. Verner & Yakovlev (1995) also give cross sections for inner electrons, but these are at wavelengths in the far ultraviolet and X-ray that are of little interest here.

From Verner & Yakovlev (1995), the general expression for the partial cross section is given by

$$\sigma_{nl}(\bar{\nu}) = 10^{-18} \sigma_o \left\{ [(y-1)^2 + y_w^2] y^{(P-10)/2-l} \left[ 1 + \sqrt{y/y_a} \right]^{-P} \right\}, \quad (28)$$

in  $\text{cm}^2 \text{absorber}^{-1}$ , where  $n$  is the principle quantum number,  $l$  is the angular momentum quantum number taking the values 0, 1, 2, ... for  $s, p, d$ , etc.,  $\sigma_o, y_w, y_a$ , and  $P$  are fit parameters, and  $y$  is the photon energy relative to another fit parameter  $E_o$ . Since we are expressing photon energies in units of  $\text{cm}^{-1}$ , but  $E_o$  is given in eV in the reference,  $y = \bar{\nu}/s_o E_o$ , where the conversion factor  $s_o = 8065.539 \text{ cm}^{-1} \text{eV}^{-1}$  has to be applied. Equation (28) can be applied only for photon energies at and above the absorption threshold energy. Otherwise, there is no contribution.

In the case of potassium, only one partial cross section is available, and since the absorption threshold energy is the ionization energy, eq. (28) is evaluated only at and above the ionization energy with  $n=4$  and  $l=0$ . Since the statistical weight is already included in the cross section, and only the ground state is considered, eq. (28) need only be divided by the partition function and multiplied by the stimulated emission factor to obtain the total required absorption in  $\text{cm}^2 \text{atom}^{-1}$ . As with sodium, the first three energy levels from Moore (1949) are used to calculate the partition function. Because we have data only on a single level, the absorption plotted in Fig. 14 contains only one absorption edge. As discussed in §4, the abundances are plotted in Fig. 19.

*Fe* - Like potassium, the TOPBASE database from Cunto & Mendoza (1992) and Cunto et al. (1993), does not include bound-free data for iron, which has to be included, as it can be very important. Such data, however, are available in Bautista (1997). From Kurucz (1995), data are available for the bound-free absorption for 30 levels, starting from the ground state. The data are in the form of an energy in Hz above the ground state, together with various parameters, from which the total absorption in  $\text{cm}^2 \text{atom}^{-1}$  can be found from summing over the partial cross sections using

$$\sigma(\bar{\nu}) = 10^{-18} \sum_{i=1} g_i \alpha_i \sigma_i^x [\beta_i + x(1 - \beta_i)] \frac{e^{-E_i hc/kT}}{Q(T)} \left( 1 - e^{-hc\bar{\nu}/kT} \right), \quad (29)$$

with stimulated emission included, where  $\sigma_i$  is the partial cross section at the threshold for the  $i^{\text{th}}$  level,  $\alpha_i$  and  $\beta_i$  are fitted coefficients for that level,  $g_i$  is the statistical weight, and  $F_i$  is the corresponding term value in  $\text{cm}^{-1}$  above the ground state for that level, which we convert from the tabulated value in Hz.  $F_i$  is also the photon energy of the absorption threshold, and is used to define the dimensionless wavelength  $x = F_i/\bar{\nu}$  used in eq. (29).

As before, summation is required only for those levels for which  $\bar{\nu} \geq F_i$ , and the partition function is obtained by summing over the levels listed in Moore (1949). Summing over the first 30 levels up to just above  $20,000 \text{ cm}^{-1}$  from the ground state should be adequate. Previously, in Fig. 10, the combined bound-bound and bound-free absorption were plotted. Because *Fe* is so important, it is also included in Fig. 14 for bound-free absorption alone. (See Fig. 20 for its abundance as a function of temperature.)

*CH* - Bound-free data are available for the *CH* molecule from Kurucz, Dishoeck, & Tarafdar (1987) in the form of a table of cross sections for the range of temperatures and photon energies of interest. Bicubic splines can be used for interpolation, and the partition function is not required, as it is implied in the table. However, for a solar composition with  $[C]/[O] < 1$ , this species is of little importance at any temperature.

*OH* - Bound-free data are available from Kurucz, Dishoeck, & Tarafdar (1987) for the *OH* molecule in a form very similar to *CH*, and the same interpolation scheme can be used. For a solar composition at sufficiently high temperatures when  $H_2O$  has mostly dissociated, this molecule can play a minor role, but at the temperatures of interest here where  $H_2O$  is mostly associated, it is unlikely to be important. Neither *CH* nor *OH* are shown in our plots.

### 3.3. Collision-Induced Absorption

The last major gas-phase contribution to the opacity that is of interest in cool atmospheres is collision-induced absorption (CIA). During a collision a molecule can have a transient induced dipole moment, which can allow a rotational or vibrational-rotational transition to take place in the infrared, that would otherwise not be possible. Symmetric diatomic molecules that have no permanent dipole moment, as well as symmetric polyatomic molecules that have a number of vibrational modes that are inactive in the infrared are of particular interest. Because the absorption is due to the collision of gas-phase species, it will scale as the square of the gas pressure, and so is most important for high pressures and low temperatures relevant to giant planets and brown dwarfs.

In a gas with a typical astrophysical composition, by far the most important sources of CIA are due to  $H_2 - H_2$  and  $H_2 - He$  collisions, together with collisions between  $H_2$  and other common gas-phase species. In the absence of CIA (and discounting small Rayleigh scattering), these two most abundant gases are very transparent in the infrared, with  $H_2$  having only very weak quadrupole absorption, and *He* having essentially no absorption at all. Thus, the treatment of CIA is particularly important.

CIA cross sections can be found mostly in Borysow & Frommhold (1989), Borysow & Frommhold (1990), Borysow, Frommhold, & Moraldi (1989), Zheng & Borysow (1995), Zheng & Borysow (1995b), Borysow & Frommhold (1988), and Borysow, Frommhold, & Birnbaum (1985), as detailed below, for  $H_2 - H_2$ ,  $H_2 - He$  and  $H_2 - CH_4$  collisions, the last involving collisions with a third common species. Data on  $H_2 - H_2O$  and other collision pairs of relevance are not readily available.

The data for  $H_2 - H_2$ ,  $H_2 - He$ , and  $H_2 - CH_4$  are similar, consisting of cross sections in  $\log_{10}(\text{cm}^{-1}\text{amagat}^{-2})$  per collision pair tabulated in wavenumbers from  $10 \text{ cm}^{-1}$  in the far infrared to  $18,000 \text{ cm}^{-1}$  in the visible, for 500 values, and for temperatures ranging from 50 K to 5000 K, for 25 values, where an amagat is a unit of density in terms of Loschmidt's number,  $L_o$ . ( $L_o = 2.68676 \times 10^{19} \text{ cm}^{-3}$  is defined such that  $L_o = N_A/V_o$ , where  $N_A$  and  $V_o$  are, respectively, Avogadro's number and the volume occupied by 1 mole of gas at standard temperature and pressure.)

At a given temperature and wavenumber, the monochromatic absorption for a collision pair in  $\text{cm}^{-1}\text{amagat}^{-2}$  can be obtained by bilinear interpolation in wavenumber and temperature, and linear interpolation in the tabulated log of the absorption, yielding a value of  $\sigma_{H_2-X}(\bar{\nu})$ , where  $X$  is the second species colliding with the  $H_2$  molecule, and can be another  $H_2$  molecule or another species. The required monochromatic volume opacity  $\kappa_v(\bar{\nu})$  in  $\text{cm}^2\text{cm}^{-3}$ , i.e. in  $\text{cm}^{-1}$ , can then be obtained from

$$\kappa_v(\bar{\nu}) = \sigma_{H_2-X}(\bar{\nu})N_{H_2}N_X/L_o^2, \quad (30)$$

where  $N_{H_2}$  and  $N_X$  are, respectively, the number densities in  $\text{cm}^{-3}$  of  $H_2$  and the species colliding with it. Equation (30) can be evaluated for each of the three collisions, with the results summed and added to the total opacity, after correction for stimulated emission. At the end of all the calculations, the final monochromatic mass opacity in  $\text{cm}^2\text{g}^{-1}$  is obtained by dividing by the gas mass density.

Data are available from the following references:

$H_2 - H_2$  - Borysow et al. (1985), Zheng, & Borysow (1995a) and (1995b), Borysow & Frommhold (1990), Lenzuni, Chernoff, & Salpeter (1991), and Guillot et al. (1992),

$H_2 - He$  - Borysow, Frommhold, & Birnbaum (1988), Borysow, Frommhold, & Moraldi (1989), and Borysow & Frommhold (1989), and

$H_2 - CH_4$  - Courtin (2004).

Figure 15 shows the monochromatic absorption due to  $H_2 - H_2$ ,  $H_2 - He$ ,  $H_2 - CH_4$ , and the combined CIA, i.e. the sum of the contributions due to  $H_2$  colliding with another  $H_2$ ,  $He$ , and  $CH_4$  weighted by their respective abundances at 200 and 1000 K at a pressure of 10 atmospheres. The absorption is expressed in  $\text{cm}^2$  per  $H_2$  molecule, regardless of the fraction of  $H_2$  molecules participating in a collision at any given instant. As CIA is proportional to the square of the pressure, plots at 1 and 100 atmospheres would be exactly the same, except that the absorption would be scaled by factors of 0.01 or 100, respectively.

### 3.4. Calculation of Grain Opacities

The final source of opacities discussed here is due to scattering and absorption caused by solid and liquid particles, for which the treatment is completely different than the gas phase. This obviously requires liquid or solid particles to be suspended in the atmosphere in the form of clouds, which for equilibrium chemistry requires the temperature to be below the condensation temperature of the species considered. This can take place in the atmospheres of very late M dwarfs, and all T and L dwarfs.

In the limiting case when particles are very small compared with the wavelength of the radiation, Rayleigh scattering takes place; in the opposite case when the particles are very large compared with wavelength, geometric scattering is applicable. In the most general (and most complicated) case when the wavelength of the radiation is of approximately the same order as the particle size, Mie scattering theory should be applied.

The theory we present here is based on the work of Van de Hulst (1957), where we start with a set of uniform spheres of the same substance in suspension (liquid or solid), all having the same radius. The scattering and absorption of the radiation depends on only four parameters: the real and imaginary parts of the refractive index, the radius of the particles, and the wavelength of the photon being scattered or absorbed.

Specifically, the scattering and extinction coefficients are

$$Q_{sca} = \frac{\sigma_{scat}}{\pi a^2} = \frac{2}{x^2} \sum_{n=1}^{\infty} (2n+1) [|a_n|^2 + |b_n|^2], \quad (31)$$

and

$$Q_{ext} = \frac{\sigma_{ext}}{\pi a^2} = \frac{2}{x^2} \sum_{n=1}^{\infty} (2n+1) \text{Re}(a_n + b_n), \quad (32)$$

respectively, where  $a$  is the particle radius,  $x$  is the size parameter ( $= 2\pi a/\lambda$ ), and  $a_n$  and  $b_n$  are the Mie coefficients. Following Deirmendjian (1969), for numerical computation these coefficients can be expressed in terms of the complex index of refraction,  $m = n_{real} - in_{imag}$ , and Bessel functions of fractional order:

$$a_n = \frac{\left[ \frac{A_n(mx)}{m} + \frac{n}{x} \right] J_{n+\frac{1}{2}}(x) - J_{n-\frac{1}{2}}(x)}{\left[ \frac{A_n(mx)}{m} + \frac{n}{x} \right] \left[ J_{n+\frac{1}{2}}(x) + (-1)^n i J_{-n-\frac{1}{2}}(x) \right] - J_{n-\frac{1}{2}}(x) + (-1)^n i J_{-n+\frac{1}{2}}(x)}, \quad (33)$$

and

$$b_n = \frac{[mA_n(mx) + \frac{n}{x}]J_{n+\frac{1}{2}}(x) - J_{n-\frac{1}{2}}(x)}{[mA_n(mx) + \frac{n}{x}] \left[ J_{n+\frac{1}{2}}(x) + (-1)^n J_{-n-\frac{1}{2}}(x) \right] - J_{n-\frac{1}{2}}(x) + (-1)^n J_{-n+\frac{1}{2}}(x)}, \quad (34)$$

where

$$A_n(mx) = \frac{J_{n-\frac{1}{2}}(mx)}{J_{n+\frac{1}{2}}(mx)} - \frac{n}{mx}. \quad (35)$$

Equations (31) and (32) are evaluated by summing up the first 50 to 200 terms, depending on the value of the size parameter, with large size parameters requiring more terms in order to produce accurate scattering and extinction coefficients. For size parameters larger than  $\sim 75$ , variations in  $Q_{ext}$  and  $Q_{sca}$  are much reduced. An asymptotic form of the Mie equations for large  $x$  outlined fully by Irvine (1964) is used to find the limits of the scattering coefficients. In the large  $x$  limit, the extinction coefficient,  $Q_{ext}$ , approaches 2.0. Interpolation between the full Mie theory results and these asymptotic limits yields the coefficients for large size parameters.

In practice, there will be a range of particle sizes for the grains or drops suspended in a cloud. Sudarsky (2002) assumed a range of particle sizes given by

$$n(a) \propto \left(\frac{a}{a_0}\right)^6 \exp\left[-6\left(\frac{a}{a_0}\right)\right], \quad (36)$$

where  $n(a)$  is proportional to the number of particles in the size range  $a$  to  $a + da$  and  $a_0$  is the size at the peak of the distribution. Equation (36) reproduces the distributions in cumulus water clouds in Earth's atmosphere fairly well if  $a_0 \simeq 4 \mu\text{m}$  (Deirmendjian 1964). However, stratospheric aerosols in Earth's stratosphere can be represented by the "haze" distribution given by

$$n(a) \propto \frac{a}{a_0} \exp\left[-2\left(\frac{a}{a_0}\right)^{1/2}\right], \quad (37)$$

which is also obtained from Deirmendjian (1964).

Given a size distribution, eqs. (31) and (32) are evaluated for a range of sizes for every wavelength in a grid, and weighted mean scattering and extinctions are calculated at each wavelength for a particular condensed species, using the refractive index of that species at each wavelength in turn. In general, the real and imaginary parts of the refractive index vary with wavelength; in particular, the imaginary part can vary by many orders of magnitude. These calculations are repeated for any additional species present in the cloud, using the refractive indices for that species. Thus, in a parcel of gas inside a cloud, the total opacity is given by the contribution of the condensates, in addition to that of the gas-phase species previously discussed.

Figure 16 compares the monochromatic absorption of the gas at 500 K and 1500 K at a pressure of 1 atmosphere, and the absorption due to  $MgSiO_3$  grains and water ice for two grain (or ice) sizes. The gas opacity is calculated from the contributions due to many of the individual species that have been previously discussed.

### 3.5. Abundance-Weighted Total Opacities

In order to calculate the total opacity of a gas, or a gas plus condensed species, the monochromatic opacity as a function of wavelength or wavenumber for each species has to be calculated first in the form of an absorption in  $\text{cm}^2$  per atom, ion, or molecule, for the required temperature and pressure. Once the absorption for each species has been obtained, they are combined together. This requires calculating the abundance of each species, then weighing their contribution by these abundances.

Because all intermediate calculations are based on number densities of the species, it is convenient to perform all opacity calculations as volume opacities, i.e. in  $\text{cm}^2\text{cm}^{-3} = \text{cm}^{-1}$ , which are obtained by multiplying the opacities of each species by their number densities in  $\text{cm}^{-3}$ , then at the end to convert to the total mass opacity by dividing by the mass density. This can be summarized by writing

$$\kappa_{mass} = \frac{1}{\rho} \sum_i N_i \kappa_i = \frac{N_A}{\mu N_t} \sum_i N_i \kappa_i, \quad (38)$$

where  $\kappa_{mass}$  is the monochromatic mass opacity in  $\text{cm}^2\text{g}^{-1}$ ,  $N_i$  and  $\kappa_i$  are, respectively, the number density in  $\text{cm}^{-3}$  of species  $i$  and the monochromatic opacity of that species in  $\text{cm}^2\text{species}^{-1}$ ,  $\rho$  is the density (possibly including suspended condensates) in  $\text{g cm}^{-3}$ ,  $N_A$  is Avogadro's number,  $\mu$  is the mean molecular weight, and  $N_t$  is the total number density in  $\text{cm}^{-3}$  of all particles, gas and condensates.

In order to calculate the total opacity, the quantities  $N_i$  in eq. (38), the number densities for each species, have to be calculated. This is discussed in §4. However, one of the dilemmas in calculating total opacities is that *ab initio* it is not always possible to know which species are likely to be important opacity sources without investing the time in the first place to determine whether they are indeed abundant enough. In many cases, this is obvious, but in others this

can only be determined after it has been included in chemical equilibrium calculations. However, even then, a species with a low abundance can turn out to be a very important opacity source. This can take place when its absorption features fall in a part of the spectrum that is otherwise quite transparent for the particular temperature and pressure being investigated. Good examples are *TiO* in M dwarfs, and the lines of the alkali elements in T and L dwarfs. Moreover, even species that do not contribute a significant opacity, or for which no relevant data are available, can indirectly affect the opacity by altering the abundances of those species that do.

#### 4. ATMOSPHERIC ABUNDANCES

Before any opacities can be calculated, the abundances of a mixture of a large number of species have to be determined for the given temperature and pressure. For the results shown here, nearly 500 species were followed, including over 150 condensates, containing 27 elements, using the Allende Prieto, Lambert, & Asplund (2001), Asplund et al. (2005), Allende Prieto & Lambert (2005) composition, which replaces the Anders & Grevesse (1989) composition previously used. The 27 elements used are the following: *H, He, Li, C, N, O, F, Ne, Na, Mg, Al, Si, P, S, Cl, Ar, K, Ca, Ti, V, Cr, Mn, Fe, Co, Ni, Rb, and Cs*. Other than *He*, which should be included for collision-induced opacities, the noble gases neon and argon play no role in the chemistry or opacity, but should still be included to ensure that for a given pressure, the gas has the correct density. In spite of their very low abundances, rubidium and caesium should be included because they have strong resonance lines that can be relatively important in the near infrared, and together with the other alkali elements contribute free electrons at relatively low temperatures because of their low ionization energies. Lithium should also be included because below a mass of about 65  $M_J$  it is not destroyed by nuclear burning, and it is present in more massive brown dwarfs and stars that are too young to have destroyed their lithium.

When calculations are performed with different values of metallicity ( $Z$ ), the abundances of all the metals should be scaled with  $Z$ , but their fractions within  $Z$  remained constant. At temperatures high enough for ions and electrons to be important, electrons should be added as an additional “element” with a zero total abundance, and the stoichiometric coefficient of an ionized atom, including the electron itself, is equal in magnitude, but opposite in sign, to the charge.

In all cases the abundances can be calculated assuming chemical equilibrium between the different species in the gas phase, together with any condensates that may be present, using the methods described in detail in Sharp & Huebner (1990), Burrows & Sharp (1999), and Fegley & Lodders (2001). For a given temperature, pressure, and composition, the equilibrium abundances of the various species can be determined by minimizing the total Gibbs free energy of the system. This requires a knowledge of the free energy of each species as a function of temperature, which is normally obtained from thermodynamic data. However, suitable spectroscopic data for an important gas-phase species can be used to calculate the free energy when no thermodynamic data are available, as summarized in Appendix A of Burrows et al. (2005). Since the work of Sharp & Huebner (1990), a number of substantial improvements to the databases have been made, and were used in Burrows & Sharp (1999). Extensive updates to these thermodynamic databases have been made by Lodders & Fegley (2002). Data from Barin (1995) for a number of species replace the earlier data from the JANAF tables from Chase (1982) and Chase et al. (1985). In the earlier work, Burrows & Sharp (1999) used Tsuji (1973) and Turkdogan (1980) for most of the species for which data in the JANAF tables were not available, and most of these data are now replaced by the far better data from Barin (1995). The most important gas-phase species from Barin (1995) are: *CaH, CrO, TiO, and VO*, and the most important condensates are: *Al<sub>2</sub>O<sub>3</sub>, CaTiO<sub>3</sub>, FeSiO<sub>3</sub>, MgTiO<sub>3</sub>, Mg<sub>2</sub>TiO<sub>4</sub>, MgTi<sub>2</sub>O<sub>5</sub>*, various oxides and nitrides of chromium, titanium, and vanadium, and a number of other compounds involving combinations of at least two elements out of aluminum, calcium, magnesium, manganese, and silicon, combined with oxygen.

Most thermodynamic tabulations of free energy of a species are given in terms of the formation energy of the species from their elements in their reference states at the temperature being considered. The problem with this is that there is a discontinuity in the derivative of the free energy when one of the elements in its reference state changes phase. One way to circumvent this problem is to redefine the free energy of formation of a species in terms of its constituent elements in their monatomic neutral gaseous phase, even if that phase is not stable at the temperature being considered. Thus, the element in that state is defined as having a free energy of zero. Moreover, if charged species are considered so electrons are included, free electrons should also be defined to have a zero free energy of formation. Using this method, polynomials can be fitted to the free energy to represent a smooth function with temperature.

Our equilibrium code was originally based on the SOLGASMIX code from Besmann (1977), which used calories as the measurement of heat and 1 atmosphere as the reference pressure (as used also by the JANAF tables). The free energies of formation of a species from its elements in their standard reference state are used, then these are converted to the free energy of formation from the elements in their neutral monatomic gaseous state using

$$\Delta G_{pi} = \Delta G_{pi}^o - \sum_{j=1}^n \nu_{pij} \Delta G_{1j}^o, \quad (39)$$

where  $\Delta G_{pi}$  is the required Gibbs free energy of formation of substance  $i$  in phase  $p$  in  $\text{cal mol}^{-1}$ ,  $\Delta G_{pi}^o$  is the tabulated free energy in terms of the elements in their standard reference states,  $\nu_{pij}$  is the stoichiometric coefficient of species  $i$  in terms of each of its constituent elements  $j$ , and  $\Delta G_{1j}^o$  is the tabulated free energy of formation from its reference state of element  $j$  in its monatomic gaseous phase, where the gas phase is always indexed by 1. If the reference state of the element is the monatomic gaseous phase, then this term is zero. The summation is performed over the  $n$  different elements contained in the species, which include electrons for charged species as an additional “element.”

The data from Barin (1995) are expressed in terms of Joules, with the reference pressure being 1 bar. Moreover, it is convenient to use the Gibbs energy functions as tabulated, then convert these to the free energies in cal mole<sup>-1</sup>. Given  $g'_{pi}$ , the Gibbs energy function in J mol<sup>-1</sup> of species  $i$  in phase  $p$  with a reference pressure of 1 bar, the required Gibbs energy function,  $g_{pi}$  in cal mol<sup>-1</sup> with a reference pressure of 1 atmosphere, can be obtained from

$$g_{pi} = [g'_{pi} - P_c]/J_c, \quad (40)$$

where for a gas-phase species,  $P_c$  is the conversion factor in cal mol<sup>-1</sup>, given by  $P_c = R \ln(1.01325)$ , with  $R = 1.986$  being the gas constant in cal mol<sup>-1</sup>, and  $J_c = 4.184$  J cal<sup>-1</sup>. For a condensed phase, since the typical bulk modulus is in the megabar range, the compressibility of the species is neglected, so  $P_c$  is replaced by zero. The free energy is then obtained from

$$\Delta G_{pi} = \Delta H_{pi}(298) - Tg_{pi} + \sum_{j=1}^n [\nu_{ij} \{Tg_{1j} - \Delta H_{1j}(298)\}], \quad (41)$$

where  $\Delta H_{pi}(298)$  is the enthalpy of formation of species  $i$  in phase  $p$  from its elements in their standard reference states at 298.15 K, and as with eq. (39), the summation is over the constituent elements, with the indices referring to element  $j$  in phase 1, the gas phase. In the case of data used from Barin (1995), the value of  $\Delta H_{pi}(298)$  is often given only for the phase that is stable at 298.15 K. However, for phases stable at elevated temperatures, the enthalpy change is given at each phase boundary with increasing temperature, so the value of  $\Delta H_{pi}(298)$  for a high temperature phase could be obtained by taking the enthalpy of formation of the phase stable at 298.15 K, and adding to it the enthalpy change for the high temperature phase, summing over any intermediate phases.

For a number of phases at intermediate temperatures that have too few points to fit a smooth function using the data from Barin (1995), the relationship between the Gibbs energy function, enthalpy, entropy and specific heat could be used. Dropping for convenience the indices  $p$  and  $i$  and the primes because heat is measured in Joules, but making it clear that it is a function of  $T$ , the Gibbs energy function can be obtained from

$$g(T) = \frac{H(298) - H(T_o)}{T} + S - \frac{1}{T} \int_{T_o}^T C_p dT + \int_{T_o}^T \frac{C_p}{T} dT, \quad (42)$$

where  $H(298)$  is the enthalpy at 298.15 K,  $H(T_o)$  is the enthalpy at some tabulated temperature  $T_o$  in the range where the phase is stable,  $S$  is the corresponding entropy at  $T_o$ , and  $C_p$  is the specific heat at constant pressure. All these quantities are given in Barin (1995). If  $C_p$  is constant over the temperature range being considered, which is the case for all liquid phases tabulated, then eq. (42) can be integrated to give

$$g(T) = \frac{H(298) - H(T_o)}{T} + S + C_p [T_o/T - \ln(T_o/T) - 1]. \quad (43)$$

Using eq. (43), together with eqs. (40) and (41), it is possible to generate additional points, including those outside the range of stability of the phase being studied, and make a good fit. If extrapolation outside the range of stability is included for the purposes of making a fit, such as below the freezing point of a liquid phase, one should ensure that the free energy outside the range of stability is always greater than the phase that is stable in that region, in order to guarantee that the phase being extrapolated never forms in preference to the more stable phase. If the specific heat varies with temperature, it should be possible to replace  $C_p$  by a fitted polynomial and to integrate eq. (42).

In addition to the above methods, for some gas-phase species, such as  $TiH$ , no suitable thermodynamic data appear to be available, but it is possible to use the spectroscopic data for this purpose. The free energy can be calculated from the data using eq. (A1) in Burrows et al. (2005), and is directly in the form required.

At the temperatures for which data are tabulated using the various methods already discussed, least-square fits can be made for a set of polynomials whose highest order is given by

$$\Delta G_{pi}(T) = aT^{-1} + b + cT + dT^2 + eT^3, \quad (44)$$

where  $a$ ,  $b$ ,  $c$ ,  $d$ , and  $e$  are fitted coefficients, and  $\Delta G_{pi}(T)$  is the fitted Gibbs free energy of formation at temperature  $T$  of species  $i$  in phase  $p$ . The polynomials are evaluated at the tabulated points and the deviations from the tabulated values are obtained. The polynomial with the best fit over the temperature range of particular interest, namely where the phase is stable, should be selected, but in the event of a near tie between two or more polynomials, the lowest order polynomial should be selected, with the unused coefficients being set to zero. For monatomic neutral species in the gas phase and for free electrons,  $\Delta G_{pi}(T)$  is zero by definition for all  $T$ . Because discontinuities associated with phase changes of the elements in their standard reference states have been removed,  $\Delta G_{pi}(T)$  varies smoothly as a function of  $T$ , and eq. (44) should represent a good fit over the temperature range required. Once a good fit has been obtained, the data can be added to a thermodynamic database.

In performing the calculation for a particular temperature, pressure, and composition, the Gibbs free energy for each species of interest is obtained from the database using the fitted coefficients at the temperature required, then the total free energy of the system is minimized to obtain the abundances of the gas-phase species, together with any condensates. The total dimensionless free energy is given by

$$\frac{G(T)}{RT} = \sum_{i=1}^m \left[ n_{1i} \left\{ \frac{\Delta G_{1i}(T)}{RT} + \ln P + \ln \left( \frac{n_{1i}}{N} \right) \right\} \right] + \frac{1}{RT} \sum_{p=2}^{s+1} \left[ n_{p1} \Delta G_{p1}(T) \right], \quad (45)$$

where  $R$  is the gas constant, and for the first sum for the gas phase with  $p = 1$ ,  $P$  is the total pressure in atmospheres,  $N$  is the number of moles,  $m$  is the number of species,  $n_{1i}$  is the number of moles of species  $i$ , and  $\Delta G_{1i}(T)$  is the corresponding free energy of that species. The second sum is over the  $s$  condensed phases, which may include multiple phases of the same species, but except at a phase boundary, only one phase of a particular species in a condensed form is present at any time, since we have not considered solid or liquid solutions. Consequently,  $n_{p1}$  is the number of moles of a condensed species and  $\Delta G_{p1}(T)$  is the corresponding free energy of that species. Since there is only one species per phase, for convenience we have set  $i$  equal to 1.

Equation (45) then has to be minimized, subject to the constraint given by the mass balance for each element  $j$

$$\sum_{i=1}^m \nu_{1ij} n_{1i} + \sum_{p=2}^{s+1} \nu_{p1j} n_{p1} = b_j, \quad (46)$$

where  $\nu_{1ij}$  and  $\nu_{p1j}$  are the stoichiometric coefficients of the species containing the element, and  $b_j$  is the total number of gram-atoms of that element in all forms. When ionized species are considered,  $j$  includes the electron as an “element,” which can have positive or negative stoichiometric coefficients, but it must sum to zero for net charge neutrality; thus, the corresponding value of  $b_j$  is zero. The solution is found by the method of Lagrange undetermined multipliers and Taylor expansions about an arbitrary point after starting with trial abundances, as described by Eriksson (1971) and Eriksson & Rosén (1973).

The most efficient method is to perform a set of calculations at a given pressure and  $Z$  for a sequence of decreasing temperatures at one degree intervals, starting at a temperature above the range of interest, in particular above the condensation temperature of the most refractory species, using arbitrary starting values for the first iteration. For each new temperature down in the sequence, the abundances from the previous temperature can be used as starting values. This can be very efficient, and not much would be gained in computing time by using larger temperature intervals at the expense of fewer temperature points covered. As the temperature decreases, the first appearance or disappearance of a condensed phase should be noted, in order to follow the condensation sequence with decreasing temperature. When a phase disappears with decreasing temperature, it always changes into one or more other condensed phases. The only exception for a realistic astrophysical mixture might be graphite, which can convert into  $CH_4$  in a carbon-rich ( $[C]/[O] > 1$ ) mixture at low temperatures.

At higher temperatures, convergence is generally very rapid, but as the temperature decreases and more condensed phases appear, the iterations slow down, and there is a greater likelihood of convergence failing at some low temperatures. This problem can usually be cured by removing species that have negligible abundances, but still adversely affects the processing time. In some cases at low temperatures it is possible for the code to converge to solutions where the element abundances or net charge neutrality are not valid, i.e. eq. (46) does not balance. This can be checked by calculating residuals using

$$r_j = \frac{b_j - s_j}{b_j}, \quad (47)$$

where  $r_j$  is the residual fraction for element  $j$ ,  $b_j$  is the specified abundance, as in eq. (46), and  $s_j$  is the sum of the abundances multiplied by the stoichiometric coefficients of all species containing element  $j$  on the left hand side of eq. (46). In the case of charge conservation for  $j$  corresponding to electrons as an “element,”  $r_j$  is just the sums on the left hand side of eq. (46), i.e.  $r_j = s_j$ .

Working in double precision with an accuracy of about 15 significant figures, if  $r_j$  is substantially larger in magnitude than  $O(10^{-15})$ , the calculations should be discarded, and if necessary repeated with some of the very low abundance species removed.

As discussed previously, because of the expense in calculating some of the opacities, tables should be precomputed at selected temperatures and pressures, then when required opacities can be calculated by interpolation. Additionally, for those opacities that do not require extensive precomputations and are not already in precomputed tabular form, they can be calculated on the fly when required. In all cases, the final mass opacities in  $\text{cm}^2 \text{g}^{-1}$  require the abundances of the absorbing species to be known for the given temperature, pressure, and chemical composition at which the calculations are being performed.

In the equilibrium calculations performed for the plots presented here, a subset of 30 gas-phase species out of nearly 350 gas-phase species were selected for detailed treatment. The species are the neutral atoms:  $H$ ,  $He$ ,  $Li$ ,  $Na$ ,  $K$ ,  $Rb$ ,  $Cs$ ,  $Al$ ,  $Ca$ , and  $Fe$ , the ions:  $e^-$ ,  $H^+$ , and  $H^-$ , the metal hydrides:  $MgH$ ,  $CaH$ ,  $FeH$ ,  $CrH$  and  $TiH$ , with the remaining molecules being  $H_2$ ,  $N_2$ ,  $CO$ ,  $SiO$ ,  $TiO$ ,  $VO$ ,  $CaOH$ ,  $H_2O$ ,  $H_2S$ ,  $NH_3$ ,  $PH_3$ , and  $CH_4$ . Out of these,  $Al$ ,  $Ca$ ,  $N_2$ , and  $CaOH$  are not discussed here, but their abundances can be important. Note that like  $H_2$ ,  $N_2$  is a symmetric molecule with no net dipole moment, and in planetary/satellite atmospheres like of the Earth or Titan is a source of CIA opacities in the infrared, as well as collisional broadening of lines. Although the temperature is too low for scattering due to  $e^-$  to be of any importance, the abundance of free electrons indicates the level of ionization, and thus indirectly the contribution due to the absorption produced by  $H^-$ .



Although we are discussing calculations involving only a solar composition, a large range of stellar metallicities exist, even for nominally Population I compositions. It is thus expected that the metallicities of substellar objects will also have a large range. To cover the large ranges in temperature, pressure, and metallicity expected, a recommended set of values could be as follows:

$$\begin{aligned} 50 \text{ K} \leq T \leq 5000 \text{ K} & \quad \text{in steps of } \Delta \log T = 0.0025, \\ 8 \times 10^{-8} \text{ Atm} \leq P \leq 400 \text{ Atm} & \quad \text{in steps of } \Delta \log P = 0.1, \\ 0.01 Z_{\odot} \leq Z \leq 3.16 Z_{\odot} & \quad \text{in steps } \Delta \log Z = 0.5, \end{aligned}$$

and at each value of  $T$ ,  $P$ , and  $Z$  the abundances of each of a selected subset of species, say 30, could be stored for later use in opacity calculations.

In order to see how the abundances of a number of important species vary with temperature, Figs. 17, 18, 19, and 20, show the  $\log_{10}$  of the mixing fractions as a function of temperature between 100 and 4000 K at a total gas pressure of 1 atmosphere for a number of species. All the figures are plotted with the same scales to make comparisons easier, with the  $\log_{10}$  of the mixing fractions plotted from -18 to -2. The molecule  $H_2$  is the most abundant species over most of the temperature range, so is not plotted. At the highest temperatures here atomic hydrogen replaces  $H_2$  as the most abundant species, and is likewise omitted.

Figure 17 is a plot of the abundances of the molecules discussed in §2.1, namely  $H_2O$ ,  $NH_3$ ,  $CH_4$ , and  $CO$ , the abundances discussed in §2.2,  $TiO$  and  $VO$ , and  $H_2S$  and  $PH_3$  from §2.4. In addition, because of the importance of the equilibrium between  $N_2$  and  $NH_3$ ,  $N_2$  is also included. Since  $CO$  has a very high dissociation energy, and since the abundance of oxygen likely exceeds that of carbon, virtually all carbon is tied up in  $CO$ , with the surplus oxygen being bound in  $H_2O$ , excepting some partial dissociation of  $H_2O$  at the very highest temperatures and the formation of other oxides and condensates containing oxygen. With decreasing temperature a point is reached where  $CO$  reacts with  $H_2$  to form  $CH_4$ , which replaces  $CO$  as the dominant carbon-bearing species. In the process, the oxygen tied up in  $CO$  becomes available to form additional  $H_2O$ , which more than compensates for some of the oxygen that has in the mean time been removed from  $H_2O$  to form various condensates, mostly those of silicon and magnesium.

Like  $CO$  with oxygen,  $N_2$  is the most abundant nitrogen bearing species at high temperatures, because  $N_2$  also has a very high dissociation potential, and like  $CO$ , with decreasing temperature it reacts with  $H_2$  to form  $NH_3$ , which replaces it as the most abundant nitrogen-bearing species at low temperatures. However, nitrogen is only weakly coupled to the rest of the system, because other compounds containing nitrogen have low abundances. Both  $TiO$  and  $VO$  are influenced by the formation of condensates, that cause them to be very rapidly removed from the gas phase when the condensates form (Lodders 2002). If rainout did not take place,  $Fe$  would react with  $H_2$ , causing  $FeS$  to form and the abundance of  $H_2S$  would rapidly fall like  $TiO$  and  $VO$ , but because  $Fe$  has been removed from system, the abundance of  $H_2S$  does not decrease with decreasing temperature (Fegley & Prinn 1983; Visscher, Lodders & Fegley 2006).

Figure 18 shows the mixing fractions of the metal hydrides, whose opacities are discussed in §2.3, Fig. 19 shows the corresponding fractions of the alkali elements discussed in §2.6, and Fig. 20 shows the corresponding fractions of a number of species discussed in §3.2 and §2.5. With the exception of the  $H^-$  ion, all the abundances start dropping rapidly at some specific temperature due to the formation of condensates, which remove elements forming condensates from the gas phase.

Figure 21, which is plotted on the same scales as the previous four figures, shows the mixing fractions of  $CH_4$ ,  $FeH$ , and  $CrH$  for pressures of 0.001, 0.01, 0.1, 1, and 10 atmospheres, and Fig. 22 is the same for the abundances of  $TiO$ ,  $VO$ , and  $K$ . With the exception of  $CH_4$ , all the abundances fall rapidly at some point due to the formation of condensates.

## 5. CONCLUSION

In this work, we have discussed and detailed the main sources of opacity in the cool atmospheres of brown dwarfs and extrasolar giant planets. Since these objects have lower atmospheric temperatures than stars, a number of diatomic and polyatomic molecules are present, which are not found in abundance in most stellar types. Such molecules can have a very complicated spectrum with a large number of lines. Because of the complex spectrum of molecules, and because they are such important sources of absorption, a considerable amount of effort is required to calculate their contribution to the opacity. Detailed calculations for many millions of lines over an extensive frequency grid are involved.

Most other papers dealing with the opacities in the atmospheres of substellar objects, consider only one or a few specific molecules, often in a restricted wavelength region. This is one of the first papers to provide in one place a comprehensive discussion of the important molecular and atomic opacity sources, covering a broad range of wavelengths from the near ultraviolet through to the far infrared.

In practical opacity calculations, once the monochromatic absorption of each species has been considered, their abundances have to be calculated before they can be combined to obtain total opacities. The minimization of the free energy of the system can be used to determine equilibrium abundances, and we have provided a comprehensive summary of the techniques needed to derive such abundances and results of such calculations. Once the complete monochromatic opacities are obtained, mean opacities weighted by abundances can be calculated.

In order to model substellar objects correctly, a knowledge of how the atmosphere absorbs radiation is necessary. This paper is meant to provide a compendium of approaches, references, and results to aid the student interested in substellar dense atmospheres and the associated spectroscopy and chemistry.

This work was supported in part by NASA under grants NAG5-10760 and NNG04GL22G. The authors would like to thank Ivan Hubeny for reading the manuscript and providing detailed comments in early drafts. They would also like to thank Richard Freedman for providing guidance with line broadening parameters. Finally, AB acknowledges support through the Cooperative Agreement #NNA04CC07A between the University of Arizona/NOAO LAPLACE node and NASA's Astrobiology Institute.

## REFERENCES

- Alexander, D.R. & Ferguson J.W. 1994, ApJ, 437, 879  
 Allard, F., Hauschildt, P.H., & Schwenke, D. 2001, ApJ, 540, 1005  
 Allard, N.F. et al. 2003 A&A, 411, L473  
 Allende Prieto, C. & Lambert, D.L. 2005, Workshop on Oxygen in the Earliest Solar System, LPI Contribution No. 1278, 9.  
 Allende Prieto, C., Lambert, D.L., & Asplund, M. 2001, ApJ, 556, L63  
 Anders, E. & Grevesse, N. 1989, Geochim. Cosmochim. Acta, 53, 197  
 Asplund, M., Grevesse, N., Sauval, A.J., Allende Prieto, C., & Blomme, R. 2005, A&A, 431, 693  
 Barber, R.J., Tennyson, J., Harris, G.J., & Tolchenov, R.N. 2006, MNRAS, 368, 1087  
 Barin, I. 1995, "Thermochemical Data of Pure Substances," 3rd Edition, ISBN 3-527-28745-0, (VCH: Weinheim, Germany)  
 Bauschlicher, C.W. 1999, Theor. Chem. Acc., 103, 141  
 Bautista, M.A. 1997, A&A Suppl., 122, 167  
 Bauschlicher Jr., C.W., Ram, R.S., Bernath, P.F., Parsons, C.G., & Galehouse, D. 2001, J. Chem. Phys., 115, 1312  
 Bell, K.L. 1980, J. Phys. B, 13, 1859  
 Bell, K.L., Berrington, K.A., & Croskery, J.P. 1982, J. Phys. B, 15, 977  
 Bell, K.L., Hibbert A., & Berrington, K.A. 1988, J. Phys. B, 21, 2319  
 Bell, K.L. & Berrington, K.A. 1987, J. Phys. B, 20, 801  
 Besmann, T.M. 1977, "SOLGASMIX-PV - A computer Program to Calculate Equilibrium Relationships in Complex Chemical Systems," Oak Ridge National Laboratory Report TM-5775  
 Bethe, H.A. & Salpeter, E.E. 1957, "Quantum Mechanics of One- and Two-Electron Atoms," p. 269, equation 63.11 (New York: Academic Press).  
 Borysow, A. & Frommhold L. 1989, ApJ, 341, 549  
 Borysow, A. & Frommhold L. 1990, ApJ, 348, L41  
 Borysow, A., Frommhold L., & Moraldi M. 1989, ApJ, 336, 495  
 Borysow, J., Frommhold L., & Birnbaum G. 1988, ApJ, 326, 509  
 Borysow, J., Trafton L., Frommhold L., & Birnbaum G. 1985, ApJ, 296, 644  
 Borysow, A., Champion, J.P., Jrgensen, U G, & Wenger, C. 2003, in "Stellar Atmosphere Modeling," eds. Ivan Hubeny, Dimitri Mihalas, & Klaus Werner (San Francisco: ASP Conference Proceedings, Vol. 288), p. 352  
 Bouanich, J.-P., Salem, J., Aroui, H., Walrand, J., & Blanquet, G. 2004, J.Q.S.R.T. 84, 195  
 Brown, L.R., Champion, J.P., Hilico, J.C., Loete, M., Nikitin, A., Ouardi, O., & Tyuterev, V.I.G. 1997, Bull. AAS, 29, 1010  
 Brown, L. R., Nemtchinov, V., Cottaz, C., Kleiner, I., & Tarrago, G. 2000, Bull. AAS, 32, 1108  
 Brown, L. R., Dulick, M. & Devi, V.M. 2001, Bull. A.A.S., 33, 1142  
 Burrows, A., Marley, M.S., Hubbard, W.B., Lunine, J.I., Guillot, T., Saumon, D., Freedman, R., Sudarsky, D., & Sharp, C.M. 1997, ApJ, 491, 856  
 Burrows, A., Marley, M.S., & Sharp, C.M. 2000, ApJ, 531, 438  
 Burrows, A. & Sharp, C. 1998, ApJ, 512, 843  
 Burrows, A., Ram, R.S., Bernath, P., Sharp, C.M., & Milsom, J.A. 2002, ApJ, 577, 986  
 Burrows, A. & Sharp, C.M. 1999 ApJ, 512, 843  
 Burrows, A., Dulick, M., Bauschlicher, Jr., C.W., Bernath, P.F., Ram, R.S., Sharp, C.M., & Milsom, J.A. 2005, ApJ, 624, 988  
 Burrows, A. & Volobuyev, M. 2003, ApJ, 583, 985  
 Carson, T.R. 1988a, A&A, 189, 319  
 Carson, T.R. 1988b, A&A Suppl., 75, 385  
 Castelli, F. & Kurucz, R.L. 2003, "New Grids of ATLAS9 Model Atmospheres" in "Proceedings of the 210th Symposium of the International Astronomical Union" Uppsala University, Uppsala, Sweden, 17-21 June, 2002. Eds. N. Piskunov, W.W. Weiss & D.F. Gray. Published on behalf of the IAU by the Astronomical Society of the Pacific, 2003., p.A20  
 Chase, M.W. 1982, *JANAF Thermodynamic Tables*, Magnetic Tape Version (Midland, MI: Dow Chemical Co.).  
 Chase, M.W., Davies, C.A., Downey, J.R., Frurip, D.J., McDonald, R.A., & Syverud, A.N. 1985, *JANAF Thermodynamic Tables*, J. Phys. Chem. Ref. Data Suppl., 14, 1  
 Courtin, R. 2004, Observatoire de Paris-Meudon, private communication  
 Cunto W. & Mendoza C. 1992, Rev. Mexicana Astron. Astrofis., 23, 107  
 Cunto W., Mendoza C., Ochsenbein F., & Zeippen C.J. 1993, A&A, 275, L5  
 Deirmendjian, D. 1964, Applied Optics, 3, 187  
 Deirmendjian, D. 1969, "Electromagnetic Scattering on Spherical Polydispersions," (New York: Elsevier)  
 Dimitrijević, M.S. & Peachi, G. 1990, A&A, 236, 261  
 Dorschner, J., Begemann, B., Henning, T., Jäger, C., & Mutschke, H. 1995, A&A, 300, 503  
 Dulick, M., Bauschlicher, Jr., C.W., Burrows, A., Sharp, C.M., Ram, R.S., & Bernath, P. 2003, ApJ594, 651  
 Dunning, T.H. 1989, J. Chem. Phys., 90, 1007  
 Eisenberg, D. & Kauzmann, W. 1969, *The Structure and Properties of Water*, (New York: Oxford University Press).  
 Eriksson, G. 1971, Acta Chem. Scandinavia, 25, 2651  
 Eriksson, G. & Rosén, E., 1973, Chem. Scripta, 4, 193  
 Fegley, B., Jr. & Lodders, K. 2001, Meteoritics & Planetary Science Suppl., 36, A55  
 Fegley, B., Jr. & Prinn. R.G. 1983, Lunar and Planetary Science, XIV, 189  
 Fraser, F.A. 1954, Can. J. Phys., 32, 515  
 Fuhrmann, K., Pfeiffer, M.J., & Bernkopf, J. 1998, A&A, 336, 942  
 Goorvitch, D. 1994, ApJS, 95, 535  
 Guillot T., Gautier D., Chabrier G., & Mosser B. 1994, Icarus 112, 337.  
 Lide, D.R., Ed. of Handbook of Chemistry and Physics, 74th Edition 1993, CRC Press Inc.  
 Herzberg, G. 1950, "Molecular Spectra and Molecular Structure: I - Spectra of Diatomic Molecules," (New York: Van Nostrand Reinhold Company)  
 Herzberg, G. 1966, "Molecular Spectra and Molecular Structure: III - Electronic Spectra and Electronic Structure of Polyatomic Molecules," (New York: Van Nostrand Reinhold Company)  
 Herzberg, G. 1968, "Molecular Spectra and Molecular Structure: II - Infrared and Raman Spectra of Polyatomic Molecules," (New York: Van Nostrand Reinhold Company)  
 Huber, K.P. & Herzberg, G. 1979, "Molecular Spectra and Molecular Structure: IV. Constants of Diatomic Molecules," (New York: Van Nostrand Reinhold Company)  
 Hummer, D.G. & Mihalas, D. 1988, ApJ, 331, 815  
 Irvine, W.M. 1964, Journal of the Optical Society of America, 55, 16  
 Jacquinet-Husson N. et al. 1999, "The 1997 spectroscopic GEISA databank," JQSRT, 62, 205-54  
 Jacquinet-Husson N. et al. 2003, "The 2003 Edition of GEISA : A spectroscopic database system for the second generation vertical sounders radiance simulation. Proceedings of the 13th International TOVS Study Conference (ITSC-13); 28 October 4 November 2003, Sainte-Adle, Canada"  
 Jacquinet-Husson, N. et al. 2005, "The 2003 edition of the GEISA/IASI spectroscopic database," J.Q.S.R.T., 95, 429  
 Jørgensen, U.G. 1997, in *Molecules in Astrophysics: Probes and Processes*, ed. E.F. Van Dishoeck, (Amsterdam: Kluwer, IAU Symp. 178), p. 441-456.  
 John, T.L. 1975, MNRAS, 172, 305  
 John, T.L. & Morgan, D.J. 1975, MNRAS, 170, 1  
 Karkoschka, E. 1994, Icarus, 11, 174  
 Kassel, L.S. 1933a, J. Chem. Phys., 1, 576  
 Kassel, L.S. 1933b, Phys. Rev., 43, 364  
 Kissel, A., Sumpf, B., Kronfeldt, H.-D., Tikhomirov, B.A., & Ponomarev, Yu. N. 2002, J. Mol. Spec. 216, 345  
 Kovács, I. 1969, "Rotational Structure in the Spectra of Diatomic Molecules," (London: Adam Hilger Ltd.)

- Kurucz, R.L. 1970, *Smithsonian Obs. Spec. Rep.*, 309, 1-291
- Kurucz, R.L., Van Dishoeck, E.F., & Tarafdar, S.P. 1987, *ApJ*, 322, 992
- Kurucz, R.L. 1993, *Molecular Data for Opacity Calculations*, Cambridge, Mass. Smithsonian Astrophysical Observatory, originally on CD-ROMs now available at <http://kurucz.harvard.edu/>
- Kurucz, R.L. 1995, CD-ROM No. 23. Cambridge, Mass. Smithsonian Astrophysical Observatory
- Lang, K.R. 1999, *Astrophysical Formulae*, 3rd edition (New York: Springer-Verlag)
- Lange's Handbook of Chemistry 1979, ed. J.A. Dean, (New York: McGraw-Hill Book Company)
- Lee, L.C., Wang, X., & Suto, M. 1987, *J. Chem. Phys.*, 86, 4353
- Leininger, T. & Jeung G-H., 1995, *J. Chem. Phys.*, 103, 3942
- Lenzuni P., Chernoff D.F., & Salpeter E.E. 1991, *ApJSuppl.* 76, 759
- Levy A. & Lacombe, N. 1993, *J. Mol. Spec.* 157, 172
- Levy A., Lacombe, N., & Tarrago, G. 1994, *J. Mol. Spec.* 166, 20
- Lodders, K. 1999, *ApJ*, 519, 793
- Lodders, K. 2002, *ApJ*, 577, 974
- Lodders, K. & Fegley B., Jr. 2002, *Icarus*, 155, 393
- Martonchik, J.V., Orton, G.S., & Appleby J.F. 1984, *Applied Optics*, 23, 4
- Mayor, M. & Queloz, D. 1995, *Nature*, 378, 355
- Menzel, D.H. 1969, *A&A Suppl.* 18, 221
- Moore, Charlotte E. 1949, "Atomic Energy Levels," NBS Circular number 467.
- Nakajima, T., Oppenheimer, B.R., Kulkarni, S.R., Golimowski, D.A., Matthews, K., & Durrance, S.T. 1995, *Nature*, 378, 463
- Nefedov, A.P., Sinel'shchikov, V.A., & Usachev, A.D. 1999, *Physica Scripta*, 59, 432
- Nicholls, R.W. 1965, *Proc. Phys. Soc.*, 85, 159
- Nicholls, R.W. & Jarman, W.R. 1956, *Proc. Phys. Soc.*, A69, 253
- Partridge, H. & Schwenke, D.W. 1997, *J. Chem. Phys.*, 106, 4618
- Piskunov, N.E., 1994 "Vienna Atomic Line Database" (VALD), Electronic Mail Service - <http://www.astro.univie.ac.at/~vald/>
- Piskunov, N.E., Kupka, F., Ryabchikova, T.A., Weiss, W.W., & Jeffery, C.S. 1995, *A&A Suppl.*, 112, 525
- Plez, B. 1998, *A&A*, 337, 495
- Polyansky, O.L., Jensen, P., & Tennyson, J. 1994, *J. Phys. Chem.*, 101, 7651
- Rages, K., Pollack, J.B., Tomasko, M.G., & Doose, L.R. 1991, *Icarus*, 89, 359
- Ram, R.S., Jarman, C.N., & Bernath, P.F. 1993, *Journal of Molecular Spectroscopy*, 161, 445
- Ramsbottom, C. A., Bell, K.L., & Berrington, K.A. 1992, *J. Phys. B*, 25, 1443
- Rothman, L.S., Gamache, R.R., Tipping, R.H., Rinsland, C.P., Smith, M.A.H., Benner, D.C., Malathy Devi, V., Flaud, J.-M., Camy-Peyret, C., Perrin, A., Goldman, A., Massie, S.T., Brown, L.R., & Toth, R.A. 1992, *J.Q.S.R.T.*, 48, 469
- Rothman, L.S. et al. "The HITRAN molecular database: edition of 2000 including updates through 2001," 2003, *J.Q.S.R.T.*, 82, 5
- Rothman, L.S. et al. "The HITRAN 2004 molecular spectroscopic database," 2005, *J.Q.S.R.T.*, 96, 139
- Schadee, A. 1967, *J.Q.S.R.T.*, 7, 169
- Schwenke, D.W. 1998, *Faraday Discussions*, 109, 321
- Skory, S, Weck, P.F. Stancil, P.C., & Kirby, K. 2003, *ApJ*, 148, 599
- Sharp, C.M. 1984, *A&A Suppl.*, 55, 33
- Sharp, C.M. & Huebner, W.F. 1990, *ApJS*, 72, 417
- Strong, K., Taylor, F.W., Calcutt, S.B., Remedios, J.J., & Ballards, J., 1993, *J.Q.S.R.T.*, 50, 363
- Sudarsky, D.L. 2002, Ph.D. Thesis
- Tipping, R. 1990, Report on Calculation of Spectroscopic Parameters for Diatomic Molecules of Atmospheric Interest, Univ. of Alabama Report, Dept. of Physics and Astronomy.
- Tsuji, T. 1973, *A&A Suppl.*, 23, 411
- Turkdogan, E.T., 1980, *Physical Chemistry of High Temperature Technology*, US Steel Corp., (New York: Academic).
- Tyuterev, V.I.G., Babikov, Yu.L., Tashkun, S.A., Perevalov, V.I., Nikitin, A., Champion, J.-P., Wegnerm, Ch., Pierre, C., Pierre, G., Hilico, J.-C., & Loete, M. 1994, *J.Q.S.R.T.*, 52, 459
- Varanasi, P. & Chudamani, S. 1989, *Journal of Geophysical Research*, 94, 11175
- Visscher, C., Lodders, K., & Fegley Jr., B. 2006, *ApJ*(accepted for publication)
- Van de Hulst, H.C. 1957 "Light Scattering by Small Particles," (New York: John Wiley & Sons)
- Van de Hulst, H.C. 1974, *A&A*, 35, 209
- Warren, S.G. 1984, *Applied Optics*, 23, 8
- Wattson, R.B. & Rothman, L.S. 1992, *J.Q.S.R.T.*, 48, 763
- Weck, P.F., Schweitzer, A., Stancil, P.C., Hauschildt, P.H., & Kirby, A. 2003a, *ApJ*, 582, 1059
- Weck, P.F., Stancil, P.C., & Kirby, K. 2003b, *J.Chem.Phys.* 118, 9997
- Weise, W.L., Smith, N.W., & Glennon, B.M. 1966, NSRDS-NBS 4, Washington, D.C.: US Department of Commerce, National Bureau of Standards
- Wishart, A.W. 1979, *MNRAS*, 187, 599
- Verner, D.A. & Yakovlev, D.G. 1995 *A&A Suppl.*, 109, 125
- Zheng, C. & Borysow, A. 1995a, *ApJ*, 441, 1995
- Zheng, C. & Borysow, A. 1995b, *Icarus*, 113, 84
- Zhu, C. Babb, J.F., & Dalgarno, A. 2006, *Phy. Rev. A*, 73, 012506

TABLE 1  
SUMMARY LIST OF SPECIES, SECTION NUMBERS, & BAND SYSTEMS

Species	Section	Comments
<i>H</i>	2.5 and 3.2	Lines and continuum
<i>H<sup>-</sup></i>	3.2	Continuum present when free electrons are also present
<i>He</i>	3.3	Important for CIA and line broadening
<i>Li</i>	2.6	Alkali element - lines
<i>Na</i>	2.6 and 3.2	Alkali element - lines and continuum
<i>K</i>	2.6 and 3.2	Alkali element - lines and continuum
<i>Fe</i>	2.5 and 3.2	Lines and continuum
<i>Rb</i>	2.6	Alkali element - lines
<i>Cs</i>	2.6	Alkali element - lines
<i>H<sub>2</sub></i>	2.5 and 3.3	CIA, and <i>B - X</i> and <i>C - X</i> UV bands
<i>CO</i>	2.1 and 2.5	Vib-rot bands in IR and <i>A - X</i> band system in UV
<i>SiO</i>	2.5	<i>A - X</i> band system in UV
<i>H<sub>2</sub>O</i>	2.1 and 2.5	Rot and vib-rot bands in IR and absorption in UV
<i>NH<sub>3</sub></i>	2.1	Vib-rot bands in IR
<i>CH<sub>4</sub></i>	2.1 and 3.3	Vib-rot bands in IR
<i>H<sub>2</sub>S</i>	2.4 and 2.5	Pre-computed vib-rot bands in IR and absorption in UV
<i>PH<sub>3</sub></i>	2.4	Pre-computed vib-rot bands in IR
<i>TiO</i>	2.1	$\alpha$ , $\beta$ , $\gamma$ , $\gamma'$ , $\delta$ , $\epsilon$ , and $\phi$ band systems
<i>VO</i>	2.1	<i>A - X</i> , <i>B - X</i> and <i>C - X</i> band systems
<i>TiH</i>	2.3	<i>A - X</i> and <i>B - X</i> band systems
<i>CrH</i>	2.3	<i>A - X</i> band system
<i>FeH</i>	2.3	<i>F - X</i> band system
<i>MgH</i>	2.3	<i>X - X</i> , <i>A - X</i> and <i>B' - X</i> systems
<i>CaH</i>	2.3	<i>A - X</i> , <i>B - X</i> and <i>D - X</i> systems
<i>MgSiO<sub>3</sub></i>	3.4	Enstatite in Mie theory
<i>H<sub>2</sub>O</i>	3.4	Water in Mie theory

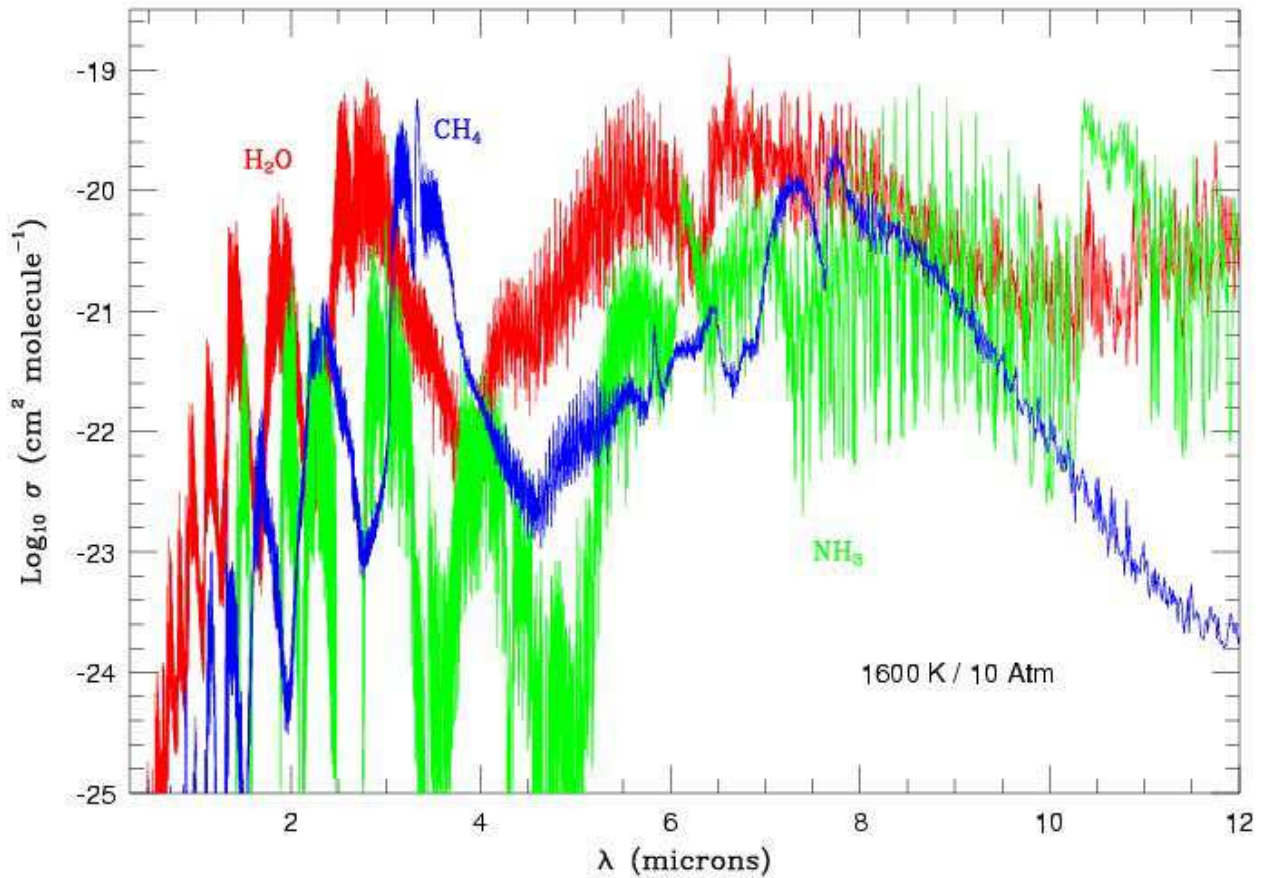


FIG. 1.— The log (base 10) of the monochromatic absorption  $\sigma$  in  $\text{cm}^2\text{molecule}^{-1}$  as a function wavelength  $\lambda$  in  $\mu\text{m}$  in the infrared at a temperature of 1600 K and a pressure of 10 atmospheres for the vibration-rotation transitions of  $\text{H}_2\text{O}$ ,  $\text{NH}_3$ , and  $\text{CH}_4$ , as indicated by the red, green, and blue curves, respectively. The contribution due to different isotopes is included here and in all other figures, when data are available and relevant. The temperature and pressure chosen here are reasonably representative, in particular the lines are sufficiently broadened at 10 atmospheres that the very rapid fluctuations in absorption over short wavelength intervals are suppressed so that the main band features can be more easily seen. At significantly lower pressures the broadening of the lines is much smaller and the absorption can change so rapidly in short wavelength intervals that the main features do not show up so clearly. As can be seen here,  $\text{H}_2\text{O}$  has a strong absorption feature just shortward of  $3 \mu\text{m}$ , and  $\text{CH}_4$  has a strong peak near of  $3.3 \mu\text{m}$ . In the region of  $8 \mu\text{m}$  to  $9 \mu\text{m}$  all three molecules absorb strongly; however, between about  $10.5 \mu\text{m}$  and  $11 \mu\text{m}$   $\text{NH}_3$  has absorption which is distinctly higher than that of the other two molecules. When the combined opacity is calculated, the individual absorptions must be weighted by the abundances. (See text for discussion.)

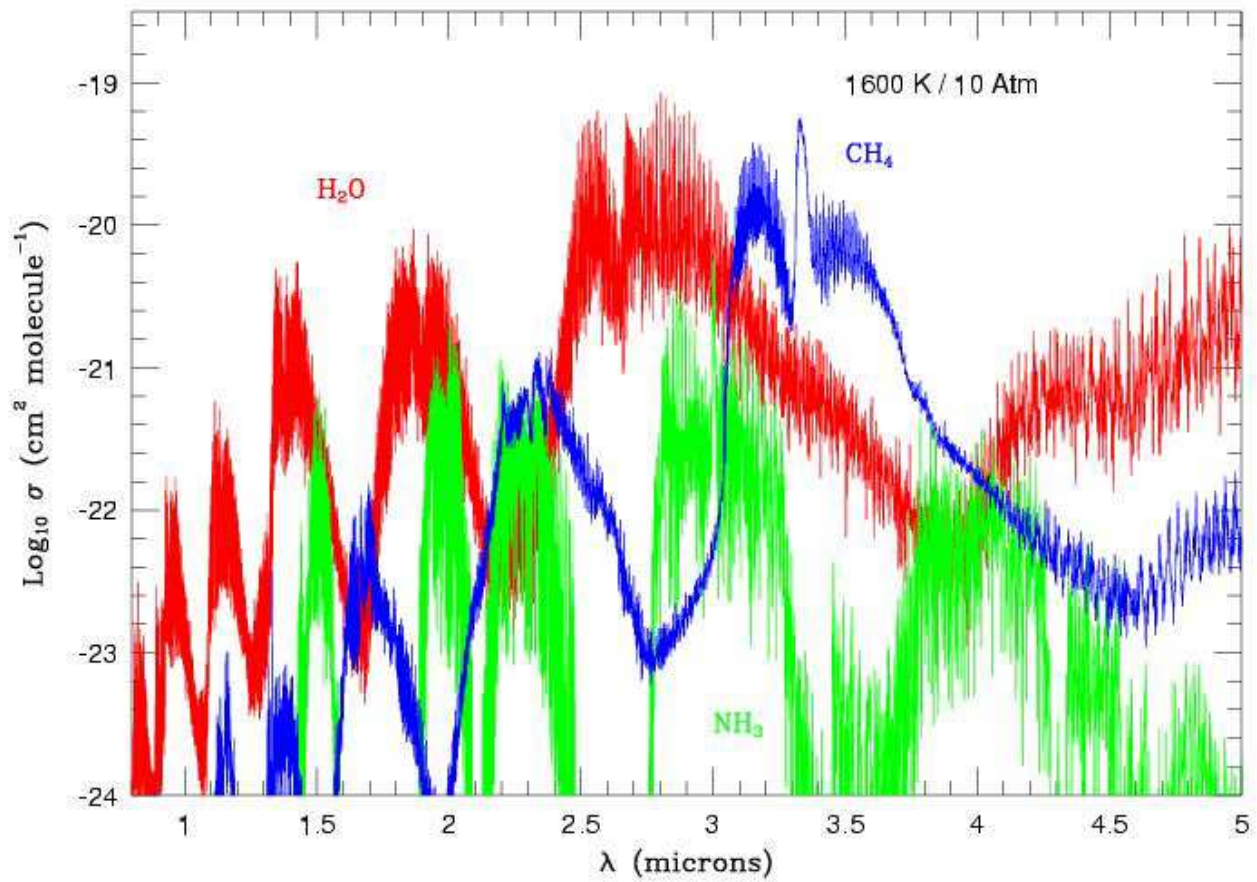


FIG. 2.— This is the same as the previous figure, but with the shorter wavelength region much expanded, together with a small increase in scale of the ordinate, and shows in greater detail the absorption at shorter infrared wavelengths. Of particular interest are the positions and structures of the bands due to  $H_2O$  and  $CH_4$ .

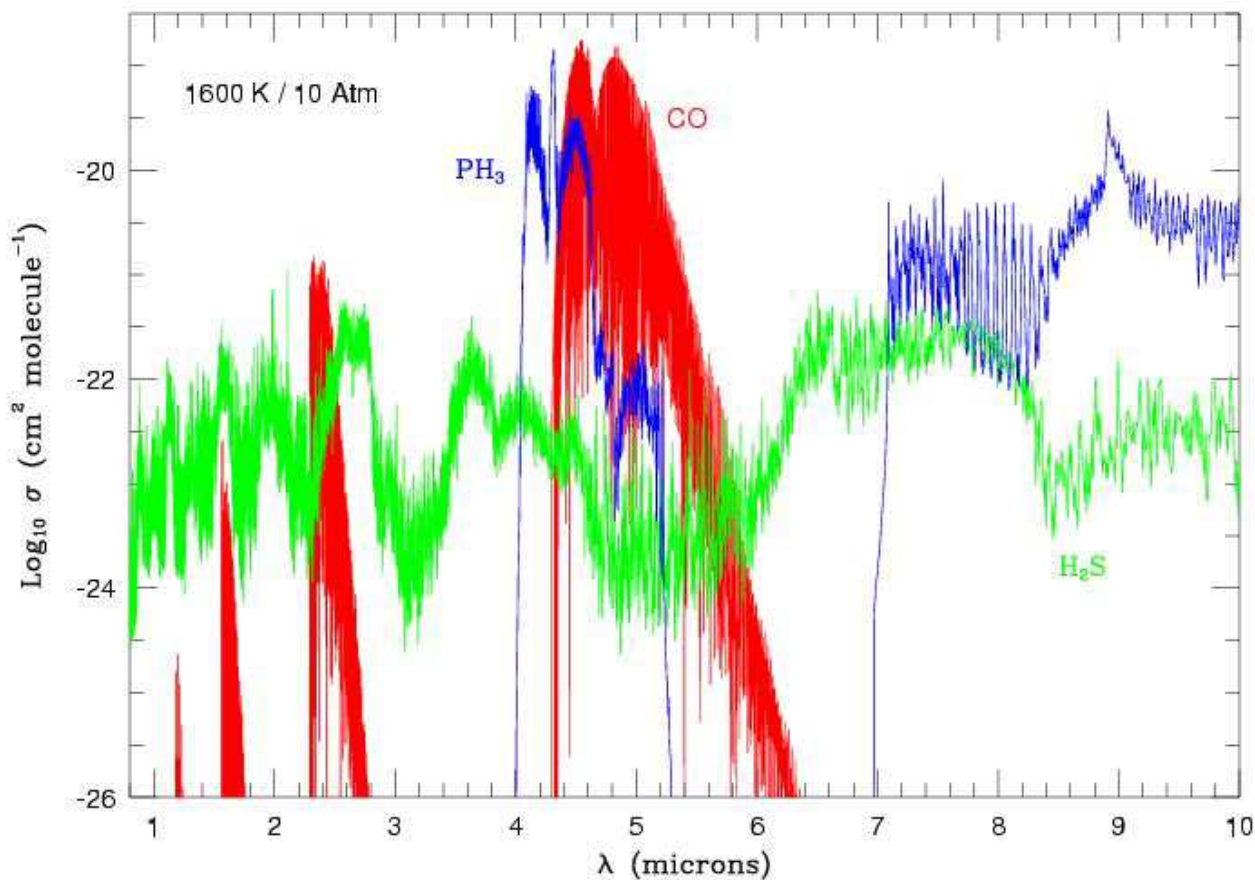


FIG. 3.— The log (base 10) of the monochromatic absorption  $\sigma$  in  $\text{cm}^2\text{molecule}^{-1}$  as a function wavelength  $\lambda$  in  $\mu\text{m}$  in the infrared at the same temperature and pressure of the previous figures for vibration-rotation transitions of  $\text{CO}$ ,  $\text{H}_2\text{S}$ , and  $\text{PH}_3$ , as indicated by the red, green, and blue curves, respectively. Since  $\text{CO}$  is a diatomic molecule with no electron spin or orbital angular momentum in its ground electronic state, the spectra are particularly simple with bands caused by only  $P$ - and  $R$ -branches, together with isotopic versions. The very strong absorption at  $\sim 5 \mu\text{m}$  is due to the fundamental (first harmonic) vibration-rotation transition of  $\text{CO}$ . The progressively weaker bands at progressively shorter wavelengths are due to the second, third and fourth harmonics. Note the strongest peak in  $\text{PH}_3$  absorption partially overlaps the  $\text{CO}$  first harmonic absorption, but a second peak at  $9 \mu\text{m}$  is clear from  $\text{CO}$  absorption. However, both  $\text{H}_2\text{S}$  and  $\text{PH}_3$  have low abundances, and have to compete with much more abundant  $\text{H}_2\text{O}$ ,  $\text{NH}_3$ , and  $\text{CO}$  or  $\text{CH}_4$ . Note that for a given pressure the region in temperature over which  $\text{CO}$  and  $\text{CH}_4$  are of comparable abundances is relatively narrow; otherwise, most carbon is either in  $\text{CO}$  or  $\text{CH}_4$ .



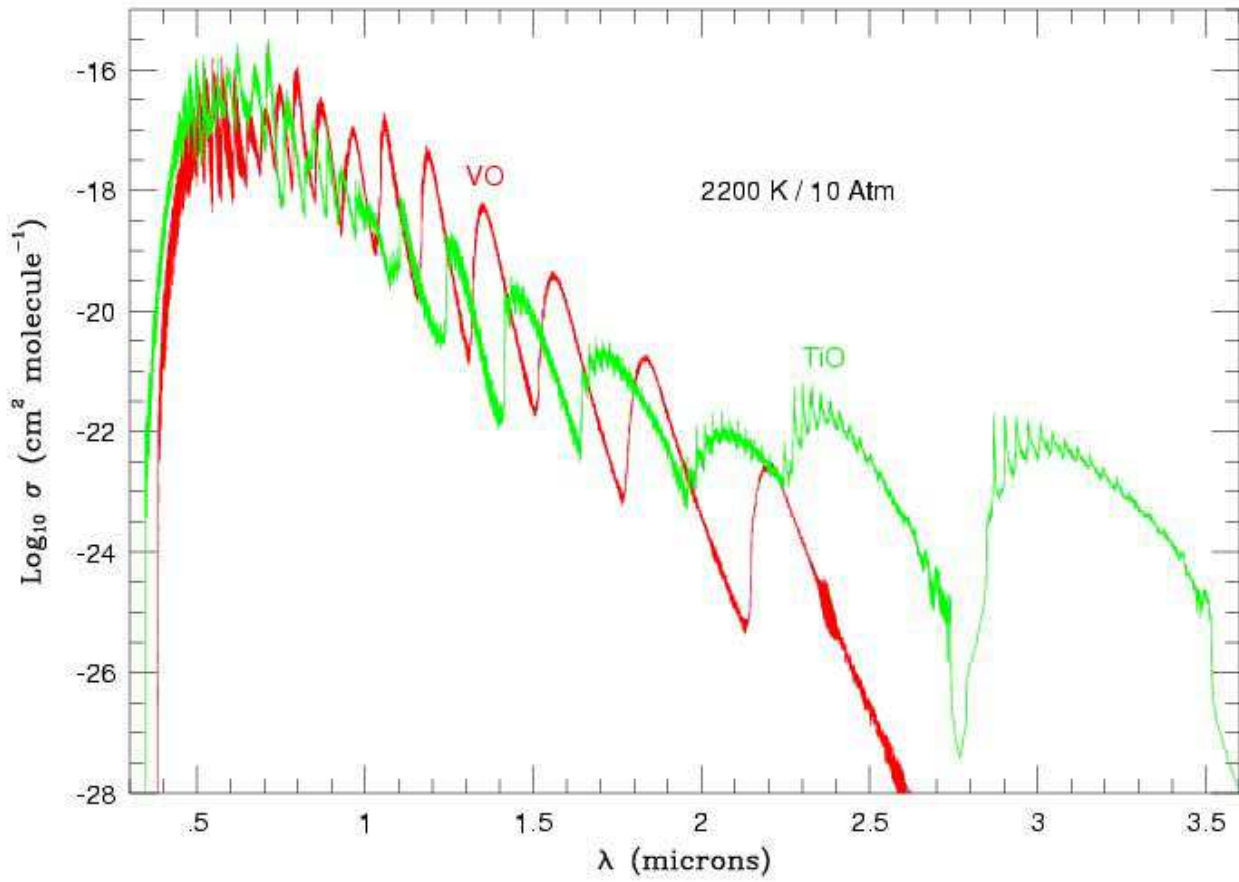


FIG. 4.— The log (base 10) of the monochromatic absorption  $\sigma$  in  $\text{cm}^2\text{molecule}^{-1}$  as a function wavelength  $\lambda$  in  $\mu\text{m}$  in the infrared and visible at a temperature of 2200 K and a pressure of 10 atmospheres for *VO* (red curve) and *TiO* (green curve). Unlike the previous figures, the absorption here is due to electronic transitions, with three systems being calculated for *VO* and seven for *TiO*. Note that the two molecules are very similar, but band strengths of *TiO* drop off more slowly with increasing wavelengths.



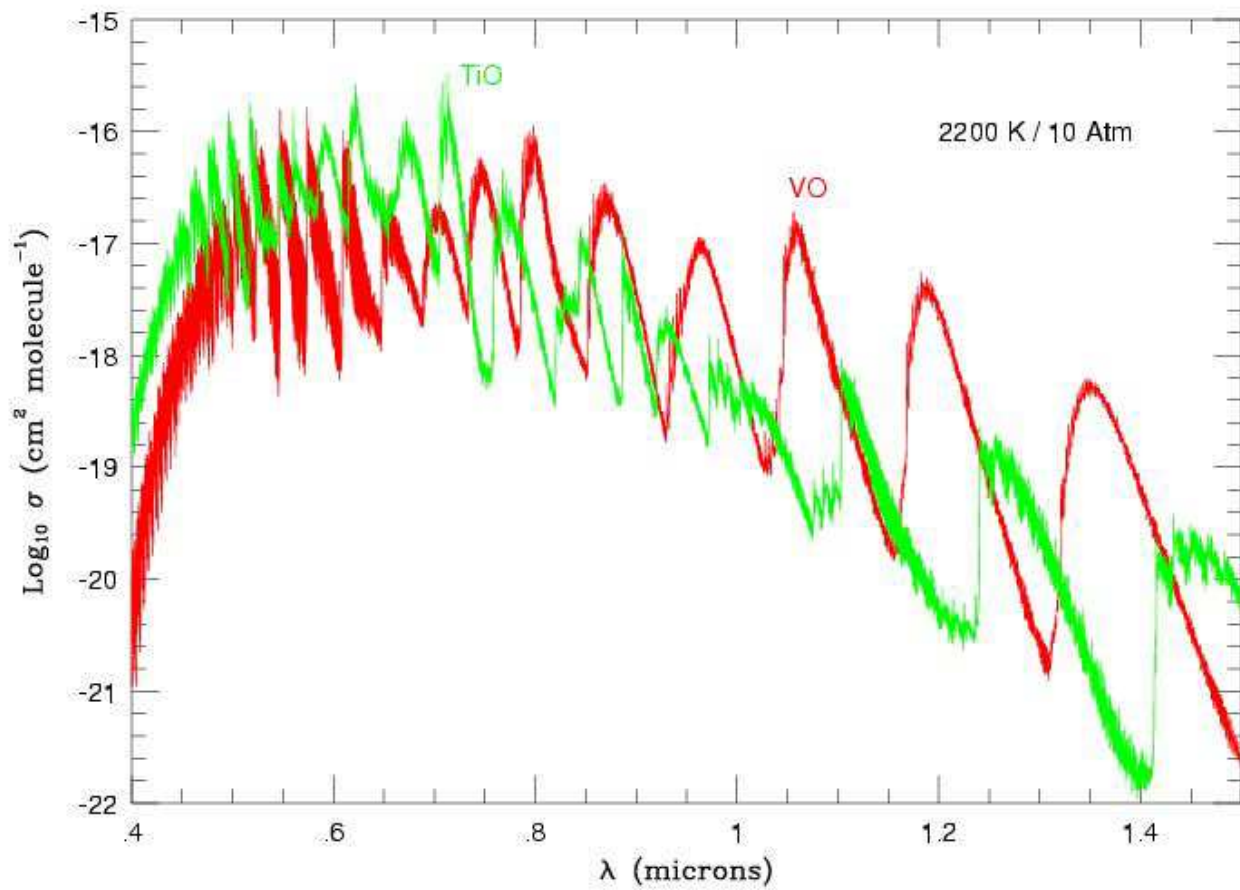


FIG. 5.— The same as the previous figure, but with the shorter wavelength region being represented by expanded wavelength and absorption scales, in order to show the differences between the *VO* and *TiO* absorptions.

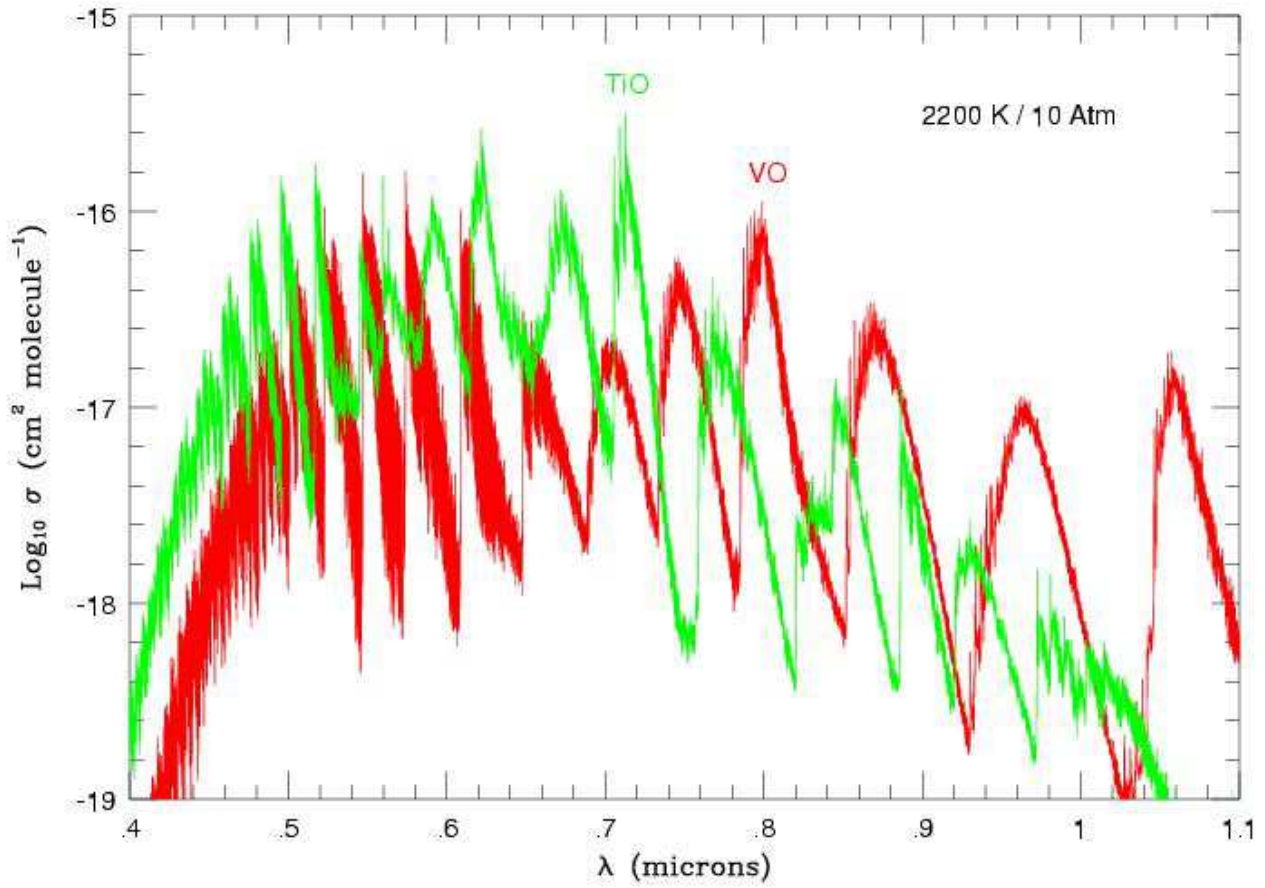


FIG. 6.— A further expansion in scales of the short wavelength region of Fig. 4 to show the differences between the *VO* and *TiO* absorptions. As can be seen, the strongest *TiO* absorption at about  $0.71 \mu\text{m}$  occurs where *VO* absorption is relatively low, and there are several other places where peaks in *TiO* absorption take place where there are troughs in *VO* absorption, and visa versa; this is not so clear at smaller scales.

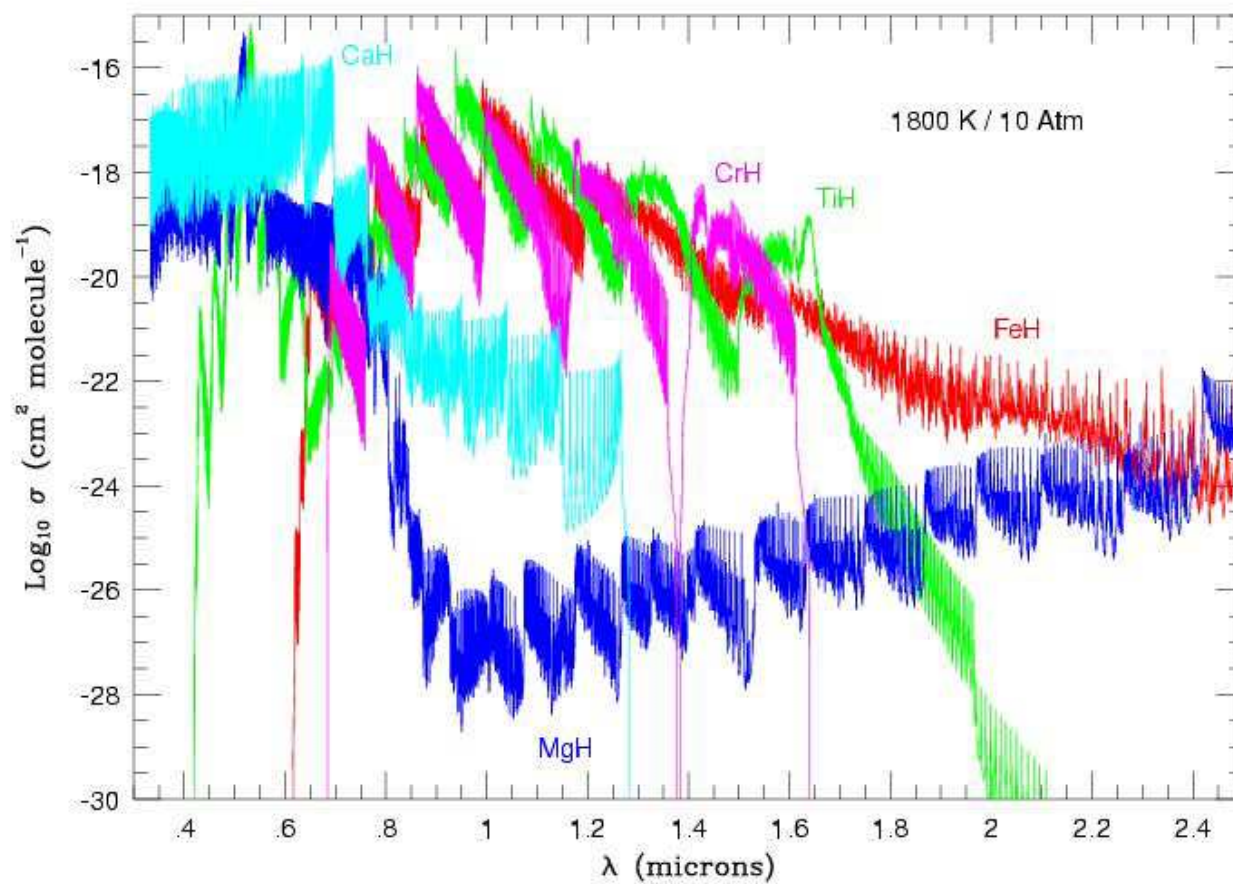


FIG. 7.— The log (base 10) of the monochromatic absorption  $\sigma$  in  $\text{cm}^2 \text{ molecule}^{-1}$  as a function wavelength  $\lambda$  in  $\mu\text{m}$  in the infrared and visible at a temperature of 1800 K and a pressure of 10 atmospheres for the five metal hydrides  $\text{FeH}$ ,  $\text{TiH}$ ,  $\text{MgH}$ ,  $\text{CrH}$ , and  $\text{CaH}$ , represented, respectively, in red, green, blue, magenta, and cyan. All the bands are due to electronic transitions, except that for  $\text{MgH}$ , which includes vibration-rotation transitions in the ground  $X$  electronic state, in addition to the  $A - X$  and  $B' - X$  electronic systems.

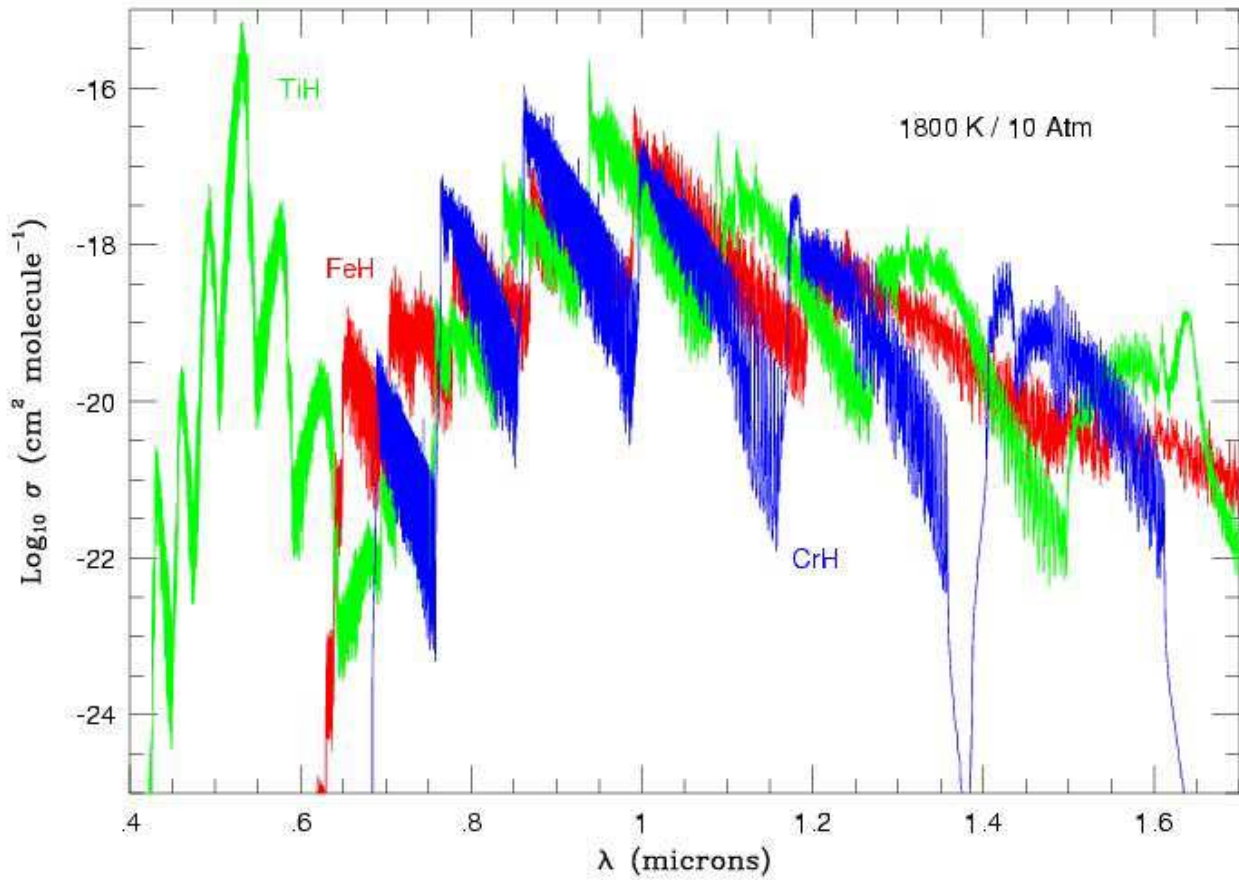


FIG. 8.— A subset of  $FeH$  (red),  $TiH$  (green), and  $CrH$  (blue), taken from the previous figure and plotted on a larger scale to show more detail. The absorption due to the  $F - X$  electronic system of  $FeH$ , the  $A - X$  system of  $TiH$ , and the  $A - X$  system of  $CrH$  all very strongly overlap longward of about  $0.65 \mu\text{m}$ . In addition, we have the data for the  $B - X$  system of  $TiH$ , which stands out on its own here at the shortest wavelengths.

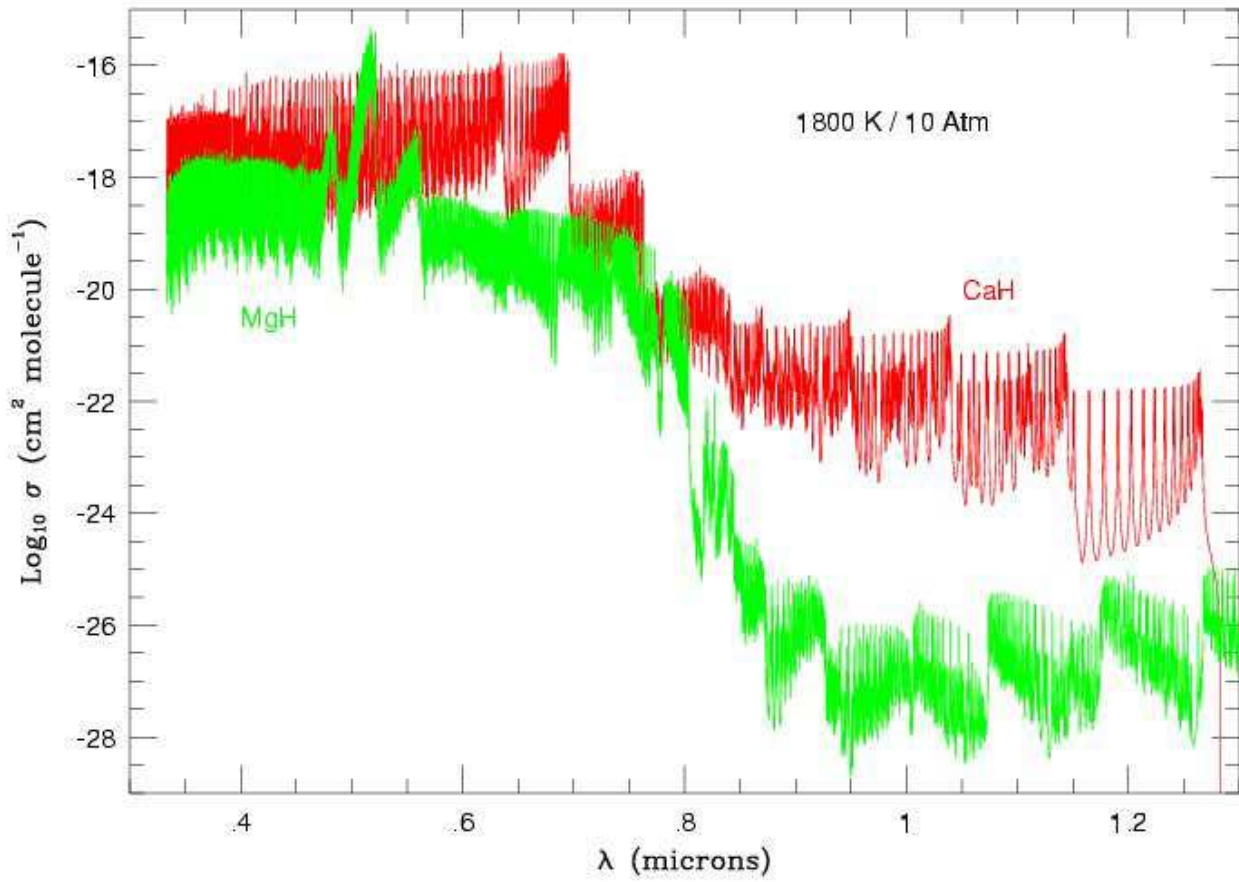


FIG. 9.— A subset of *CaH* (red) and *MgH* (green) taken from Fig. 7 and plotted on larger scales. The absorption produced by *CaH* is calculated from the *A* – *X*, *B* – *X*, and *D* – *X* system, and that due to *MgH* is calculated from the *X* – *X* (vibration-rotation), *A* – *X*, and *B*' – *X* systems, with the *X* – *X* being the only source of absorption of *MgH* longward of about 1  $\mu\text{m}$ .

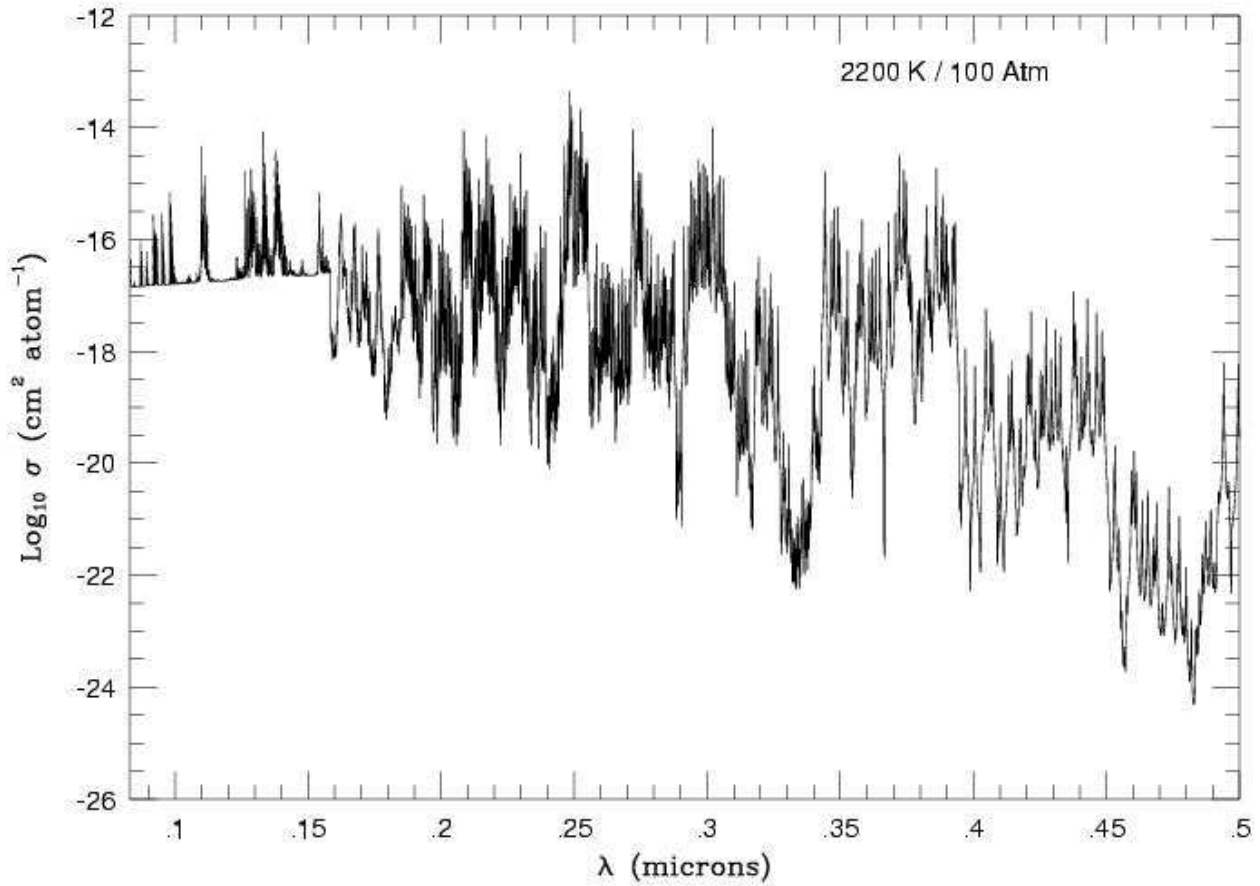


FIG. 10.— The log (base 10) of the sum of the monochromatic absorption  $\sigma$  in  $\text{cm}^2\text{atom}^{-1}$  as a function wavelength  $\lambda$  in  $\mu\text{m}$  due to the contributions of line and bound-free transitions of atomic iron at 2200 K and 100 atmospheres in the visible and ultraviolet parts of the spectrum. A pressure of 100 atmosphere is high, but as the absorption changes so rapidly over very short wavelength intervals, this is adopted here so that the general behavior of absorption can be represented graphically. At the shortest wavelengths, the minimum absorption is clearly governed by the contribution due to the bound-free transition.



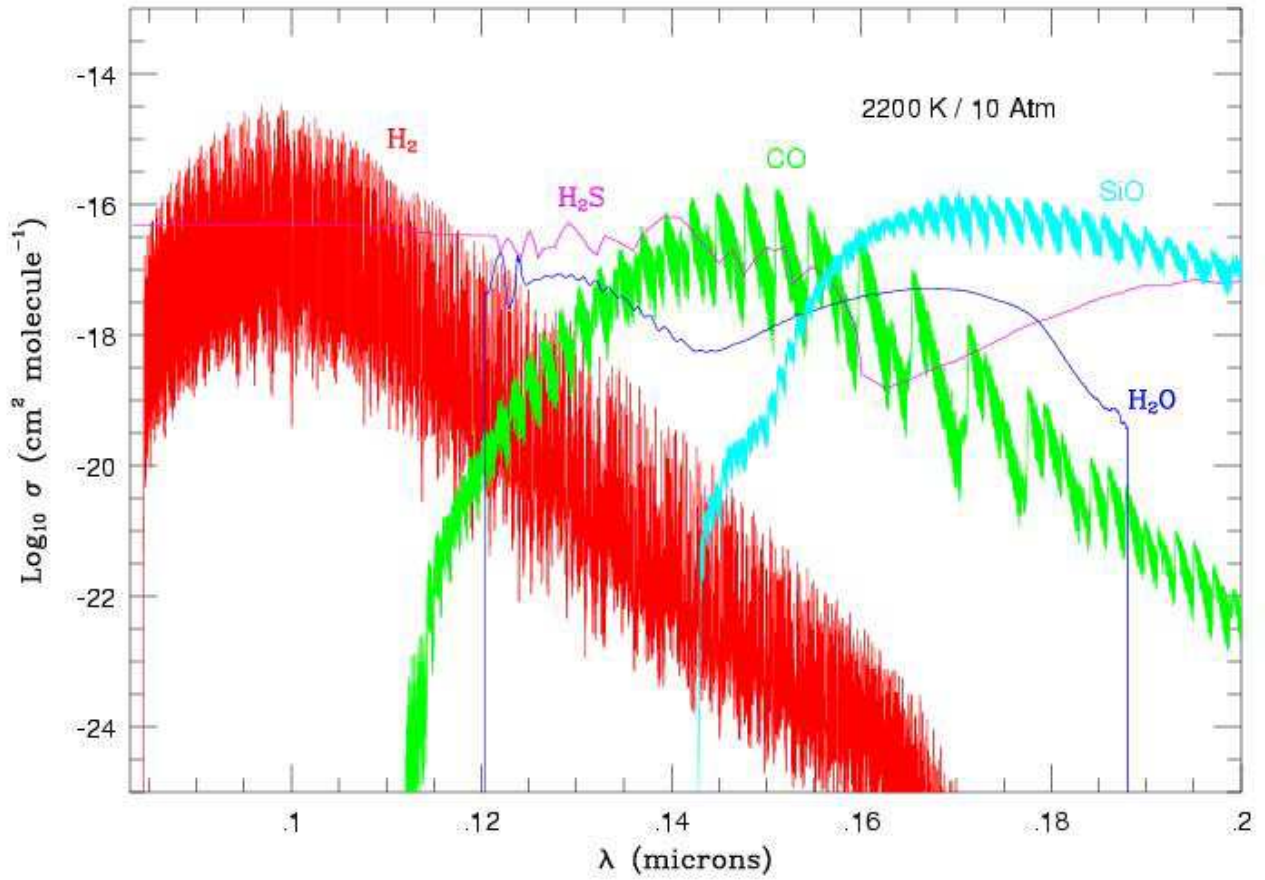


FIG. 11.— The log (base 10) of the monochromatic absorption  $\sigma$  in  $\text{cm}^2\text{molecule}^{-1}$  as a function wavelength  $\lambda$  in  $\mu\text{m}$  at a temperature of 2200 K and a pressure of 10 atmospheres in the ultraviolet for  $H_2$  (red),  $CO$  (green),  $H_2O$  (blue),  $H_2S$  (magenta), and  $SiO$  (cyan). All the transitions are electronic, and in particular the absorption for  $H_2$  is calculated from the  $B-X$  and  $C-X$  (respectively, the Lyman and Werner) systems, and for  $CO$  from the  $A-X$  system, as well as for  $SiO$ . Since we have no individual line data for  $H_2O$  and  $H_2S$ , the temperature and pressure dependences are not calculated, and only smoothed plots can be made. As with the previous figure, a high pressure is chosen to smooth out for graphical representation several of the absorptions.

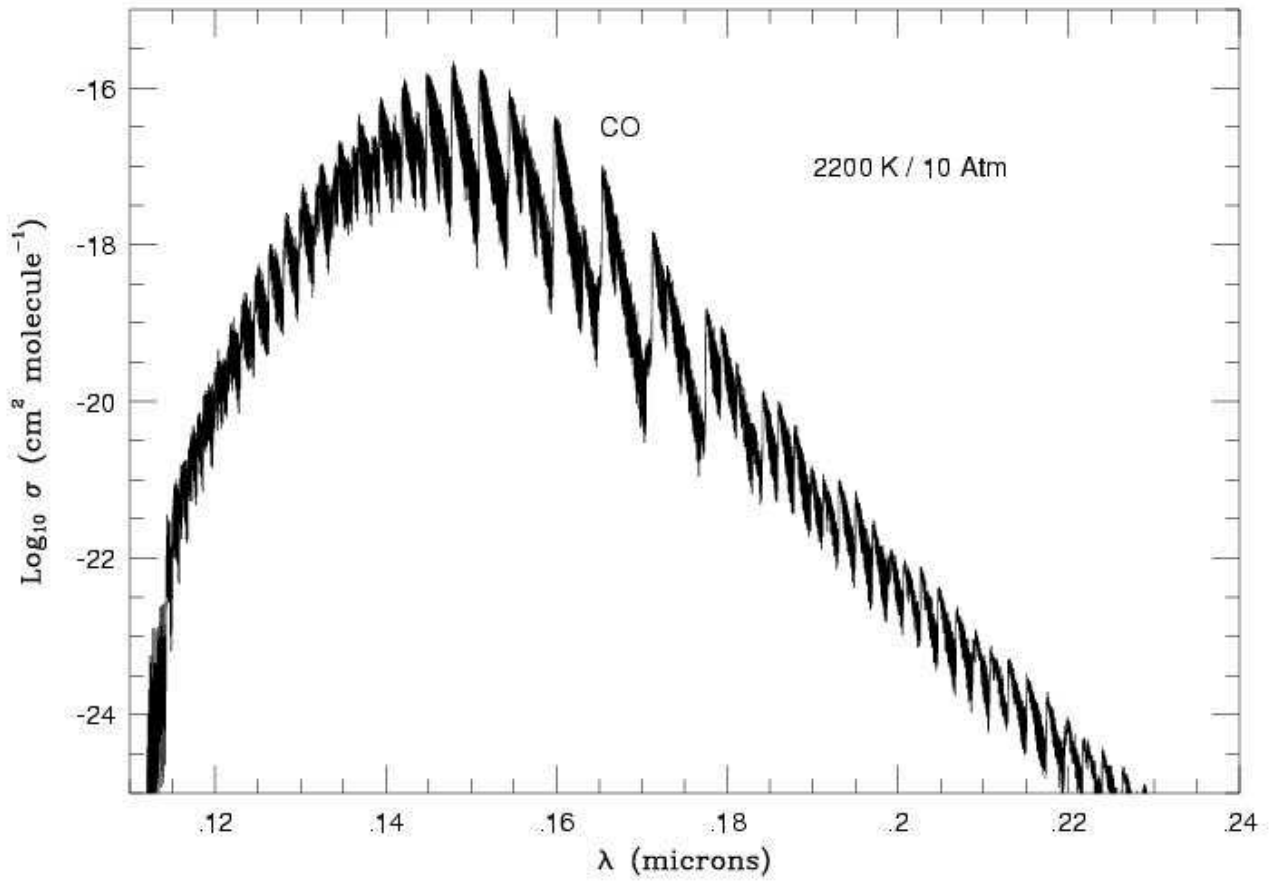


FIG. 12.— The absorption of *CO* as given in the previous figure for the same temperature and pressure, but extended to longer wavelengths to give more complete coverage.



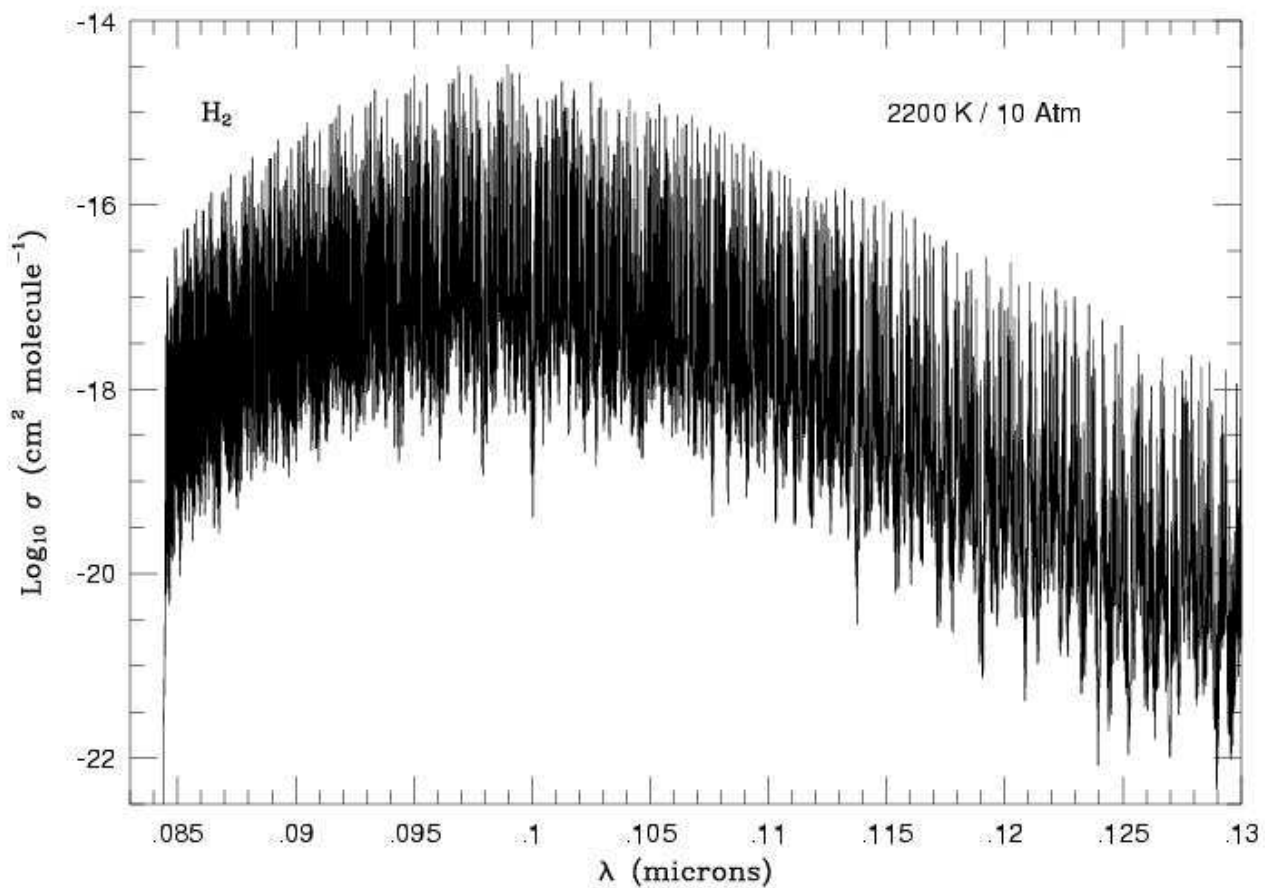


FIG. 13.— The short-wavelength absorption of  $H_2$  as given in Fig. 11 for the same temperature and pressure, but on a larger wavelength scale to show more detail.  $H_2$  is by far the most abundant species, absorbs strongly in the ultraviolet, and so completely dominates that part of the spectrum.

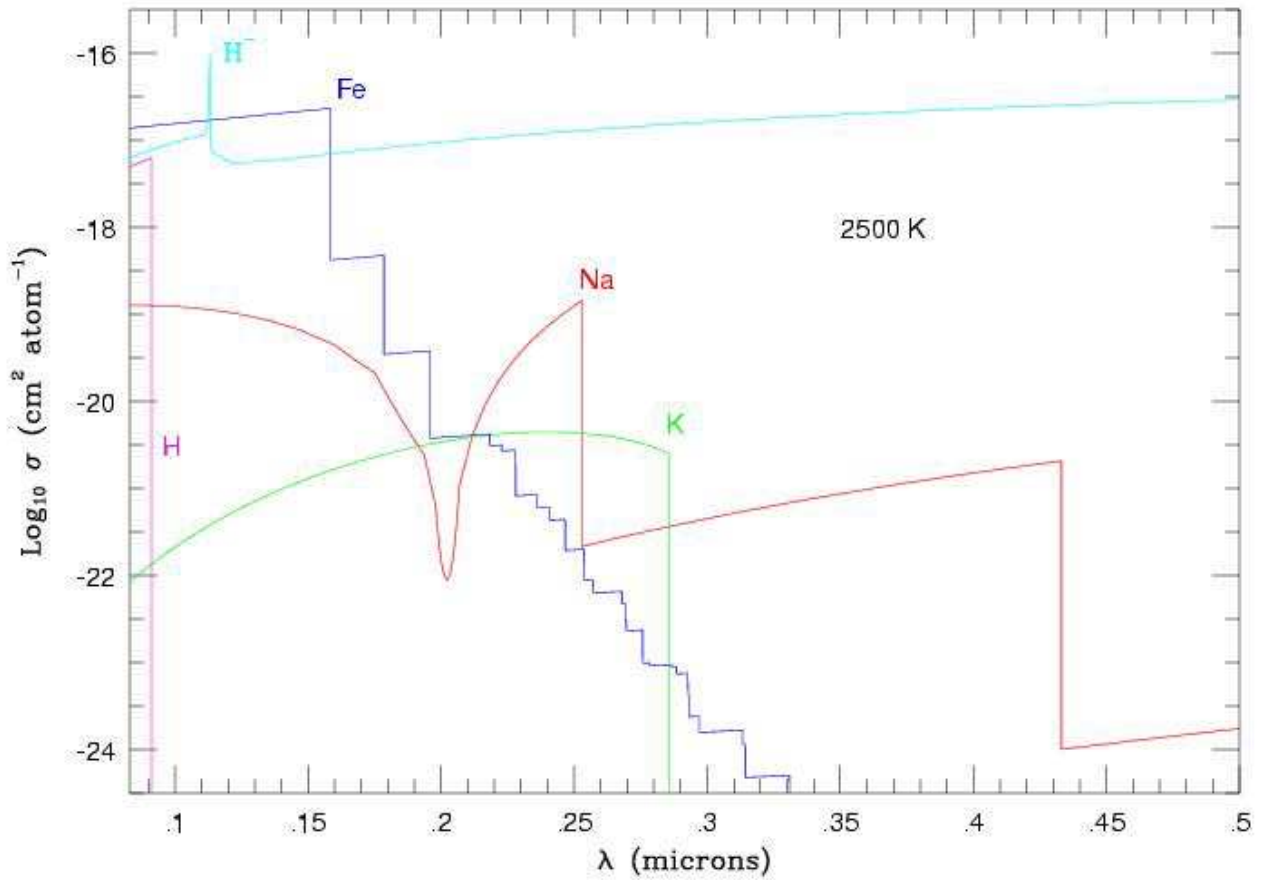


FIG. 14.— The log (base 10) of the monochromatic absorption  $\sigma$  in  $\text{cm}^2\text{atom}^{-1}$  as a function wavelength  $\lambda$  in  $\mu\text{m}$  at a temperature of 2500 K due to bound-free transitions for the atomic species  $\text{Na}$  (red),  $\text{K}$  (green),  $\text{Fe}$  (blue), and  $\text{H}$  (magenta). In addition the negative hydrogen ion  $\text{H}^-$  (cyan) is also plotted. The effects of pressure have been neglected. In the case of  $\text{Fe}$ , this is plotted with the atomic lines in Fig. 9. The absorption shown here due to  $\text{H}$  is caused by the Lyman continuum, and the absorption due to  $\text{H}^-$  is a smooth continuum covering the whole ultraviolet and visible spectrum, as well as the near infrared above the absorption threshold. However, note the spike just shortward of  $0.11 \mu\text{m}$ .

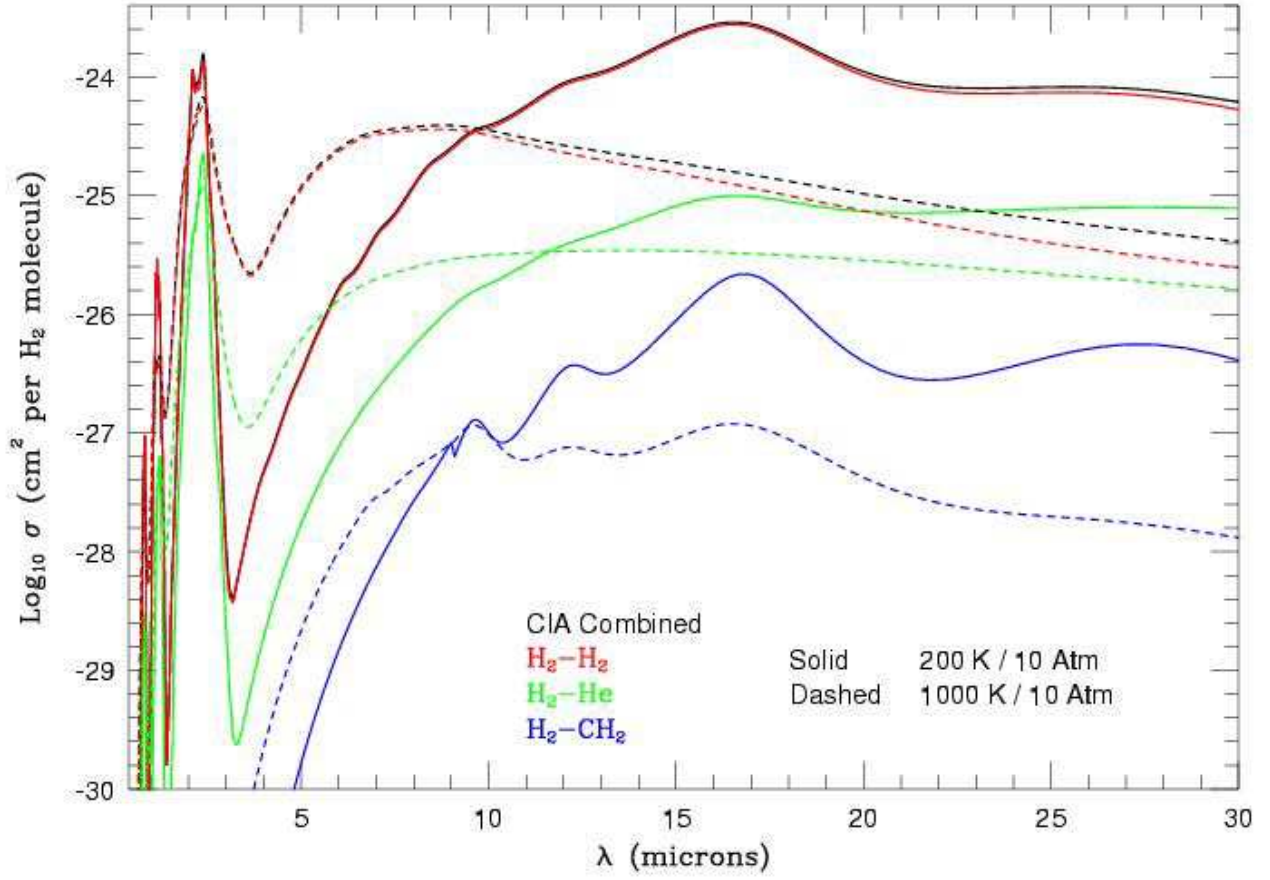


FIG. 15.— The log (base 10) of the monochromatic collision induced absorption  $\sigma$  in  $\text{cm}^2$  per  $H_2$  molecule as a function wavelength  $\lambda$  in  $\mu\text{m}$  at 200 K and 10 atmospheres, shown by solid curves, and 1000 K and 10 atmospheres show by dashed curves. The red curves are due to  $H_2 - H_2$  CIA expressed as the absorption per  $H_2$  molecule in the gas, regardless of whether any particular  $H_2$  molecule is undergoing a collision; the green curves are due to  $H_2 - He$  CIA, but weighted by the abundance of helium, and likewise the blue curves are due to  $H_2 - CH_4$  CIA, weighted by the abundance of methane. The black curves are the combinations of these contributions at the two temperatures, i.e. the CIA due to  $H_2$  colliding with any of  $H_2$ ,  $He$ , and  $CH_4$ . Note that the CIA scales as the square of the pressure.

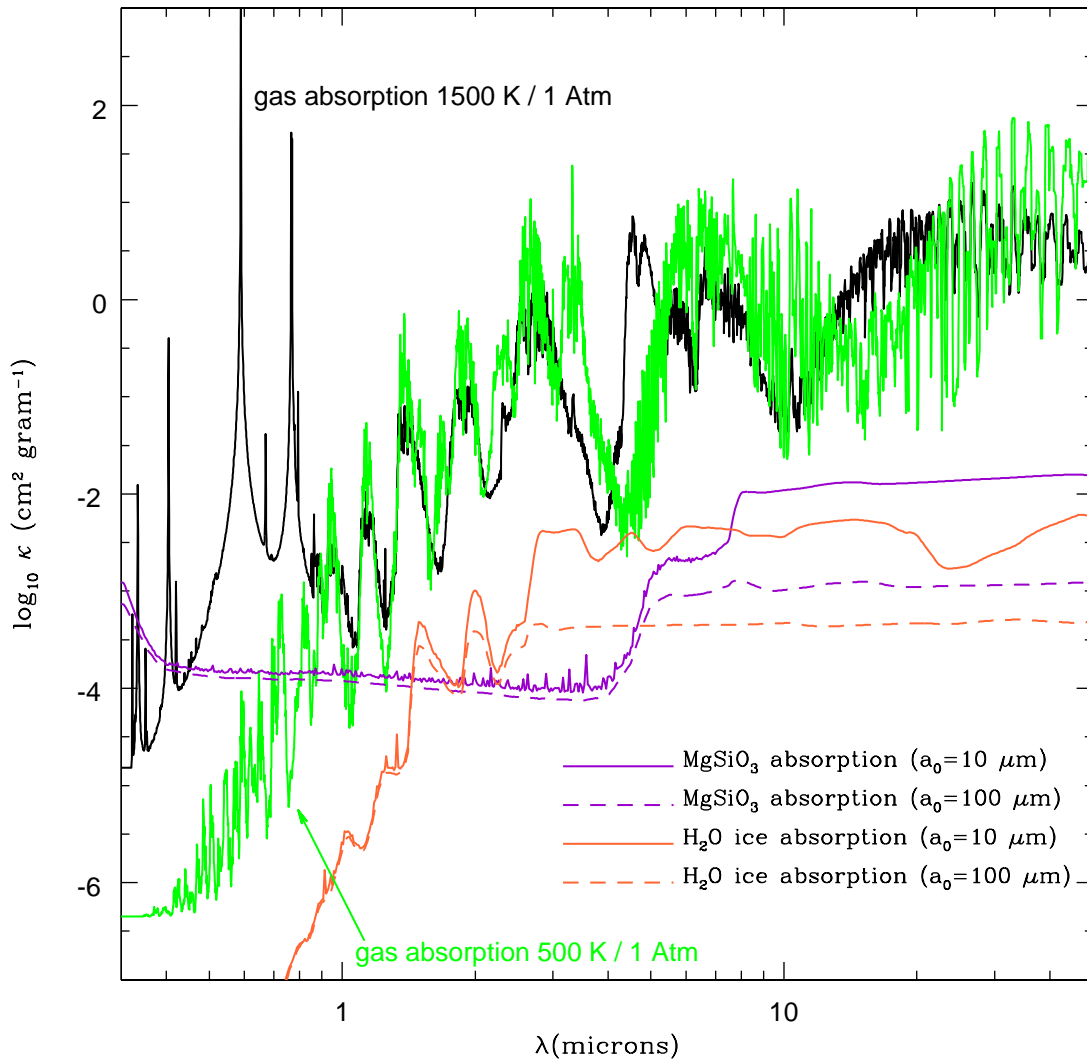


FIG. 16.— The log (base 10) of the monochromatic opacity  $\kappa$  in  $\text{cm}^2\text{g}^{-1}$  as a function of wavelength  $\lambda$  in  $\mu\text{m}$  for separate gas and grain absorption. The green and black curves represent at a pressure of 1 atmosphere the monochromatic gas opacity at temperatures of 500 K and 1500 K, respectively, with the contributions of the individual species weighted by their abundances. The magenta and orange curves represent the absorption due to grains of  $\text{MgSiO}_3$  and  $\text{H}_2\text{O}$  ice, respectively, with the solid and dashed curves showing the absorption due grains or ice particles with radii of  $10 \mu\text{m}$  and  $100 \mu\text{m}$ , respectively. The opacity is weighted by the abundances; in the case of  $\text{MgSiO}_3$  it is given by the least abundant element, which is  $\text{Si}$ , and in the case of ice the abundance is based on the equilibrium with  $\text{H}_2\text{O}$  in the vapor phase. In both cases, the slight effects of temperature and pressure are neglected, except that the temperature has to be low enough for the phase to be stable, which in the case of  $\text{H}_2\text{O}$  ice is at or below 273 K.

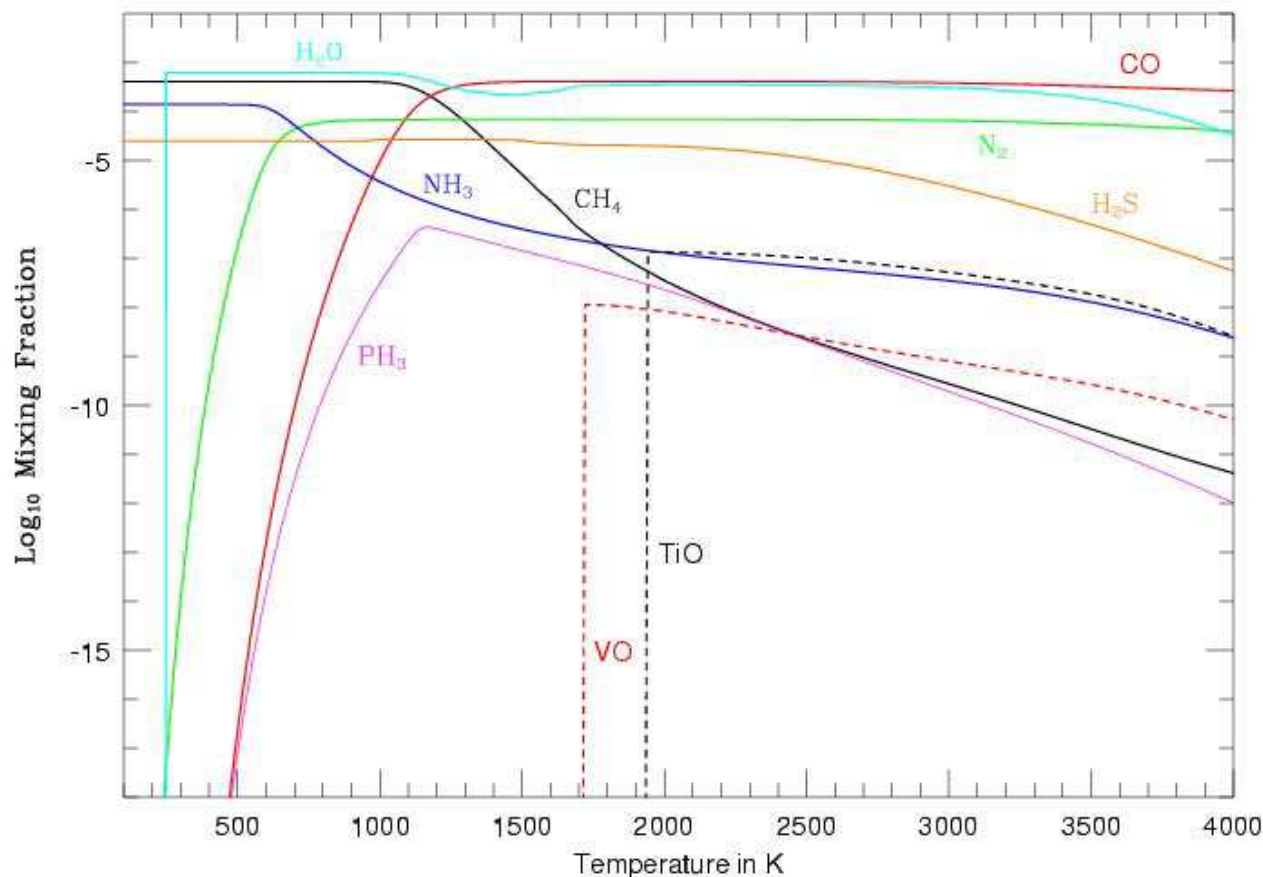


FIG. 17.— The log (base 10) of the mixing fraction as a function of temperature at a total gas pressure of 1 atmosphere for the seven molecules shown with solid curves  $CH_4$  (black),  $CO$  (red),  $N_2$  (green),  $NH_3$  (blue),  $H_2O$  (cyan),  $H_2S$  (orange), and  $PH_3$  (magenta), and the two molecules shown with dashed curves  $TiO$  (black) and  $VO$  (red). At 4000 K,  $CO$  and  $N_2$  are the most stable species, containing nearly all the carbon and nitrogen, respectively. With decreasing temperature,  $CO$  reacts with  $H_2$ , forming  $CH_4$ , which becomes the dominant carbon-bearing species at low temperatures, and  $N_2$  reacts with  $H_2$ , forming  $NH_3$ , which likewise becomes the dominant nitrogen-bearing species at low temperatures. Except above about 3000 K,  $H_2O$  is fully associated containing nearly all the available oxygen that is not bound in  $CO$ . Below about 1600 K, its abundance temporarily falls slightly due to the condensation of silicates which reduce the available oxygen; however, the mixing fraction of  $H_2O$  then rises again when  $CO$  is converted to  $CH_4$ , which releases the oxygen tied up in  $CO$ . Finally, at 273 K  $H_2O$  drops effectively to zero due to the condensation of ice. With decreasing temperature, both  $TiO$  and  $VO$  rise as they associate, then sharply drop to effectively zero when condensates involving  $Ti$  and  $V$  form.

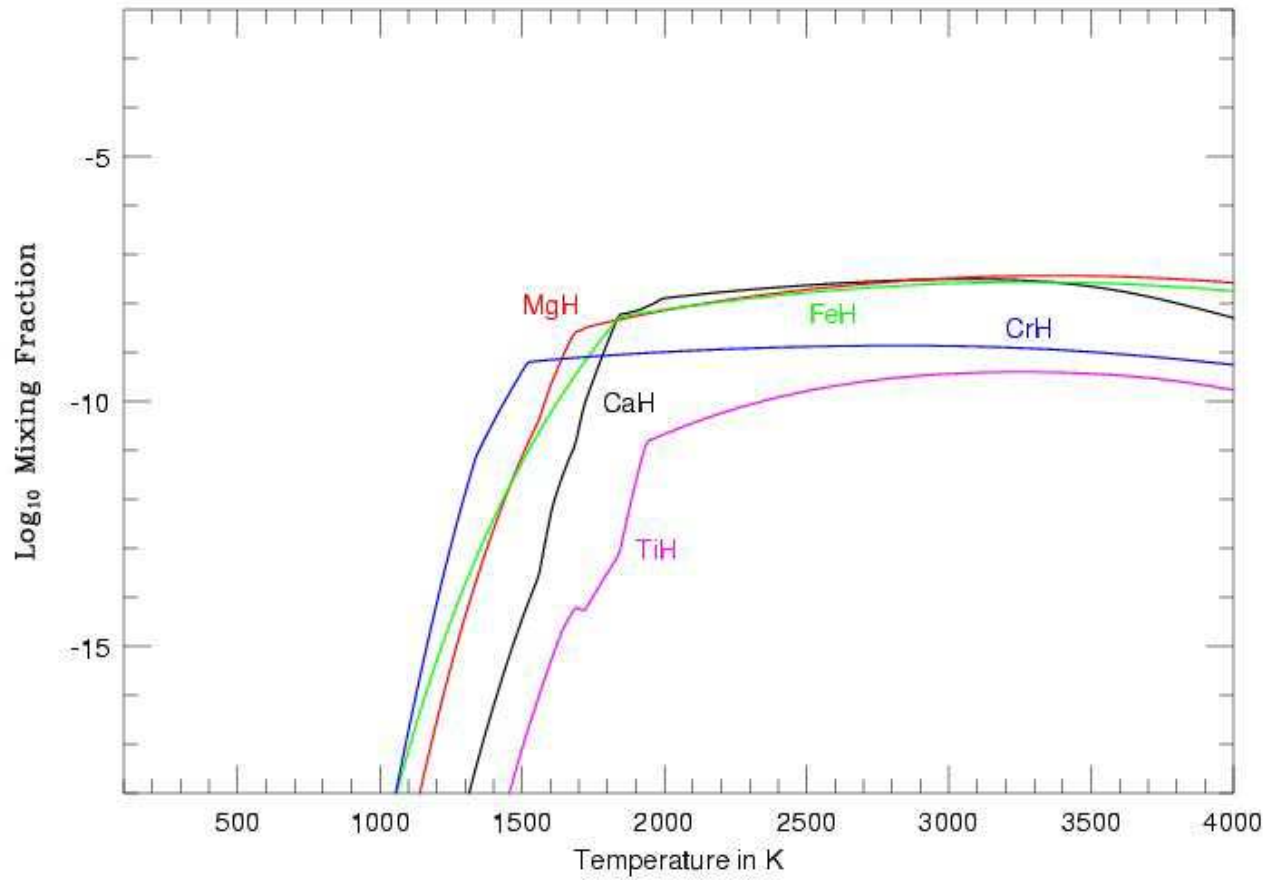


FIG. 18.— The log (base 10) of the mixing fraction as a function of temperature at a total gas pressure of 1 atmosphere for the metal hydrides *CaH* (black), *MgH* (red), *FeH* (green), *CrH* (blue), and *TiH* (magenta), shown with the same scale as the previous figure. The drop in abundance with decreasing temperature for all these molecules below about 2000 K, is due to the formation of condensates involving the corresponding metal. The kinks in the curves, particularly for *TiH*, are due to the replacement of one dominant condensed phase involving that element by another.

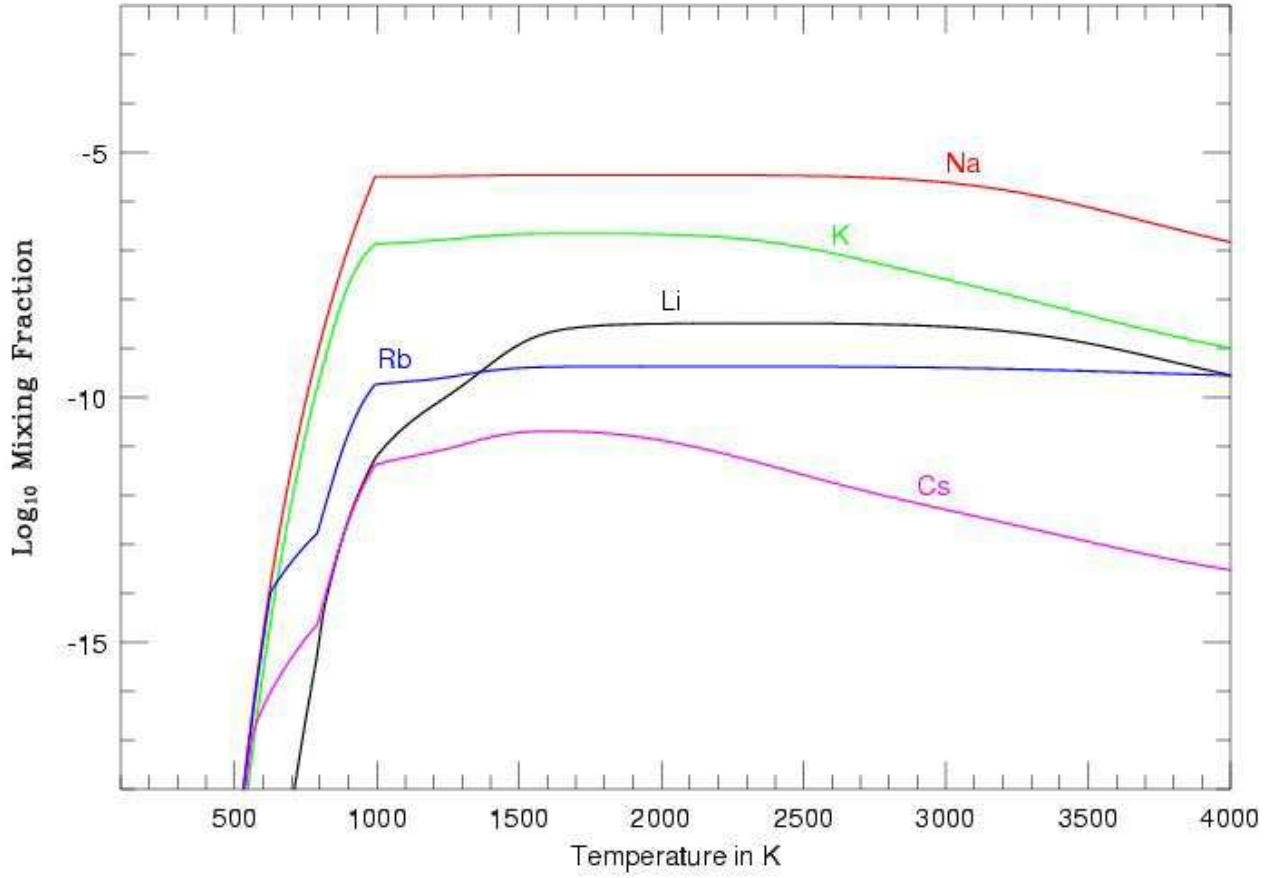


FIG. 19.— The log (base 10) of the mixing fraction as a function of temperature at a total gas pressure of 1 atmosphere for the alkali elements in their monatomic form: *Li* (black), *Na* (red), *K* (green), *Rb* (blue), and *Cs* (magenta), shown on the same scale as previously. In all cases, they start decreasing in abundance with decreasing temperature at about 1000 K, due to the formation of condensates, and in the case of *Rb* and *Cs*, kinks at lower temperatures are due to the most abundant condensed species being replaced by another one. Unlike the other elements, *Rb* has a constant abundance above about 2000 K, but this is an artifact of thermodynamic data missing for some species of *Rb*.

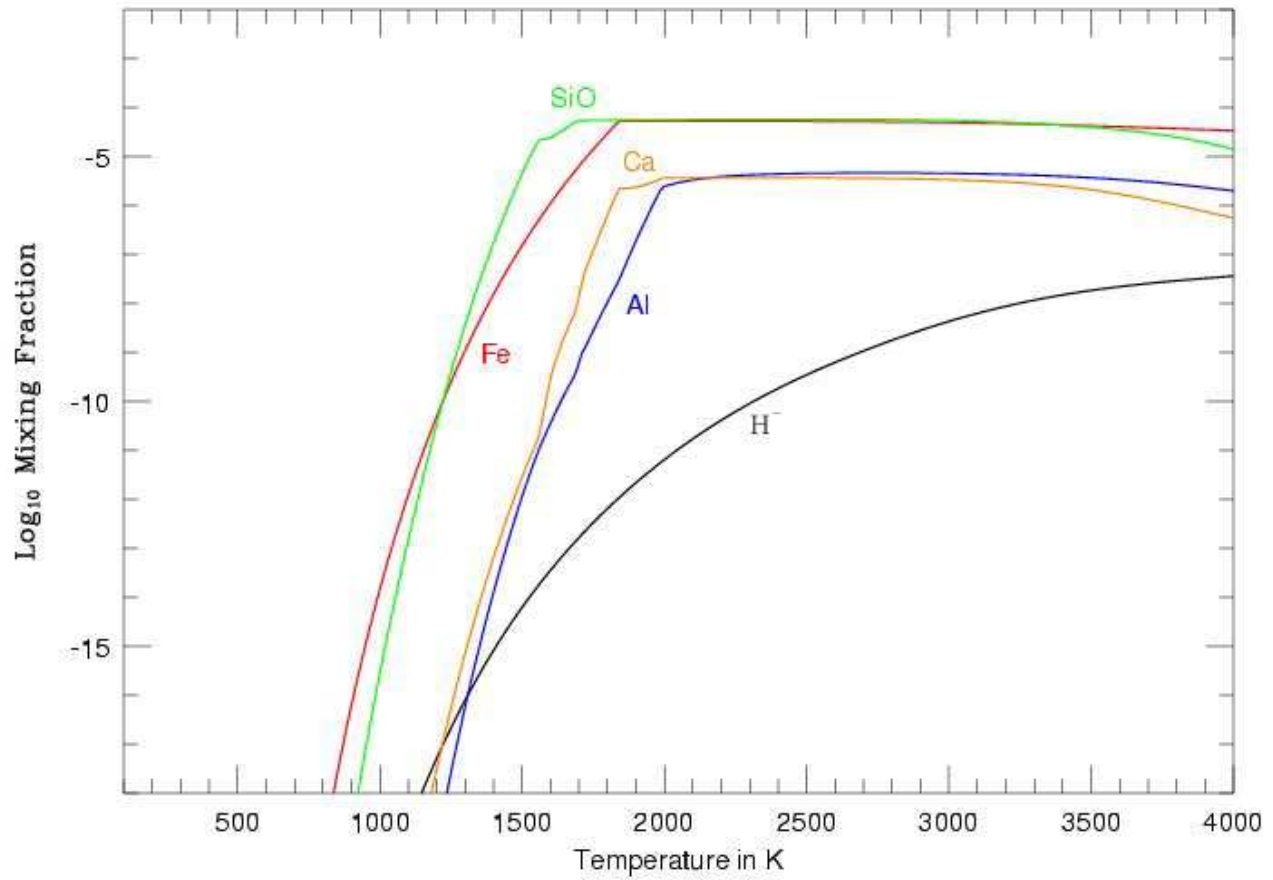


FIG. 20.— The log (base 10) of the mixing fraction as a function of temperature at a total gas pressure of 1 atmosphere for the negative hydrogen ion (black), *Fe* (red), *SiO* (green), *Al* (blue), and *Ca* (orange), plotted on the same scales as before. These are some of the atomic species together with *SiO* which are important opacity sources in the visible and ultraviolet, in addition to the other species plotted. With the exception of  $H^-$ , they all start decreasing with decreasing temperature between 2000 and 1500 K, due to the formation of condensates.



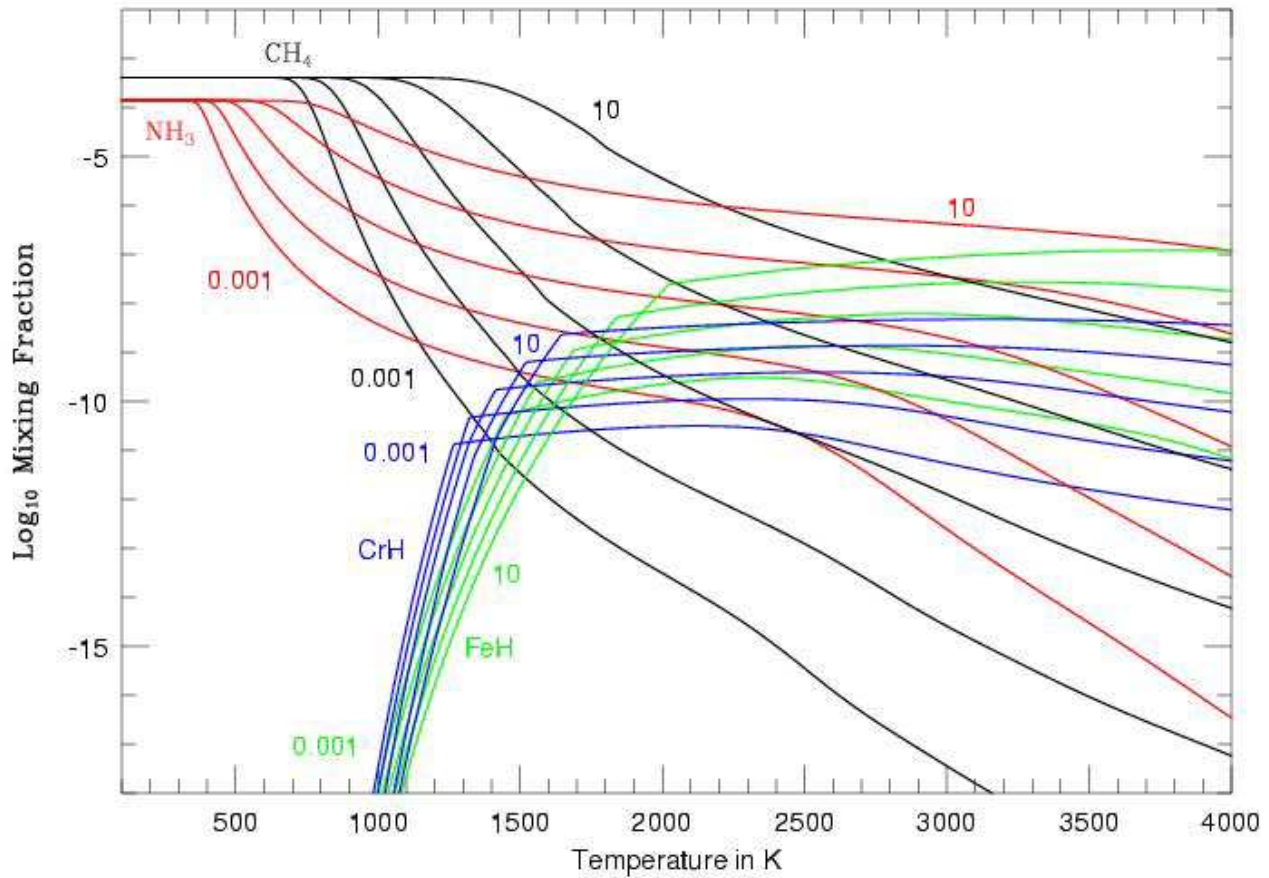


FIG. 21.— The log (base 10) of the mixing fraction as a function of temperature for pressures of 0.001, 0.01, 0.1, 1, and 10 atmospheres for  $CH_4$  (black curves),  $NH_3$  (red curves),  $FeH$  (green curves), and  $CrH$  (blue curves), with the same scales as before. For each species, only the curves for 0.001 and 10 atmospheres are labeled (to avoid clutter), with the curves for the three intermediate pressures lying between them. In the cases of  $CH_4$  and  $NH_3$ , the temperatures at which these molecules are fully associated increase with increasing pressure, and above these temperatures when these molecules are less abundant the abundances increase with pressure, which is in full accord with the principle of mass action. Both  $FeH$  and  $CrH$  are influenced by the formation of condensates between about 1000 and 2000 K, such that with increasing pressure the temperature at which condensation takes place and reduces the abundance in the gas phase increases. Moreover, when no condensation is present, the abundance increases with increasing pressure, such that with decreasing temperature, the curve for a given pressure crosses over those due to higher pressures that are rapidly falling at a higher temperature when condensation takes place.

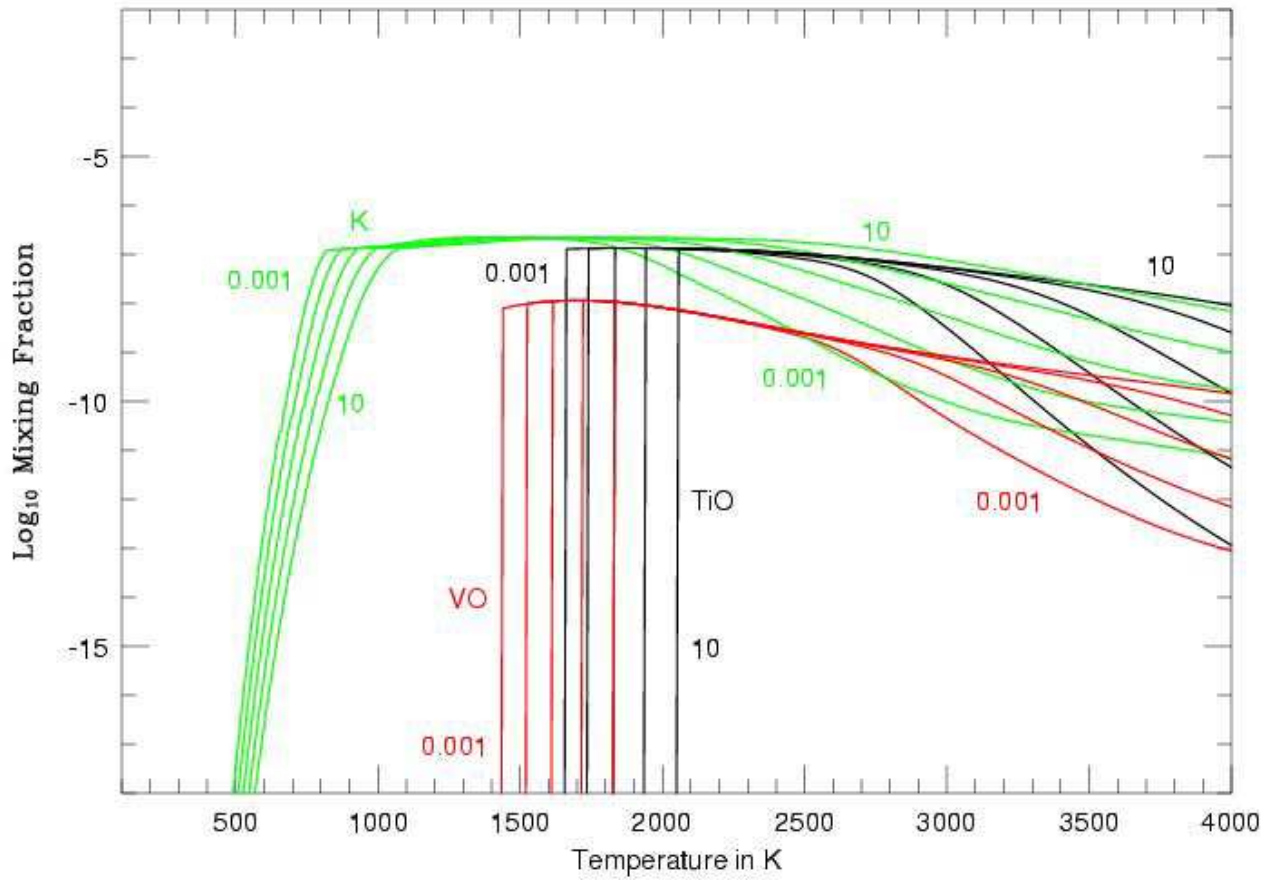


FIG. 22.— The log (base 10) of the mixing fraction as a function of temperature for pressures of 0.001, 0.01, 0.1, 1, and 10 atmospheres for  $TiO$  (black curves),  $VO$  (red curves), and  $K$  (green curves), with the same scales as the other abundance plots. As before, only the curves corresponding to 0.001 and 10 atmospheres are labeled, but in the case of  $VO$ , due to overlap with curves for  $K$  and  $TiO$ , the label for the curve corresponding to 10 atmospheres is omitted. As with  $FeH$  and  $CrH$  in the previous figure, the condensation temperatures at which these species are removed from the gas phase increases with pressure, but when these species are well above the condensation temperatures, the abundances increase with pressure.